Diagnosing the Prominence-Cavity Connection in the Solar Corona

by

D. J. Schmit

B.A., Boston University, 2007

M.S., University of Colorado,2010

A thesis submitted to the

Faculty of the Graduate School of the

University of Colorado in partial fulfillment

of the requirements for the degree of

Doctor of Philosophy

Department of Astrophysics and Planetary Science

2012

This thesis entitled:
Diagnosing the Prominence-Cavity Connection in the Solar Corona
written by D. J. Schmit
has been approved for the Department of Astrophysics and Planetary Science

Dr. S. Gibson

Dr. M. Rast

Date

The final copy of this thesis has been examined by the signatories, and we find that both the content and the form meet acceptable presentation standards of scholarly work in the above mentioned discipline.

Schmit, D. J. (Ph.D., Astrophysics)

Diagnosing the Prominence-Cavity Connection in the Solar Corona

Thesis directed by Dr. S. Gibson

The corona is a unique layer in the solar atmosphere where the temperature rapidly increases as a function of radial height. While a majority of the corona exists at temperatures above one million degrees Kelvin, there are embedded regions of much cooler and denser plasma known as prominences. The formation mechanism and force balance of prominences are open questions in solar physics.

The energetic equilibrium of the corona is described by a balance of heating, thermal conduction, and radiative cooling. Prominences can be described by the thermal instability of coronal energy balance which leads to the formation of cool condensations. For condensations to exist in force equilibrium in the corona, they must be supported against gravity by the magnetic field. Condensations will fall into the gravitational well provided on dipped magnetic field lines, but these field lines will also contain coronal plasma which surrounds the condensation. These formation and stability considerations require a hydrodynamic energetic connection and a magnetostatic structural connection between the prominence and the surrounding corona.

Observationally, the prominence is surrounded by a density depleted elliptical structure known as a cavity. In this dissertation, we use extreme ultraviolet remote sensing observations of the prominence-cavity system to diagnose the static and dynamic properties of these structures. The observations are compared with numerical models for the time-dependent coronal condensation process and the time-independent corona-prominence magnetic field.

To diagnose the density of the cavity, we construct a three-dimensional structural model of the corona. This structural model allows us to synthesize extreme ultraviolet emission in the corona in a way that incorporates the projection effects which arise from the optically thin plasma. This forward model technique is used to constrain a radial density profile simultaneously in the

cavity and the streamer. We use a χ^2 minimization to find the density model which best matches a density sensitive line ratio (observed with Hinode/Extreme ultraviolet Imaging Spectrometer) and the white light scattered intensity (observed with Mauna Loa Solar Observatory MK4 coronagraph). This diagnostic finds that the observed cavity has a density depletion of 30% relative to the streamer.

The diagnosis of thermodynamic properties of the static cavity provides a measurement of the time-averaged equilibrium condition of the plasma. However, the coronal cooling model of prominence formation requires that there will be a time-dependent change in the coronal region which supplies mass to the prominence. We use extreme ultraviolet spectra and spectral images to diagnose the dynamics of the prominence and the surrounding corona. Based on the doppler shift of extreme ultraviolet coronal emission lines, we find that there are large regions of flowing plasma which appear to occur within cavities. These line of sight flows have speeds of 10 km s^{-1} and projected spatial scales of 100 Mm. Using the Solar Dynamics Observatory Atmospheric Imaging Assembly (SDO/AIA) dataset, we observe dynamic emission from the prominence-cavity system. The SDO/AIA dataset observes multiple spectral bandpasses with different temperature sensitivities. Time-dependent changes in the observed emission in these bandpass images represent changes in the thermodynamic properties of the emitting plasma. We find that the coronal region surrounding the prominence exhibits larger intensity variations (over tens of hours of observations) as compared to the streamer region. This variability is particularly strong in the cool coronal emission of the 171Å bandpass. We identify the source of this variability as strong brightening events that resemble concave-up loop segments and extend from the cool prominence plasma. These features, referred to as prominence horns, are observed in multiple SDO/AIA bandpasses which allows us to determine how the characteristics of horns vary as a function of temperature. The most intriguing aspect of horn emission is the strong correlation between cool coronal emission and prominence emission and the weak correlation between hot coronal emission and cool coronal emission. Based on the dynamic observations, we suggest that horns are likely the signature thermal changes along magnetic field lines.

Magnetic field lines are the basic structural building block of the corona. Energy and pressure balance in the corona occur along magnetic field lines. The large-scale extreme ultraviolet emission we observe in the corona is a conglomerate of many coronal loops projected along a line of sight. In order to calculate the plasma properties at a particular point in the corona, we use one-dimensional models for energy and pressure balance along field lines. In order to predict the extreme ultraviolet emission along a particular line of sight, we project these one-dimensional models onto the three-dimensional magnetic configuration provided by a MHD model for the coronal magnetic field.

The thermal non-equilibrium model describes a method for inducing catastrophic cooling in a coronal loop by distributing chromospheric mass throughout the coronal region of the loop. This model results in the formation of a prominence along dipped magnetic loops. We find that the thermal non-equilibrium model matches our dynamic constraints of prominence horns. Loops undergoing cooling will brighten in the 171Å bandpass in SDO/AIA and this coronal emission will be correlated with dynamic emission from prominence plasma. While prominence horns and prominence formation appear compatible based on the one-dimensional modeling, there is a discrepancy when we consider the projected spatial structure of horns. Horns project inside the density-depleted cavity, while the mechanism driving prominence formation requires density-enhancements.

The three dimensional corona is composed of the projection of many distinct coronal loops. To diagnose the projection effects of prominence horns, we combine the one-dimensional hydrodynamic model with the three-dimensional flux rope model of the prominence-corona magnetic field. The flux rope model uses dipped and twisted magnetic field lines to support a prominence. The distribution of dipped field lines in the flux rope is not uniform. The segments of dipped field lines which would emit in the coronal bandpasses of SDO/AIA are volumetrically isolated along the topological surface which forms the boundary between the twisted flux rope and the near-potential arcade. The projected emission from these field lines would occur throughout the entirety of the flux rope cross section even though the field lines do not extend throughout most of the flux rope volume. Based on the flux rope model, prominence horns are an indication of prominence formation, but they do not occur within the cavity and they are not responsible for the density depletion

in that structure.

While the dipped field lines in the flux rope model can be linked to the prominence, they are not linked to the cavity. We use a one-dimensional hydrostatic model for coronal energy balance to solve for the plasma parameters throughout the volume of the flux rope model. Variations of plasma parameters between magnetic field lines occur due to geometric considerations for energy loss and column mass. Using this hydrostatic model, we find that the flux rope interior is density depleted relative to the surrounding arcade. Structurally, we find that the short field lines which dominate the flux rope volume can explain the density depletion of the cavity. By combining the hydrostatic and hydrodynamic results, we find that the flux rope model can describe the connection between prominence horns and the cavity. The cavity is formed by axial field lines which are circumscribed by high-density dipped field lines. The cavity is not directly connected to the prominence and does not supply mass to it.

These results have allowed us to the establish the first comprehensive picture on the magnetic and energetic interaction of the prominence and the cavity. While the originally hypothesis that the cavity supplies mass to the prominence proved inaccurate, we cannot simply say that these structures are not related. Rather our findings suggest that the prominence and the cavity are distinct magnetic substructures that are complementary regions of a larger whole, specifically a magnetic flux rope.

Contents

Chapter

Tables

Table

Figures

Figure

Chapter 1

The Prominence-Cavity System

1.1 Introduction

The outer solar atmosphere can be separated into three specific layers: photosphere, chromosphere, and corona. The energy generated in the solar core is radiated from the photosphere, which has a temperature of 5600 K (kelvin). The photosphere is where we observe sunspots, which are the tell-tale signs of the Sun's magnetic field. Above the photosphere, a peculiar transition occurs. The temperature rapidly rises as we move radially outward into the chromosphere. The chromosphere exists as a thin and highly dynamic transition to the corona. In 1000 kilometers, the 5600 K photosphere transitions to the 1,000,000 K (and hotter) corona. This drastic change in temperature is associated with a change in physics. Whereas the photosphere is controlled by the physics that describe the motions of a fluid, the corona is controlled by the physics that describe electricity and magnetism. It is this transition between these disparate physical regimes which gives rises to the beautiful complexity of the solar corona.

This thesis focuses on diagnosing one of the complex magnetic structures that develop in the corona due to the turbulent motions of lower solar atmosphere. Prominences are regions of cool, dense plasma in the corona. Figure 1.1a shows two prominences as they are viewed by an orbiting telescope (Solar Dynamics Observatory/Atmospheric Imaging Assembly). Prominences have a temperature around 20,000 K but are surrounded by the 1,000,000 K corona. Why are prominences cooler than the corona? What makes that region of the solar atmosphere form a prominence? These are the two primary questions in prominence physics.

In this thesis, we address these questions using the clues that we are given from another structure: cavities. Cavities are dim elliptical regions which surround prominences. Figure 1.1b shows two cavities which surround two prominences. The prominences and the cavities are not displayed in the same image because they emit light at different wavelengths due to their different temperatures. The properties of cavities provide us insight into how prominences form.

We use observational data and theoretical models to address what the magnetic connection is between the prominence and the cavity.We assess whether the prominence is connected to the cavity through a dynamic process where mass drains out of the cavity into the prominence. This theoretical model explains the two most fundamental aspects of the prominence-cavity: why the cavity is density-depleted and why the prominence is density-enhanced. However, only using a numerical model which takes into account the physical evolution of prominence plasma can we accurately validate this theory.

The primary difficulty in this question stems from the fact that we do not have magnetic field measurements from the prominence and the cavity. Instead, we use observational diagnostics to probe the physical quantities which are derivable: density and dynamics specifically. We then take a forward approach, and use magnetic and energetic models for prominences to compare how the measurements are related to theoretical predictions.

1.1.1 Summary of Results

Our research has focussed on diagnosing the prominence-cavity system through a combination of observational diagnostics and the comparison of observational measurements and model predictions. We use a structural forward model to derive a radial density profile for the cavity and streamer. We find the cavity is density-depleted relative to the streamer by 30%. We use EUV emission to trace thermodynamic changes in the prominence-cavity system. This technique reveals that there is an interaction between prominence plasma and coronal plasma which projects as inside the cavity. The dynamic structure is referred to as prominence horns. The spatial, temporal, and spectral characteristics of prominence horns are analyzed to provide constraints on the energetic

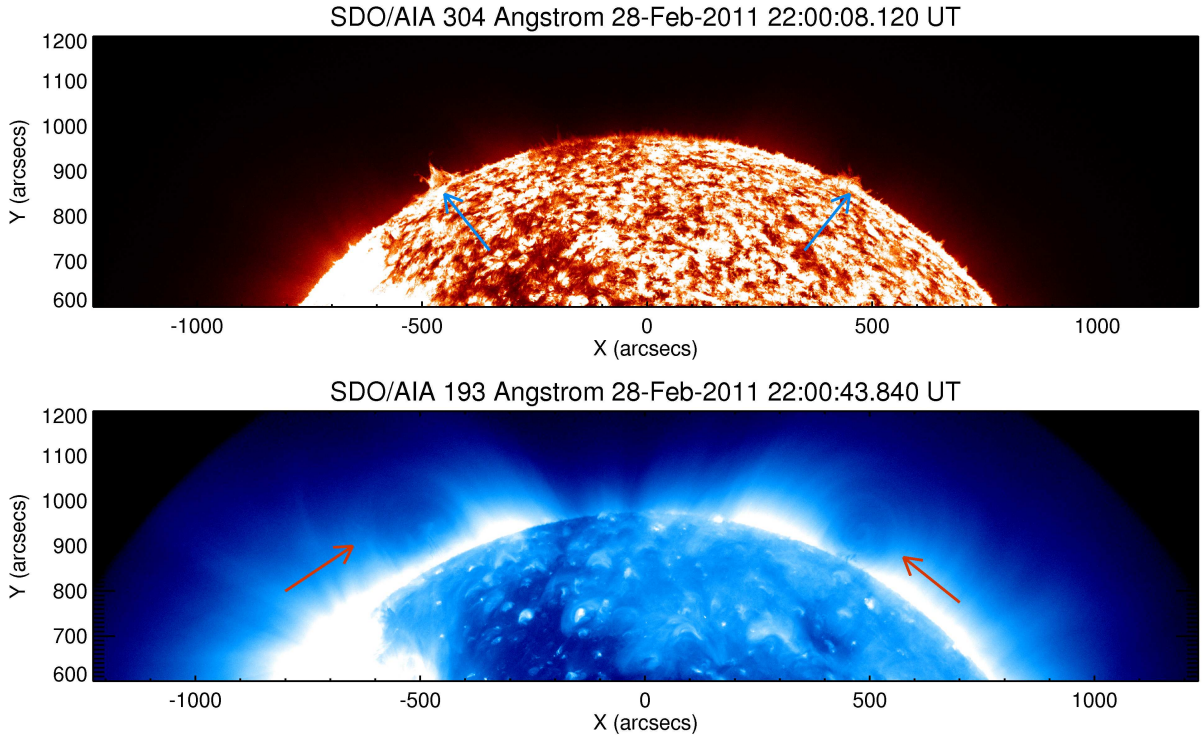

Figure 1.1 Extreme ultraviolet spectral images of a prominence and a prominence cavity. Top: the emission from singly-ionized helium at 304Å shows the extension of cool prominence material (blue arrows) off of the solar limb. Bottom: emission from the highly ionized corona (Fe XII 193Å) shows that dim, elliptical regions known a cavities surround prominences (red arrows).

process which produces them. We use a combination of one-dimensional energetic models and a three-dimensional magnetic model to compare the theory of thermal non-equilibrium prominence formation to prominence horns. The dynamic properties of prominence horns are compatible with thermal non-equilibrium, but the static properties of the cavity are not as the cooling process requires high densities. We use the flux rope model for the prominence magnetic field to show that topologically distinct magnetic regions within the flux rope may explain both the static and dynamic cavity observations. A catastrophic cooling process active on dipped field lines would be isolated to the boundary between the flux rope axis and the arcade field. The undipped, weakly twisted field near the flux rope axis would account for the density-depleted cavity structure.

1.1.2 Outline of Dissertation

Chapter 1 goes on to introduce the physics of the magnetic and energetic prominence-cavity system as well as the observational methods we use to diagnose this structure. Chapter 2 discusses a density diagnostic of the cavity. This chapter describes a forward model which allows us to disambiguate the cavity from line-of-sight projection effects. Chapter 3 discusses observations of the dynamics in the prominence-cavity system. This work measure flows and variability in extreme-ultraviolet emission. A detailed analysis of these dynamics provides constraints on the energetic models of prominence formation. Chapter 4 discusses the thermal non-equilibrium model for prominence formation and the flux rope model for prominence support. We assess whether the dynamics observations are compatible with prominence formation, and how the observational structure relates to magnetic structure of a flux rope. Chapter 5 discusses the conclusions of these chapters as a whole.

1.2 Physics of the Prominence-Cavity System

The focus of this thesis is on diagnosing the energetic and magnetic state of prominence cavities. Cavities are the primary focus, but throughout this thesis I will repeatedly delve into the details of prominence physics. The reason for this is related to the nature of the connection between

these structures. Cavities, in many ways, are comparable to their coronal surroundings. They are found to be at approximately coronal temperatures [Kucera et al., 2012], and the measured density depletion relative to streamers is less than 50% [Fuller and Gibson, 2009]. Prominences, however, are a very distinct structure. They are two orders of magnitude denser than the corona, as well as two orders cooler. The emission corona is defined by magnetic loop structures, whereas prominences appears amorphous (see Figure 1.1). Despite these wholesale differences, prominences are an incredibly pervasive phenomena on the Sun, and there is observational evidence that they occur on other stars [Donati and Collier Cameron, 1997].

Because of their very distinct nature, we have detailed theories on the formation and stabilization of prominences. The goal of this thesis to extend these models to the cavity, and address what implications the prominence system has on the surrounding coronal environment. This approach will be used to address the question:*are the prominence and the cavity magnetically linked?*

Prominence physics is divided into two distinct subfields: magnetic structure and thermodynamic stability. We will now proceed to discuss these two fields, how they connect, and what we can learn from each.

1.2.1 Magnetic Structure of Prominences

One of the most basic but perplexing observations of prominences is that they are suspended against gravity. Prominences have measured densities from $10^{10} - 10^{13}$ cm^{-3} while coronal densities are in the range of $10^{7} - 10^{9}$ cm^{-3}. Figure 1.2 shows a prominence simultaneously from two different lines of sight. The STEREO-A view shows that when the prominence aligns along the line of sight (the northern third in STEREO-A, where the crosses range in color from green to red), the cool plasma often appears to extend down to the chromosphere. When viewed side-on (the middle third in STEREO-A, where the crosses are purple and blue), the prominence is suspended above coronal material. In the absence of magnetic support, this situation is Raleigh-Taylor unstable. Prominences can stably exist for weeks on end, while the free-fall time is on the order of an hour. Due to these considerations, the prominence must be supported by the magnetic field.

One of the fundamental aspects of the corona is that it is magnetically dominated. Typically, plasmas are described in terms of β,

$$\beta = \frac{8\pi p}{B^2},$$

where p is pressure and B is the magnetic field. The pressure of a completely ionized hydrogen plasma in typical coronal conditions ($n_e = 5 \times 10^8$ cm^{-3}, T=1.2 MK) is approximately,

$$p = 2nkT = 0.17 \text{ dyne cm}^{-2}$$

The magnitude of the magnetic field is a tougher quantity to lock down. Magnetic measurements based on Zeeman and Hanle effects have become routine in the lower solar atmosphere, but this has yet to be comprehensively extended into the corona. Predictions based on extrapolation techniques and the few remote sensing measurements [Lin et al., 2004, Tomczyk et al., 2008] point to a coronal magnetic field of 10 Gauss in the quiet sun at a height of 1.1 $R_\odot$ (70 Mm). With these estimates

$$\beta = 0.043$$

This small-β ($<< 1$) implies that the corona is *magnetically dominated*. It has been shown by de Bruyne (1993) that given these conditions the magnetic field stabilizes coronal loops against the Rayleigh-Taylor instability.

The most direct method to visualize the implications for a low-β plasma is to consider time-independent momentum equation:

$$\mathbf{j} \times \mathbf{B} = -\nabla p + \rho \mathbf{g} \tag{1.1}$$

which is the balance of the Lorentz force, the gas pressure gradient, and gravity. If we look at the scales of these terms for typical coronal parameters

$$\frac{\mathbf{j} \times \mathbf{B}}{\rho \mathbf{g}} \approx \frac{1}{\beta p L \rho g} \approx 10^4 \tag{1.2}$$

$$\frac{\nabla p}{\rho \mathbf{g}} \approx \frac{p}{L \rho g} \approx 5 \tag{1.3}$$

where L represents the length of a coronal field line. The Lorentz term cannot be balanced by the much smaller pressure or gravitational terms. Thus, the corona tends towards a force-free state of

$$\mathbf{j} \times \mathbf{B} = \mathbf{0} \tag{1.4}$$

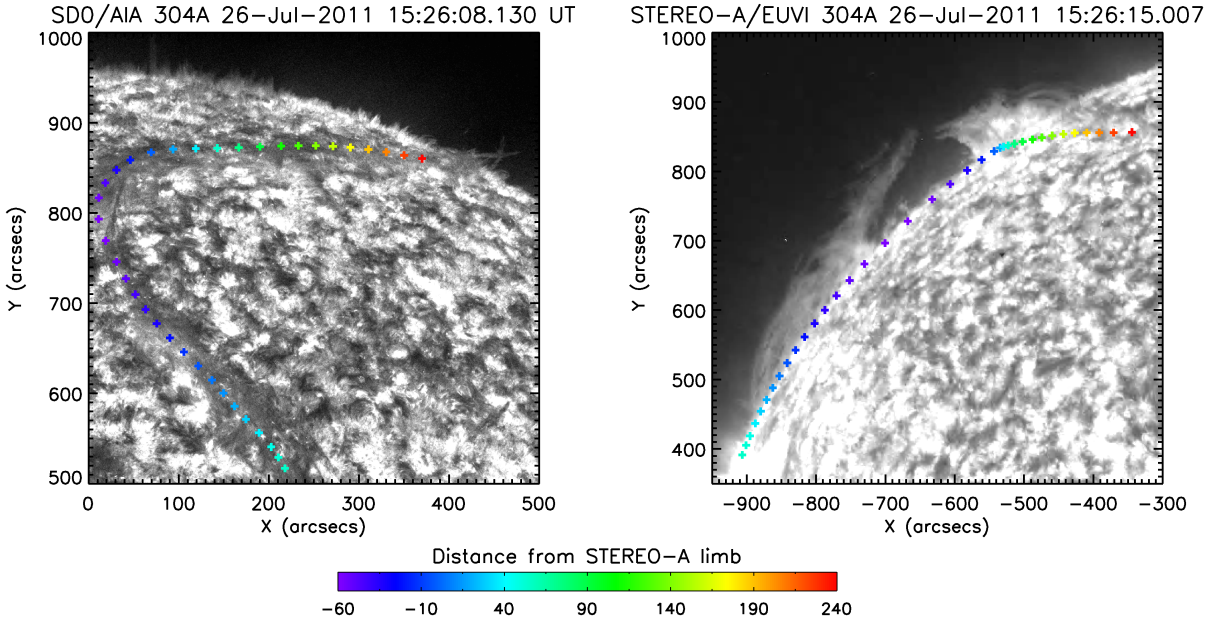

Figure 1.2 EUV observations of a prominence from two vantage points (HeII 304Å). Left: an on-disk filament appears as a continuous dark structure in AIA. Colored crosses overlie the filament. Right: the same prominence observed simultaneously from the STEREO-A spacecraft which was 110° ahead of Earth in an 1 AU orbit. The color of the crosses denotes the position in or out of the plane of the sky from the STEREO-A vantage.

The force-free equation dictates the state of the magnetic field. However, by definition the Lorentz force acts solely across the magnetic field. Pressure balance still matters in the corona, but only along the magnetic field. The non-Lorentz terms of the momentum equation can be written in the form:

$$\frac{dp}{ds} = \rho(\mathbf{g} \cdot \hat{\mathbf{s}}) \tag{1.5}$$

$$\hat{\mathbf{s}} \times \mathbf{B} = 0 \tag{1.6}$$

where $\hat{s}$ is the local magnetic direction.

The magnetic field supports prominence mass against gravity where it is has a component normal to gravity. For this reason, it is fundamental that prominences must occur along horizontal magnetic fields. More specifically, magnetic field lines need to be dipped so that the horizontal field acts as a well to stably support dense, prominence plasma. There is an observational consequence to this geometry. Figure 1.3 shows an overlay of the position of filaments on a map of the radial magnetic field at the photosphere. Prominences occur over regions where the radial magnetic field changes sign. These neutral lines will either have a concave-down (arched field) or concave-up (dipped field) geometry in the overlying corona.

This analysis has introduced the fundamental constraint for magnetic prominence models: what are stable magnetic configurations which have dipped field lines? To address this question, solutions to the magnetohydrodynamic (MHD) equations are sought. The ideal MHD equations are

$$\frac{\partial \rho}{\partial t} + \nabla \cdot (\rho \mathbf{v}) = 0 \tag{1.7}$$

$$\rho \frac{D\mathbf{v}}{Dt} = -\nabla p - \mathbf{j} \times \mathbf{B} + \rho \mathbf{g} \tag{1.8}$$

$$\frac{\partial \mathbf{B}}{\partial t} = \nabla \times (\mathbf{v} \times \mathbf{B}) \tag{1.9}$$

where pressure is defined by the ideal gas law and current is given by

$$\mathbf{j} = \frac{1}{4\pi}(\nabla \times \mathbf{B})$$

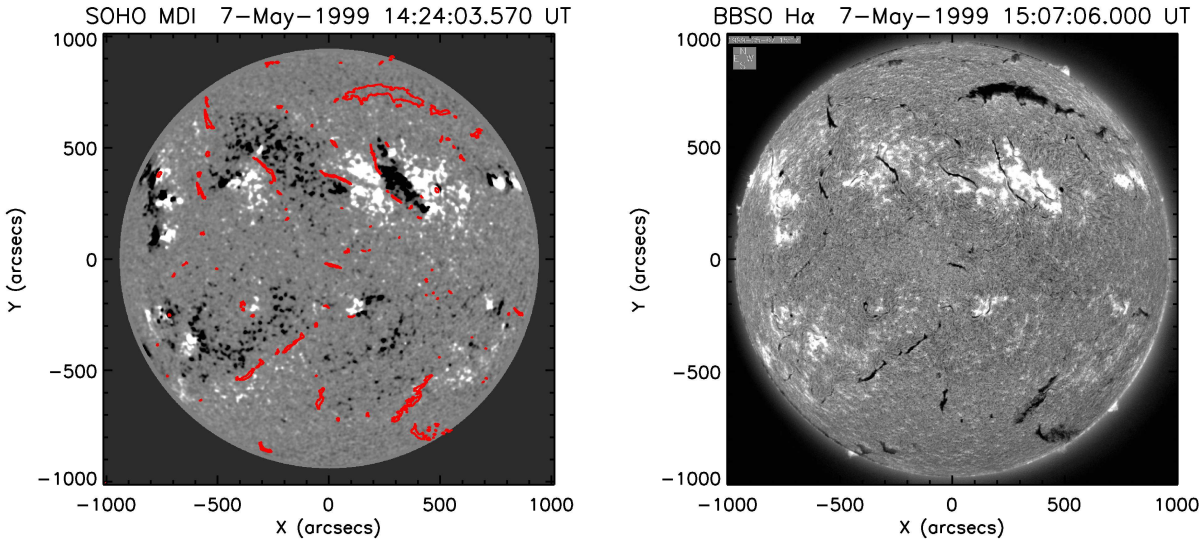

Figure 1.3 Filaments are found on magnetic neutral lines. Right: Hydrogen α emission (656nm) observed at the Big Bear Solar Observatory. Filaments (on-disk prominences) appear as dark absorption features. Left: SOHO/MDI magnetogram which measures the magnetic field strength at the photosphere using the Zeeman effect. Black and white represent positive and negative magnetic polarities respectively. The red contours show the location of Hα filaments. Neutral lines allow for the formation of stably dipped magnetic field lines in the corona.

These equations can be solved to find steady equilibrium for the magnetized plasma that fills the corona. Typically, they are solved according to a prescribed lower boundary condition where the magnetic field is "line-tied" to the high-β photosphere.

The simplest (non-trivial) magnetic field solution based on this spherical boundary value problem is a potential field [Schatten et al., 1969]. A potential field is current-free, and it has been shown that this magnetic field represents the lowest energy state given the boundary conditions [Woltjer, 1958]. In general, potential fields do not contain dipped field lines, and thus the theoretical work on prominence structure has focused on the methods of adding energy (i.e. currents) to simple magnetic fields such that non-potential dipped structures are created.

The seminal work on the support of a prominence through currents is Kuperus and Raadu [1974, hereafter KR74]. The authors found that a line current embedded within an axisymmetric potential arcade can exist in stable magnetostatic equilibrium. The force balance in KR74 relies on the Lorentz repulsion between the coronal line current and the subsurface potential field current. Figure 1.4 illustrates the cartoon setup envisioned in KR74. This paper was important for two reasons. First, this theoretical prominence model was later found to match the spectropolarimetric observations of the general magnetic orientation within prominence plasma [Leroy et al., 1984] . The authors found that a majority of prominences exhibited an inverse polarity orientation where the prominence field is antiparallel from the underlying photospheric magnetic field. Inverse polarity is a feature associated with the Kuperus-Raadu model while the other leading prominence model, Kippenhahn and Schlüter [1957], featured a normal polarity. Second, the Kuperus-Raadu showed that currents could effectively create dipped fields and stably support that configuration.

The magnetic structure of the corona is shaped by its lower boundary layer. The internal dynamo of the Sun produces buoyant magnetic flux elements which rise through the convective zone until we are able to remotely observe their presence at the last photon scattering layer, the photosphere. In terms of magnetostatics, the photosphere provides a physical lower boundary condition to coronal magnetic models. The photosphere is however not a static, isotropic layer. The photosphere is located near the top of the turbulent convective zone, where the thermal and

Figure 1.4 Diagram of the Kuperus-Raadu model for the prominence magnetic field. Magnetic fields line are depicted in the corona with foot points in the photosphere. A line current is superimposed on a potential field formed by a sub-photosphere virtual current. Both these magnetic configurations create dipped magnetic fields, where prominence material can collect. Figure taken from Kuperus and Raadu, 1974.

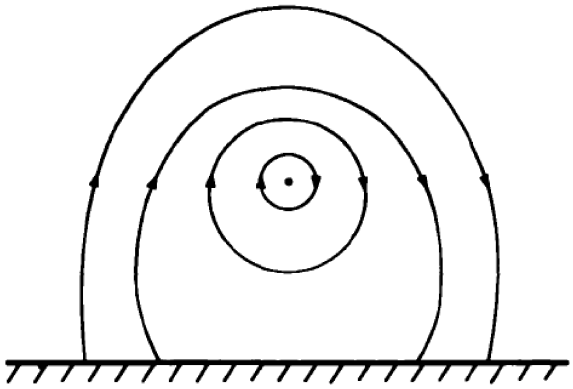

kinetic energy of the plasma dominate the magnetic energy. What does this mean for the corona? It means that lower boundary for the corona is inherently time-dependent. The corona gets passively dragged along with this lower boundary. These principles mean that the magnetic field of the corona undergoes a constant *energization* from the photosphere [Parker, 1972, Sakurai, 1979]. Additionally, currents may form in lower in the solar atmosphere and buoyantly emerge into the corona. Both of these processes introduce currents into the corona.

1.2.2 Overview of MHD Prominence Models

The focus of magnetic prominence modeling has been finding equilibrium magnetic configurations which contain magnetic dips. In this section, we will briefly describe the numerical experiments that have been done to understand the effects that various foot point motions or flux emergence have on the overlying coronal field. The nature of these models do not promote a direct, quantitative comparison due to differences in boundary conditions.

One simple mechanism for stressing is shear flows. A model was developed by Antiochos et al. [1994] who numerically solved the time-dependent 3D MHD equations. A potential arcade is subjected to a lateral velocity at the magnetic foot points. The velocity profile decreases with distance from the $B_r = 0$ neutral line such that the outer arcade maintains its original foot point locations. This unperturbed field acts as a restraining force and the sheared field gains energy. The stressed magnetic field forms dips underneath the unstressed field. Some example field lines from the sheared arcade model are shown in Figure 1.5.

van Ballegooijen and Martens [1999] solved the MHD equations using a different foot point velocity profile. They added a convergent flow to the unidirectional antiparallel flow of Antiochos et al. Sheared magnetic elements converge along the neutral line, reconnect, and form dipped field over the neutral line. The notable difference between this model and the sheared arcade model is the twist which is present in the final magnetic field. In this axisymmetric model, the reconnection process actually creates detached magnetic flux similar to Figure 1.4. This magnetic structure is referred to as a flux rope due to wrapping of the field lines. Low and Hundhausen [1995] found

Figure 1.5 Magnetic field lines in the sheared arcade model. A unilateral shear is applied along a neutral line of a potential magnetic arcade. The stressing creates dips along the stressed, line-tied field. There no twist present in the dipped field. Figure taken from Antiochos, 1994.

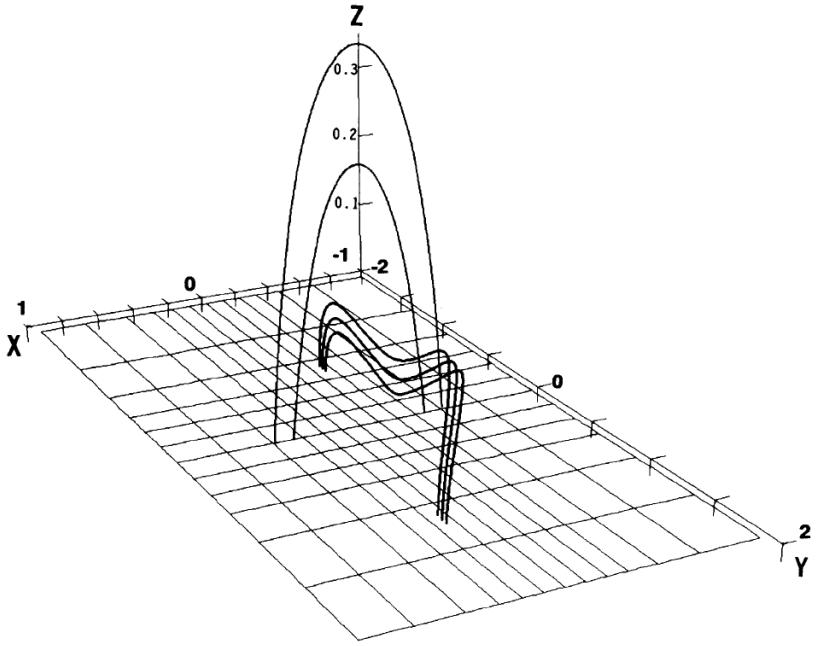

the first analytic solutions for a flux rope embedded in a potential field in axisymmetric, spherical geometry.

Flux ropes have also been modeled in 3D as well. Rather than forming a flux rope via surface motions, the Fan-Gibson model [Fan and Gibson, 2004, Gibson and Fan, 2006] emerges a twisted magnetic tube from the upper convective zone into the corona. It is reasonable to assume that the ascension through turbulent convection could produce twisted-tubes more effectively than surface shear [Longcope et al., 1996, Démoulin et al., 2002]. It is also been suggested that twist strongly aids magnetic fields to survive the shredding action of the ascension [Zwaan, 1978, Abbett et al., 2004]. This emergent flux rope differs from the 2D axisymmetric models such that the field lines that were detached now have photospheric foot points. Examples of field lines in the Fan-Gibson flux rope are shown in Figure 1.6.

One of the central issues that is still debated in the prominence community is how much twist is present in the quiescent field. The sheared arcade model features very little twist to the field, whereas a full-to-multiple winding is necessary in the flux rope interpretation. The presence of twist plays a role in determining which mechanism drives eruptions. Flux ropes undoubtably exist post-eruption, and there is a limit to how much twist can be in equilibrium in the corona.

Eruptions are the primary manner in which prominences end their evolution. Prominence eruptions often result in coronal mass ejections (CMEs) which are an important source of space weather [Kahler, 1992]. In situ observations have shown that CMEs often have the signature of a strong axial magnetic field with a weaker normal component which rotates about the primary axis as a function of position within the CME [Gosling et al., 1995, Burlaga and Lepping, 1977]. These solar wind flux ropes are directly analogous to the coronal structure suggested by Fan and Gibson. One theory is that solar wind flux ropes exist as a consequence of reconnection during the eruption process [Lynch et al., 2004]. An opposing theory argues that a coronal flux rope goes unstable as a result of the twist through a kink or torus instability [Fan and Gibson, 2004] .

Related to this debate is the question of how much twist can stably exist in the corona. This problem is very condition specific: how much potential field surrounds the twist, how gradual is

Figure 1.6 The Kuperus-Raadu flux rope extended into three dimensions via numerical MHD modeling. The Fan and Gibson model rises a pre-twisted flux rope structure into the corona. Several different magnetic topologies exist within the flux rope, as the colored field lines show. Not all are twisted or dipped. Data cube of equilibrium magnetic field taken from Fan and Gibson, 2006.

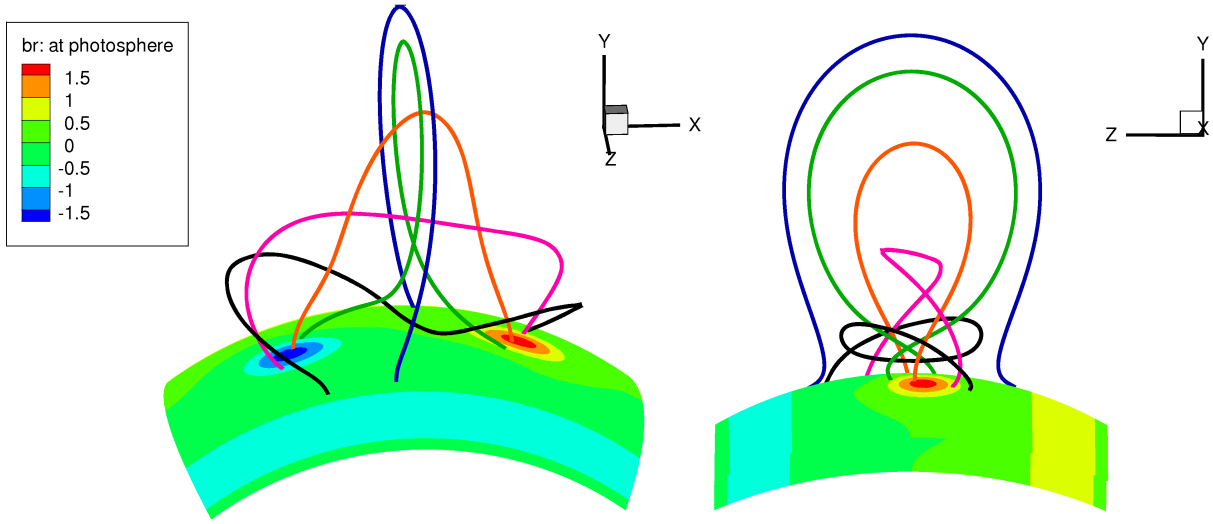

the twisting profile, what is the magnitude of the axial field? Hood and Priest [1979] calculated that a force-free symmetric, cylindrical flux rope was stable against the kink instability up to 3.3π radians of twist over the length of an individual field line. Others authors have constructed flux ropes with more twist [Lionello et al., 2002] which implies the Hood calculation does not provide a univerisal twist limit.

Throughout most of these models, the cavity has been a neglected constraint on prominence structure. In a notable exception, Low and Hundhausen [1995] consider the role that the thermodynamic properties play in the magnetostatic solution. The authors point out that given gas pressure gradients across magnetic field lines, non-force-free currents must also be present. Using the force-free solution and a prescribed density field, they calculate the necessary cross-field currents for magnetostatic cavity structure.

Stepping back, it is important to notice that we have not closed the system Equation 1.7-1.9 introduced. The equation which considers time-dependent changes in pressure, the thermal energy equation, is missing. The magnetic structure of the corona is generally taken to be force free. Numerical MHD models by-and-large have expedited their solutions by using an isothermal or adiabatic equation to close the system. While the force-free MHD solution accurately describes the structure of the corona across field lines, the solution along field lines is not accurate. We will develop through this thesis, how an accurate energy equation is important, and what we can learn from the coupled magnetic-thermal system.

1.3 Energetic Balance in Prominences

Throughout the discussion in the previous section, we describe the physics that allows a levitating, cold, dense prominence to exist the corona in the corona. We have not discussed at all where that mass comes from. In this section, we will develop a physical intuition for coronal energy balance. Prominences are a fundamental stellar phenomena because of energy balance.

To understand why prominences exist, we must first understand why the corona exists. As detailed in Section 1.2, the 3D momentum equation that describes the force balance of the corona

can be divided into a 3D magnetostatic component (Equation 1.4), and a 1D field-aligned hydrostatic component (Equation 1.5). If we reintroduce the time-dependency into Equation 1.5, we have

$$\rho\left(\frac{\partial v}{\partial t}+v\frac{\partial v}{\partial s}\right)=-\frac{\partial p}{ds}-\rho g_s \tag{1.10}$$

where v is the velocity, p is the gas pressure, ρ is the mass density, and g_s is gravity component parallel to the field. The terms on the lefthand side of Equation 1.10 represent the momentum associated with motions of the plasma.

The second equation we must consider is the energy equation. In a magnetically-dominated stellar atmosphere, the energy equation is

$$\frac{1}{\gamma-1}\left[\frac{Dp}{Dt}+\frac{p}{\rho}\,\frac{D\rho}{Dt}\right]=\alpha\frac{\partial^2}{\partial s^2}T^{7/2}-n^2\Lambda(T)+E(s,t) \tag{1.11}$$

with the operator definition

$$\frac{D}{Dt}=\frac{\partial}{\partial t}+v\frac{\partial}{\partial s}$$

where p is pressure, T is temperature, n is number density, v is velocity,γ is the adiabatic coefficient, α is the conduction coefficient, Λ is the temperature-dependent radiative loss function, and E is coronal heating. The terms in Equation 1.11 represent enthalpy, thermal conduction, radiative losses, and heating, respectively. The physical nature of these terms are discussed in detail in Appendix A.

1.3.1 Coronal Energy Balance

The energetics of a prominence are closely related to the energetics and stability of the corona. To understand the system, we must address how the different terms in Equation 1.11 balance. Let us now simplify these equations. If we consider a hydrostatic atmosphere, the lefthand side of Equation 1.10 and 1.11 are zero. We can further reduce the system by expanding the pressure gradient term using the ideal gas law

$$\frac{dp}{ds}=2k\left(T\frac{dn}{ds}+n\frac{dT}{ds}\right) \tag{1.12}$$

and rewriting the conduction term in Equation 1.10 in the form

$$\frac{dF_c}{\partial s} = \frac{d}{ds}\left(\alpha T^{5/2}\frac{dT}{ds}\right) \tag{1.13}$$

where F_c represents the conductive flux. We can then substitute Equation 1.13 into Equation 1.12 and 1.11 and Equation 1.12 into Equation 1.10. These lead us to the equations for hydrostatic balance in the corona,

$$\frac{dn}{ds} = -\frac{n}{2kT}\left(mg + \frac{kF_c}{\alpha T^{5/2}}\right) \tag{1.14}$$

$$\frac{dT}{ds} = \frac{F_c}{\alpha T^{5/2}} \tag{1.15}$$

$$\frac{dF_c}{ds} = E - n^2\Lambda \tag{1.16}$$

which is a third order ordinary differential equation, for the density, temperature, and conductive flux. This equation can be solved using numerical integration (which is detailed in Section 4.2.4). The solution to these equations for a foot-point-heated, circular half loop are shown in Figure 1.7. Let us discuss a few important aspects of this loop.

In the loop displayed in Figure 1.7, the temperature at the loops boundary is set to 3×10^4 K. This temperature is characteristic of the chromosphere. The temperature gradient (and the conductive flux) are also set to zero at this lower boundary. Within a distance of 2 Mm, the temperature of loop rises from 3×10^4 K to 6×10^5 K, and the density drops from 2×10^{10} cm^{-3} to 2×10^9 cm^{-3} . The atmospheric region between the chromosphere and the corona is the transition region. While strong density and temperature gradients are characteristic of the transition region, these gradients are very much reduced throughout the coronal region of the loop.

The transition region is most easily explained through an examination of the energy equation. At the chromosphere, energy balance occurs primarily between heat input and radiative losses

$$E - n^2\Lambda = 0$$

where the temperature-dependent function $\Lambda(T)$ is shown in Figure A.1. The chromosphere is high density, which leads to the fast collision rates and strong radiative losses.

The solar atmosphere is gravitationally stratified such that as density decreases as a function of radial height. As the loop ascends upward from the chromosphere, collisions occur less frequently and the density-squared factor of the radiative loss term weakens. For radiative losses to continue to balance heat input (which is assumed to be uniform as a function of height), the Λ component must increase as function of height. The quantity, $d\Lambda/dT$, is positive at chromospheric temperatures. A positive temperature gradient in the chromosphere allows the radiative term and the heating term to maintain balance. Thus, the radial temperature profile for the solar atmosphere will gradually increase as function of height in the temperature regime where $d\Lambda/dT$ is positive.

Given a solar abundance plasma, Λ reachs a maximum near 10^5 K. This corresponds with strong UV emission from carbon, nitrogen, and oxygen. At temperatures above 10^5 K, the plasma is less efficient at radiating and $d\Lambda/dT$ is negative. At the radial height at which this temperature threshold is reached, radiative losses can no longer balance energy input. Thus, a rapid increase in temperature occurs such that conduction acts to balance heat input. Thermal conduction is nonlinear in plasmas as both the thermal conductivity (units of erg cm^{-1} s^{-1} K^{-1}) and temperature-gradient terms are temperature dependent. The corona is conductively dominated, and conduction acts to redistribute the energy, which cannot be radiated from the corona, into the chromosphere where it can be effectively radiated. As pressure balance must be maintained, the transition region allows exhibit a rapid density drop.

This energy balance gives rise to the temperature and density profiles which are plotted in Figure 1.7. The corona is approximately 1 MK and nearly isothermal. The transition regions is 1 Mm thick and represent the rapid transition for the radiatively dominated energy balance (chromosphere) to conductively dominated (corona). A flowchart showing the effects that create the transition region is shown in Figure 1.8.

1.3.2 Thermal Instability

We have described the hydrostatic equilibrium of the corona, but we have not described the stability of that balance. To check the stability of coronal equilibrium, we will conduct a linear

Figure 1.7 Hydrostatic balance in a circular half loop. Temperature, density, conductive flux, energy contributions (top to bottom respectively) as a function of position along the loop. x=5.5×10^9 cm represents the loop midpoint about which the solutions are symmetric. The solutions are dependent on two quantities: density at the lower boundary and the coronal heating distribution.

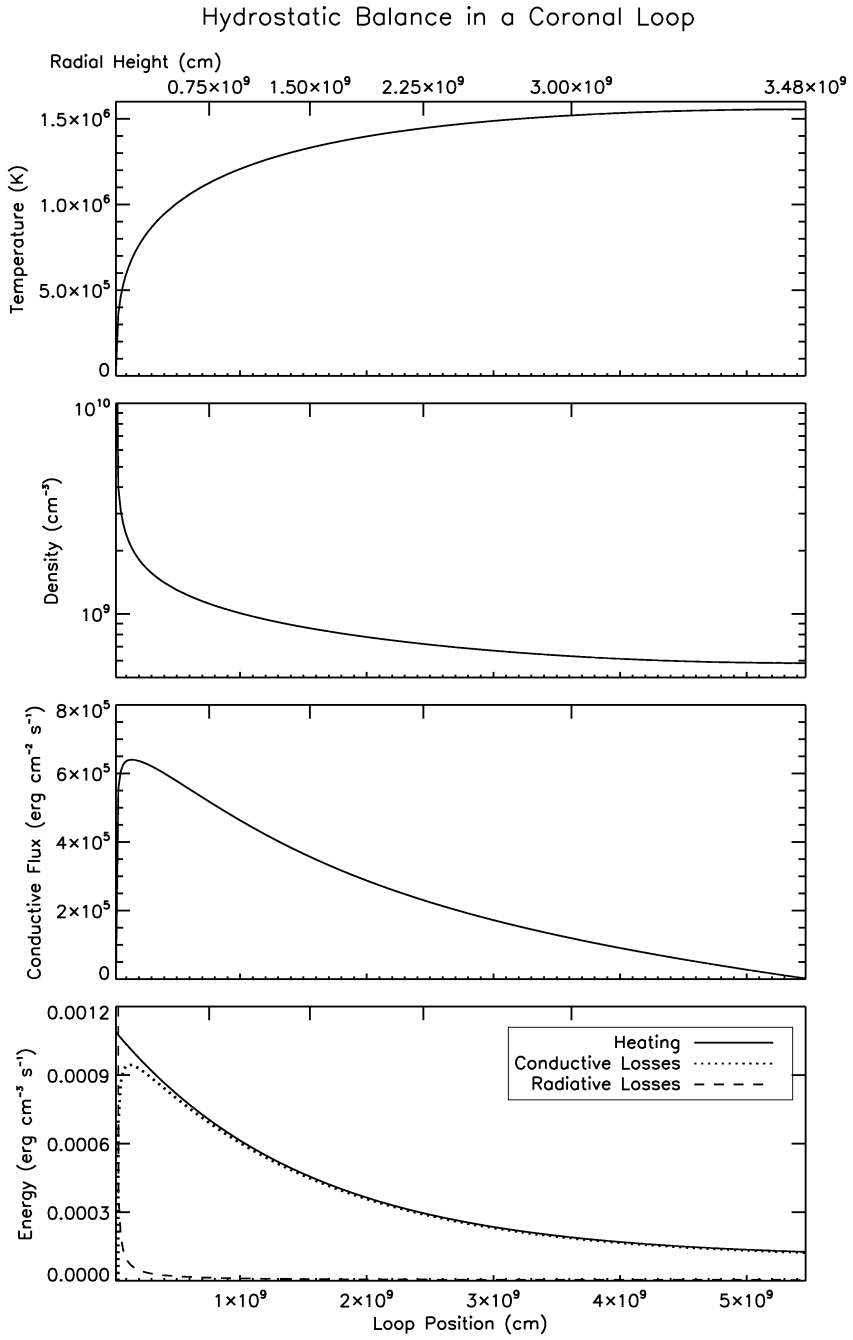

Figure 1.8 Flowchart representing the approximate process that leads to the formation of the transition region and corona. (1) The chromosphere sits 500 km above the photosphere near 3×10^4 K and 10^{10} cm^{-3}. It is heated by an unknown energy source ($\approx 10^{-5}$ erg s^{-1} cm^{-3}). (2) Pressure balance leads to radial density falloff. (3) The decreasing collisional term in radiative losses is balanced by an increasing temperature. The solar radiative loss function has a positive slope (as a function of temperate) between $10^4 - 10^5$ K. (4) The radiative loss function hits a maximum at a temperature of 10^5 K, and a temperature increase leads to decreased radiative losses. (5) The radiation term can no longer balance the heating term at this height. (6) The temperature now rapidly rises. (7) A new energy balance is established where heat input is conducted down to chromosphere where it can be effectively radiated.

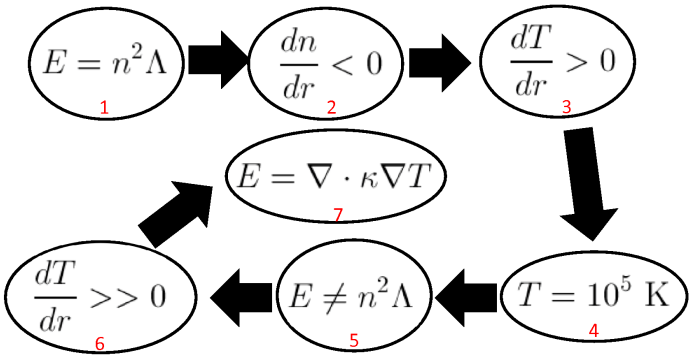

perturbation analysis. We assume that the thermodynamic variables of the corona can be written in the form

$$a(s,t) = a_0 + a_1 \exp(iks + \nu t)$$

where a_0 is the variable's value in equilibrium and a_1 is the perturbed value which varies as a function of wavenumber k and frequency ν. A closed system of equations is provided by combining Equation 1.10, 1.11, and the conservation of mass

$$\frac{\nu}{\gamma - 1} p_1 - \frac{\nu \gamma p_0}{(\gamma - 1)\rho_0} = -k^2 \kappa_0 T_1 - n_0^2 T_1 \frac{d\Lambda}{dT}_{T_0} - n_0 n_1 \Lambda_{T_0} \tag{1.17}$$

$$\nu \rho_0 v_1 = -ikp_1 \tag{1.18}$$

$$\nu \rho_1 + ik\rho_0 v_1 = 0. \tag{1.19}$$

where ρ is the mass density (μn) and κ_0 is the thermal conductivity at the equilibrium temperature. We can algebraically reduce the system into a cubic characteristic equation for the perturbation growth rate

$$\nu^3 + \nu^2 \frac{\gamma - 1}{\mu k_B} \left(\frac{d\Lambda}{dT}_{T_0} \rho_0 + \frac{\mu^2 \kappa_0 k^2}{\rho_0} \right) + \nu c^2 k^2 + \frac{(\gamma - 1)c^2}{\gamma \mu k_B} \left(\frac{d\Lambda}{dT}_{T_0} \rho_0 k^2 - \Lambda_{T_0} \rho_0 \frac{\gamma k_B}{c^2 \mu} k^2 + \frac{\mu^2}{\gamma - 1} \frac{\kappa_0}{\rho_0} k^4 \right) = 0 \tag{1.20}$$

where k_B is the Boltzmann constant. The sign and reality of the roots of this equation provide the stability (a negative or zero real component) or instability (a positive real component) of the plasma to the associated perturbation. Two roots correspond to sound waves (isothermal and isochoric modes). The third root corresponds with an isobaric perturbation where the density and temperature perturbations are out of phase. This is referred to as the condensation mode. The growth rate for the condensation mode can be written by substituting the $p_1 = 0$ into Equation 1.17

$$\nu = \frac{\gamma - 1}{c^2} \left(n_0 n_1 \Lambda_{T_0} + n_0^2 T_1 \frac{d\Lambda}{dT}_{T_0} + k^2 \kappa_0 T_1 \right) \tag{1.21}$$

If we consider the coronal temperature regime of the radiative loss curve, the first and second terms on the righthand side Equation 1.21 are both positive for a cooling isobaric perturbation

($T_1 < 0, n_1 > 0$). The third term represents conduction. It is the only term to depend on the spatial scale of the perturbation, and this term acts to stabilize the system against high wavenumber perturbations. Thus large-scale isobaric perturbations will have a positive growth rate in the corona. The driving factor in this instability is radiative losses and specifically the negative slope of the radiative loss function at coronal temperatures.

The idea of thermal instability in the corona was originally introduced by Parker [1953] and a rigorous mathematical study was conducted by Field [1965]. A later paper, Antiochos [1979], extended this analysis to coronal loops. The authors addressed the thermal instability in the conductively-dominated coronal regime and looked for perturbations which would fit appropriate boundary conditions for an entire loop, not just localized perturbations as discussed in previous section.

The thermal instability of the corona offers us an explanation for the existance of prominences. Prominences are produced by thermally unstable coronal loops which cool into a radiatively-dominated energy balanceat temperatures below 10^5 K.

1.3.3 Overview of Energetic Models of Prominence Formation

There have been three numerical experiments which have tried to study thermal instability in coronal loops in a time-dependent manner. The mechanisms of they have used to drive instability are: field line stretching, heat reduction, and foot point heating.

Choe and Lee [1992] is the primary work to describe mechanically formed condensation. The authors numerically solve the magnetic and energetic equilibrium for a linearly sheared axisymmetric potential arcade. They find that the shearing process produces both magnetic dips on the order of 36 hours(4 km s^{-1} maximum driving shear) and a condensation (on the order of 2 hours). The condensation is driven by the expansion of the field and the resulting adiabatic cooling. An important consideration to this model is the rigid (zero mass flux) lower boundary. As the field is sheared, the average density and the loop pressure decrease inversely with the increasing field volume. Though there are no set boundary conditions that are universally accepted for coronal loops,

the constant-mass condition is arguably not physical. The lower layers of the solar atmosphere should act as reservoir of additional mass which will be suctioned into the corona as the field line expands.

A more direct method to thermally destabilizing a corona loop comes from the changes to the energy input. Poland and Mariska [1986] conducted an experiment where they attempted to produce a prominence by drastically reducing the energy input throughout a loop. Instead of creating a condensation, this heat-reduction resulted in a evacuation, where gravity dominates the dynamics and the loop top mass fell to the foot points. This scenario has been rejected as a prominence-formation mechanism.

Antiochos and Klimchuk [1991] conducted the opposite experiment. They increased heating near the chromosphere of a coronal loop. The increased heating rate increased the pressure at the foot points and pushed plasma into the upper loop. The convergent flow leads to a density buildup in the loop. The increased density leads to an increase in coronal radiative losses. This results in a large-scale (> 15 Mm) catastrophically-cooling segment of the loop. This process is known as the *thermal non-equilibrium model* (TNE model). The term "non-equilibrium" refers to the fact that given this foot point heating there are no coronal-temperature equilibrium loop solutions. In Chapter 4, we provide a detailed discussion of the TNE model.

1.4 Extreme Ultraviolet Emission in the Corona

In this dissertation, we will be using remote sensing observations of extreme ultraviolet (EUV) radiation from the corona to diagnose the prominence-cavity system. The EUV range of the electromagnetic spectrum sits in between the far ultraviolet and soft x-rays. For the purposes of this dissertation, this range with be considered to be between 50 Å and 500 Å. This spectral regime is characterized by atomic line emission from highly ionized, heavy atomic species. A free-bound continuum also exists primarily from He I and He II. EUV emission plays an important role in coronal physics for two primary reasons. First, the EUV spectra provides a diagnostic tool of the emitting plasma because information on the thermodynamic state of the corona is encoded within

the spectral lines. Second, EUV emission plays a primary role as an energy sink in coronal energy balance.

1.4.1 Line Emission

The corona is optically thin in the EUV, barring particular lines (HeII 304Å or specific circumstances such as bound-free absorption in prominence material). The observed intensity of coronal EUV emission lines can be described:

$$I_{ji} = \int G_{X,ji}(n,T)\ n_e n_X d\ell \quad [\text{erg cm}^{-3}\ \text{s}^{-1}] \tag{1.22}$$

where n_X is the ion number density and n_e is the electron density,ℓ is the position along the line of sight. These terms represent the fact that the excitation state of coronal ions is dominated by free electron collisions. The collision term is integrated along the line of sight multiplicatively with the contribution function, $G_{X,ji}(n,T)$. The contribution function contains the atomic physics that describe the electronic transition. It represents the fundamental strength of the electron level $j \rightarrow i$ radiative transition and the number of atoms of ion species X in the excited state j. The contribution function combines these factors

$$\begin{array}{rccccc} G_{Xji} = & \frac{n_{Xj}}{n_{X1}} & \frac{n_X}{\Sigma n_X} & \frac{\Sigma n_X}{\Sigma n} & \frac{\Sigma n}{n_e} & \frac{A_{ji}hc}{n_e\lambda_{ij}} \\ & 1 & 2 & 3 & 4 & 5 \end{array} \tag{1.23}$$

Term 1 represents the fractional population of ion species X in electron state j relative to the ground state. This term is derived from the collisional cross section and the spontaneous emission rates of level j. Terms 2 and 3 represent the fractional population of iso-elemental atoms in ionization level X relative to the total abundance of the element. The fundamental quantities important here are the ionization and recombination cross sections of the element. Term 4 is the elemental abundance. Term 5 represent the energy and the timescale of emission between levels j and i per electron collision.

In this thesis,we will use EUV emission to diagnosis the thermodynamic properties of the corona. These diagnostics are based the relative population of electron levels (of a given ion

species) or the relative population of ions (of a given atomic species) which depend on the density and temperature of the emitting plasma.

1.4.2 Line Diagnostics

There are hundreds of measured emission lines in the EUV spectra. As described above, the relative intensities is dictated by the properties of the emitting plasma. One common analysis for the corona is diagnosing the temperature of the corona by analyzing emission lines from different ionization states of the same element. Iron is typically used because it is an important contributor to the coronal spectrum, and exhibits strong EUV emission lines from most ionization states. Figure 1.9 shows the ionization equilibrium for iron as a function of temperature. In the corona, these populations are determined by the rates of ionization and recombination. A hotter plasma contains more energetic electrons which are more likely to collisionally ionize an atom and less likely to radiatively combine.

The structure of the corona varies as a function of temperature. Regions of strong magnetic field often emit strongly in Fe XVI 335Å, while the quiet-sun corona does not emit at all in that line. It emits most strongly in Fe XII 193Å. This basic comparison of emission suggests that the quiet-sun corona is cooler than active regions. This approximation can be extended using a technique known as *differential emission measure* analysis [Batstone et al., 1970], although the inherent errors in the atomic data can cause ambiguous results [Craig and Brown, 1976]. It's worth noting that the temperature-dependency of ionization can be quite broad, and thus temperature diagnostics have a coarse temperature resolution.

A more complicated line diagnostic is described in Appendix B. This line ratio technique compares two emission lines from the same ion but different excitation levels. Atomic physics dictates that the levels are populated differently as a function of density. The ratio of emission for the Fe XII 186.8Å and 195.1Å lines is thus a density diagnostic.

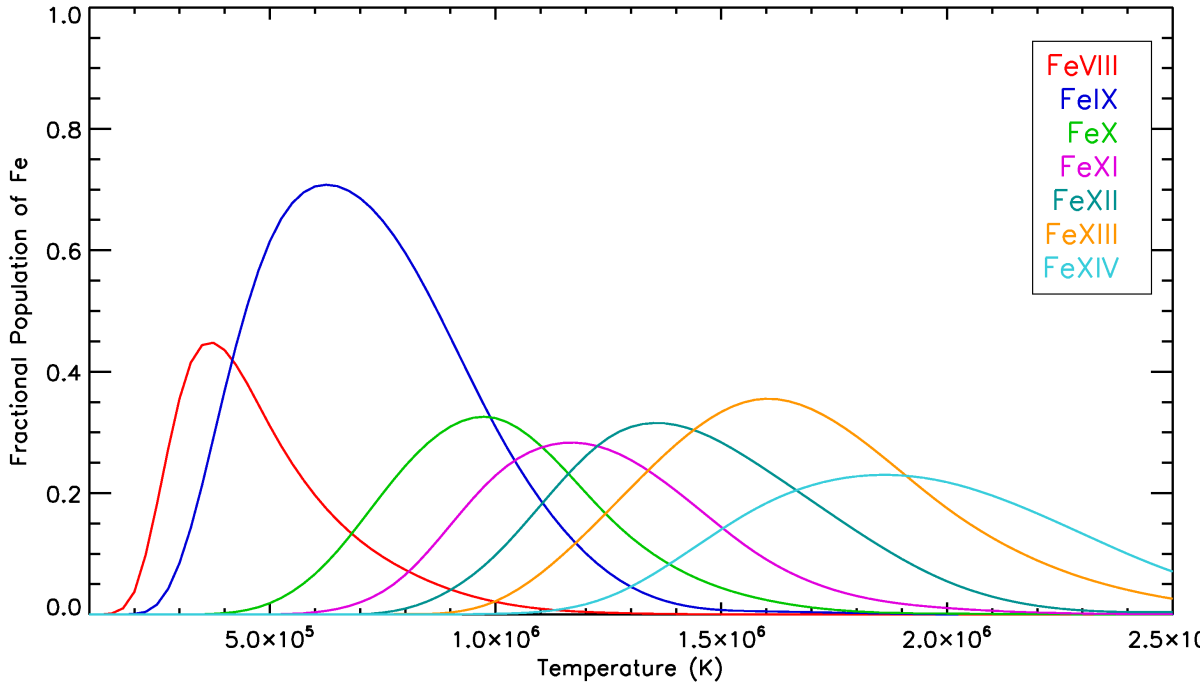

Figure 1.9 Populations for iron ion species as a function of temperature in equilibrium based on Arnaud and Raymond [1992].

1.4.3 Instruments and Data

In this thesis two EUV datasets are used. For imaging, the Solar Dynamics Observatory provides the Atmospheric Imaging Assembly (SDO/AIA) dataset. For spectroscopy, the Hinode observatory provides the EUV Imaging Spectrometer (EIS) dataset. Detailed specifications for AIA are provided in Section 2.3. AIA uses filters to provide high-spatial resolution images of the corona in spectral bandpasses centered on strong emission lines. AIA provides high-cadence observations (every 12 seconds in 6 bandpasses) of the full sun that allow us to complete our dynamics studies.

Detailed specifications for EIS in Section 3.2. EIS is a slit-grating spectrometer which resolves spectral line profiles. EIS allow us to diagnose the relative strength of various emission lines which provides details on the physical properties of the emitting plasma. EIS is capable of imaging, but this observing mode takes on the order of 2 hours for a cavity.

Two other, non-EUV datasets are used in this thesis. The Mauna Loa Solar Observatory (MLSO) provides the MK4 coronagraph data. The MK4 coronagraph images the scattered visible radiation of the corona. This provides a temperature-insensitive measurement of coronal density, which is used in Section 2.3. Data from the Coronal Multichannel Polarimeter (CoMP) is also used. CoMP makes spectropolarimetric observations of infrared coronal lines. These profiles provide Doppler velocities as well as magnetic field measurements. CoMP velocity data are used in Section 3.2.

1.5 Summary

The preceding sections detailed the basic physics which describe the prominence-cavity system and how we observe it. In the coming chapters, we will use this physics to address the magnetic link between the prominence and cavity. We will now present the results of our research.

Chapter 2

Diagnosing the Static Cavity

Cavities are a difficult structure to study through remote-sensing observations. The corona is optically thin throughout most of the electromagnetic spectrum (radio being the exception). In the optically thin limit, multiple coronal structures (coronal holes, active regions, etc.) can project along the line of sight, and convolute the observation. For cavities, this projection effect plays an even larger role due to their rarefied nature.

This chapter focuses on deriving a density profile (as a function of radial height) of a cavity by removing the projection effects. This diagnostic is accomplished by creating a structural model with radial density fall off. The cavity density is derived simultaneously with the surrounding streamer density through a genetic-algorithm powered χ^2 minimization.

This is not the first density diagnostic conducted on a cavity. Recently for example, Fuller and Gibson [2009] use a white-light inversion to measure the density of the cavity. Our analysis builds on these results by incorporating EUV observations and using a forward approach. These changes allow us to probe lower in the cavity and more directly measure the plane of the sky density.

The importance of our analysis is two-fold. First, the combination structural/density model developed here allows us to more generally assess the distribution of emission measure in cavity observations. This is useful when attempting to isolate the dynamic process described in Chapter 3. Second, the density of the cavity represents a constraint on the overall physical nature of the cavity. Can the cavity act as a mass source of the prominence? This is considered in Chapter 4.

2.1 Chapter Outline

In this work, we use EUV spectra in conjunction with white-light measurements to diagnose the density of the cavity through a forward-modeling process. Using the Extreme ultraviolet Imaging Spectrometer (EIS) aboard the Hinode spacecraft, we have observed a cavity in many spectral lines. In particular we use two lines, Fe XII 195.1Å and 186.6Å, in ratio as an indirect density diagnostic. Additionally, we have observed the polarization brightness of the cavity region with the Mauna Loa Solar Observatory MK4 coronagraph.

Using the structural morphology determined by Gibson et al. [2010], our analysis attempts to reproduce the observed line ratio and polarization brightness through forward modeling. A line-of-sight integral is carried out to determine the optically thin emission and scattering through a model corona. A genetic algorithm minimizes the χ^2 goodness-of-fit measure of the model calculation and the observed data. In this way, we determine a best-fit density model for the coronal cavity and the surrounding streamer.

Section 2 elaborates on previous research and datasets used. Section 3 discusses the synthesis of observables using the forward model and the goodness-of-fit minimization. Section 4 compares the best-fit model to the datasets and discusses the derived density profile. Section 5 discusses model errors and conclusions.

2.2 Background and Data

2.2.1 Previous Work

Observational diagnostics have been conducted on both the prominence and cavity to derive temperature and density. In the optically thick prominence, emission line profiles have been used to diagnose the plasma temperature and density [Vial et al., 2007, Labrosse et al., 2011]. The coolest regions of prominences are found to near 8000K and exceed 10^{10} cm^{-3}. Cavities have been the focus of white-light diagnostics as a density measure [Waldmeier, 1970, Fuller et al., 2008, Fuller and Gibson, 2009]. They find that cavities are density depleted up to 40% relative to streamers but

are at least twice as dense as coronal holes. These diagnostics rely on a inversion of the data which assumes a symmetric cavity. White light measurements cannot diagnose the temperature as the data is temperature-independent. X-ray observations [Hudson et al., 1999, Reeves et al., 2012] have revealed that some cavities have high-temperature substructure (>2 MK). Marqué [2004] observed the suspended cool, dense material in the cavity which was not associated with the Hα prominence. Vásquez et al. [2009] used a tomographic technique to extract density and temperature information on the cavity. They found that cavity structure had a broader distribution in temperature and that emission peaked at a hotter temperature than the streamer. A related but not cavity-specific diagnostic was completed by Orrall et al. [1990]. The authors compared EUV and white light observations to find that corona likely has highly-variable density structure in coronal holes.

2.2.2 Hinode/EIS

We use two instrument in this diagnostic: the Extreme ultraviolet Imaging Spectrometer (EIS) on Hinode and the MK4 coronagraph at the Mauna Loa Solar Observatory (MLSO). Hinode is a solar observatory in near-Earth orbit. There are three telescopes aboard Hinode: the Solar Optical Telescope (SOT),the X-Ray Telescope (XRT), and EIS. SOT provides high resolution and spectrally resolved observations of the photosphere and chromosphere. XRT images the hot corona in soft x-rays with 1" resolution. EIS observes emission lines from collisionally-excited bound-bound transitions in the highly ionized corona.

At the heart of EIS is a telescope is a normal-incidence reflector telescope. EIS uses a MoSi coated primary mirror that is coated as two separate hemispheres, each corresponding to a separate 40Å bandpass. Light reflected from the primary mirror is passed through a slit and is then incident on a toroidal diffraction grating. The first order diffracted spectra is projected onto two CCDs that observe the short wavelength (170-210Å, SW) and long wavelength (250-290Å, LW) spectra simultaneously. These data are two dimensional because the spatial resolution *along* the slit is retained. To form an image, a mechanical rastering must be done. A piezoelectric actuator mounted to the primary mirror shifts the light incident on the slit. By recording several exposures

with different mirror tilts, EIS composes a spectrally resolved image. Using the smallest slit, EIS has spatial resolution of 1". Spectral resolution is set by the grating line width and the slit width. EIS is capable of 0.05Å spectral resolution, but has CCD pixels which scale to 0.02Å.

Due to the nature of the multilayered coating on the optics, EIS has a variable effective area as a function of wavelength. The effective area for EIS peaks at the 195.1Å Fe XII line which sits in the middle of the SW band. The coatings of the primary make EIS a factor of 3 more sensitive in the SW band than the LW. The strongest lines are in the EIS spectral windows are characteristics of 1-2 MK plasma.

The EIS field of view is dependent on the choice of observations. To achieve maximum spectral resolution, the field of view for a single pointing is 1"×512" (1" corresponds with a 700 km spatial resolution at the sun). Cavities often range up to 150" in diameter so multiple raster steps are needed to observe a complete structure. Given the exposure duration, an EIS cavity study takes near 3 hours to complete.

Raw EIS spectra must be dark-current subtracted and flat fielded for calibration. Individual lines within the observed spectral windows are fit using a Gaussian profile. Errors are propagated from the individual errors per spectral pixel (which are dominated by Poisson-noise) into errors on the Gaussian parameters. The fitting methodology is described in Appendix C. The derived data product we use here are line intensities, which are measured in units of ergs s^{-1} cm^{-2} sr^{-1}. For this analysis, we use two lines in ratio, Fe XII 186.8Å and 195.1Å. These lines are described in Appendix B.

2.2.3 MLSO/MK4

The MK4 coronagraph has been observing continuously since 1998. It observes the white-light corona. MK4 employs 23 cm objective lens with a 395 cm focal length [Elmore et al., 2003]. An occulting disc is internally located within the optical assembly to mask the solar disk. A retarder is used to separate the linear-polarization states of incident radiation. The white-light corona is formed by photospheric blackbody radiation Thomson-scattering off the free electrons in the

corona. At 1.15 $R_\odot$ the white-light corona is 10^8 times fainter than the solar disk. The scattering process introduces a net polarization which is a function of the scattering angle. Because the Earth's atmosphere also scatters light, ground based coronagraphs can only observe the polarization brightness. The polarization brightness is measured by recording the I, Q, and U Stokes parameters as a function of solar latitude and altitude. The Q and U components are transferred into the solar polar coordinates where pB is defined by the difference between the flux polarized normal to the solar limb and tangential to it Billings [1966]. Being ground-based, MK4 is susceptible to atmospheric seeing conditions. Despite that caveat, MK4 is able to observe lower than any space-based coronagraphs due to the long focal length, single-reflection design.

MK4 observes the full-sun corona between 1.16 $R_\odot$ and 2.5 $R_\odot$. The detector of MK4 is a linear CCD array, and MK4 images the corona by scanning the radially oriented CCD through the azimuthal direction. The resolution of MK4 is 4.86" in the radial direction, and 0.5° in the azimuthal.

2.2.4 Specific Observations

In this chapter, we will use two specific observations to constrain the cavity density: EIS line ratio data and MK4 polarization brightness data. The EIS data were collected on 9-Aug-2007 at 14:00 UT over a 4 hour period. This study used the 1" slit and has a total field of view of 256"x256". The exposure time is 60s. To increase the signal-to-noise ratio, the spectral data have been binned 12"x12" before being Gaussian fit. Our dataset has 18" wide data gaps which are caused by the eclipsing orbit of Hinode. We use two spectral lines to produce a line-ratio image (shown in Figure 2.5a). The physics of the Fe XII 186.8Å-to-195.1Å ratio is described in Appendix B.

We also use MK4 data in this diagnostic. We have median-filtered the 113 MK4 scans between 17:00 UT and 23:59 UT 9-Aug-2007 to increase the signal-to-noise ratio of the data.

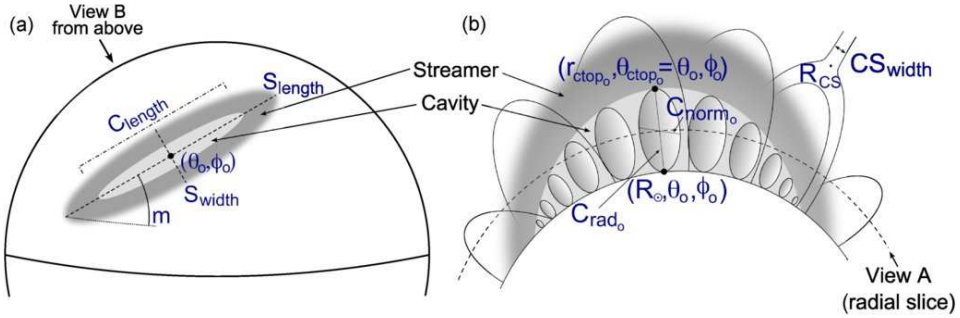

Figure 2.1 The three-dimensional structural model of Gibson et al. [2010] looking at a cavity/streamer on the solar disk (a) and off limb from a polar perspective (b). The cavity is formed as a torus of variable height. The streamer is defined by a three dimensional gaussian.

2.3 Methodology

We use a structural model to create synthetic observables which are directly comparable to our observations. The structural model, the synthesis of model data, and the model-to-data fitting routine are described in this section.

2.3.1 Morphology

The 9-Aug-2007 cavity was extensively observed from 5-Aug-2007 to 12-Aug-2007 as part of a multi-instrument campaign. Gibson et al. [2010] built a structural model of the corona, displayed in Figure 2.1, based on these observations. This model divides the three-dimensional corona into regions: cavity, streamer, and coronal hole. Streamers are regions of high density and closed magnetic field (see Figure 2.3a). Coronal holes are low density regions where the magnetic field extends into the solar wind. These structures will be populated with our forward model for density. The structural model is purely geometric and does not make assumptions on the magnetic field or thermodynamic properties of the individual structure. EUV-bandpass images from the EUVI instrument aboard STEREO are used to constrain the cavity morphology for the structural model. The cavity geometry is based on an a ellipse. A user-interactive fitting routine was used to measure the apparent dimensions of the cavity over the course of 8 days. The Gibson et al paper focuses primarily on establishing the 3D morphology of the cavity which

Table 2.1. Forward model streamer properties

Quantity	Parameter	Value
Streamer central colatitude	θ_o	$45.55° \pm 0.29$
Streamer central Carrington longitude	ϕ_o	$-30.33° \pm 2.47$
Angle of streamer axis to equator	m	$8.95° \pm 0.47$
***Tilt of streamer height axis vs. radial**	α	$28°$
***Streamer half-width at photosphere**	S_{width}	$19°$
***Streamer half-length at photosphere**	S_{length}	$50°$
***Streamer current sheet height**	R_{cs}	$1.8R_\odot$
***Streamer current sheet half-width**	CS_{width}	$2.5°$

Note. — *model parameters modified from Gibson et al (2010).

is essentially insensitive to streamer morphological properties, and in this work we have refined the streamer width, current sheet (CS) height, CS width, and streamer nonradiality angle. The streamer geometry is determined via synoptic observations with the MLSO MK4 coronagraph. In determining the streamer width and angle, radial profiles proved to be extremely useful. The polarization brightness of the streamer is well fit with a power law from 1.17-1.50 $R_\odot$. Above 1.5 $R_\odot$ the power law slope steepens between 1.50 and 2.5 $R_\odot$. A power law density profile cannot capture this "elbow" in the polarization brightness profile. This elbow is caused by the transition from streamer to coronal hole. Based on the location and slope of this transition as well as visual inspection of synthetic polarization brightness images identical to Figure 2.3b, we constrained the streamer width, height, and nonradiality angle. The streamer parameters are shown in Table 2.1. A more detailed explanation of errors in this process is presented in section 2.5.1.

2.3.2 Forward Model

Line ratio diagnostics are often applied to active region loops, where the structure is localized. The cavity is, however, a longitudinally extended structure. Along the line of sight, the strongest emission (barring major temperature fluctuations) occurs at the densest point, which is the plane of

the sky in axisymmetry. However, the line-of-sight integration also contains contributions from the higher altitude, lower density plasma outside the plane of the sky. If we are diagnosing a localized feature (an active region loop, for example) we can subtract out a background emission based on the surrounding intensity at the same plane of sky radial height to isolate emission from the localized feature. In the cavity, the projection problem is more severe. Cavities are only visible when they have an extended segment along the line of sight. Cavities are embedded within streamers, which are higher density. To diagnose the cavity, we have taken a forward modeling approach which compensates for projection effects.

The quantity we are interested in is the radial density profile of cavity. We also derive the radial density profile of the streamer. The basic framework of this forward diagnostic technique is laid out as follows: derive the 3D structural layout of the corona and then synthesize EUV emission from the model corona which can be compared with Hinode/EIS observations and polarization brightness which can be compared to MLSO MK4.

Gibson et al. [2010] described the 3D morphological model. Into this structural model we apply a power law radial density profile to the three structures:

$$N = (a\ r^{-b} + c\ r^{-d} + e\ r^{-f}) \times 10^{8}\mathrm{cm}^{-3} \tag{2.1}$$

A 6-parameter power law has been used by previous studies of streamer densities [Gibson et al., 1999]. For coronal hole, streamer, and cavity we have a total of 18 parameters. We do not have spectroscopic data which is coronal-hole specific so we have set the profile parameters equal to the values in Guhathakurta et al. [1999]. The coronal hole emission does not contribute to the EUV integral by more than 6% so this substitution does not have a major effect.

EUV emission is dependent on both density and temperature. A temperature model must be included to synthesize emission. We test two different models of temperature: uniform isothermal streamer and cavity, and isothermal streamer and cavity with different temperatures.

The equation for optically thin emission is presented in section 1.4.1. We simplify the Equa-

tion 1.15 by using the level population

$$I_{ji} = \frac{\Delta E \ A_{ji}}{4\pi} \int n_j \ dh \tag{2.2}$$

where n_j is the number density of the upper emitting level j for a given ionization state, ΔE is the change in energy between levels j and i, and A_{ji} is the frequency for spontaneous emission between levels j and i. The level populations are determined by the collisional excitation rate coefficients, and the spontaneous radiative transition probabilities. For our isothermal model, we have assumed the populations can be written as

$$\mathcal{N}_0 = n_j(N, T = 1.55 \text{ MK}) \tag{2.3}$$

where $\mathcal{N}_0$ is the population of ions in upper emitting level j in units of cm^{-3}. This function has been calculated using the CHIANTI atomic database [Dere et al., 1997] with elemental abundances of Feldman [1992] and ionization equilibrium from Mazzotta et al. [1998]. Similarly a population function for temperature is generated,

$$\mathcal{N}_T = n_j(T, N = 10^9 \text{ cm}^{-3}) \tag{2.4}$$

In the modeling runs where temperature is allowed to vary, the level populations are calculated as

$$n_j(N, T) = \mathcal{N}_0(N) * \frac{\mathcal{N}_T(T)}{\mathcal{N}_T(T = 1.55 \text{ MK})} \tag{2.5}$$

By separating the density and temperature dependence of line emission, forward modeling the Fe XII line ratio becomes tractable as a minimization problem. This solution is not a comprehensive approach for synthesizing all EUV emission. Our forward model looks solely at a singular ionization state so the ionization equilibrium temperature dependency cancels in the ratio. We also allow only a narrow range of coronal temperatures to be implemented in the model, forcing a regime where density effects dominate emission.

The polarization brightness does not depend on the temperature because it is produced by a scattering process. Synthesizing MK4 data is done using the analytic equations provided by Billings [1966]. The polarization brightness contributions at each element along the line of sight is determined by its density and its location relative to the plane of the sky. These contributions are integrated. Once both the line ratio and polarization brightness have been synthesized, a χ^2 goodness-of-fit statistic is used to compare the synthetic models to the EIS and MK4 data based on the observational errors. We are interested in finding the density model which best captures the MK4 and EIS datasets. To find the best fit, we use a genetic-algorithm minimization routine.

We use the PIKAIA genetic algorithm to find the best-fit density models through a directed search of parameter space. Genetic algorithms function on the basis of "survival of the fittest". Model parameters are normalized into a set of 4-digit chromosomes. Sets of parameters are "bred" which splices chromosomes, and thereby varying model parameters are as function of iteration. The χ^2-statistic is used to define which models are most likely to breed and survive. PIKAIA is described in full detail in Charbonneau [1995]. We have taken care to supply the genetic algorithm with natural selection parameters which maximize the parameter space covered while still favoring low χ^2 models: fully generational replacement, high mutation rate, low breeding differential. These minimization parameters have been adapted from Gibson and Charbonneau [1998]. We have developed error bars based on the distribution of solutions within χ^2 space. The simulation set consists of 30000 model sets (for each of the two temperature models) of which approximately 1500 solutions fit within the 90% confidence interval (based on the degrees of freedom of the model).

2.3.3 Data Selection

In the interest of computational resources, we have chosen specific regions in the datasets which we use to quantify the goodness of fit between model and data. The EIS dataset is limited in its field of view and is furthermore affected by satellite eclipse data gaps. The MK4 white-light coronagraph observes the entire corona from 1.15-2.5 $R_\odot$. The final regions selected for quantitative comparison are displayed in Figure 2.2. In the EIS dataset, 76 measurements are

used: 48 in the cavity, 28 in the streamer. In the MK4 dataset, 323 measurements are used: 160 in the cavity, 163 in the streamer. The weighting of each point is inversely proportional to the square of the observational error. The errors are primarily Poisson-noise in both the EIS and MK4 dataset. Appendix C discusses the method for deriving errors on spectral line profiles. MK4 errors where constructed based on a discussion with the observer and measurements from Elmore et al. [2003]. The relative error on the MK4 data is larger than that of the EIS data so the fit is not overly sensitive to the MK4 data. The location of the selected EIS regions are necessitated by the pointing of the telescope. The MK4 regions have been selected to extract data from the central cavity and the streamer radially above the EIS data. The relative locations of the selected analysis regions minimizes the effect of the morphology errors on the derived central cavity and streamer profiles. The boundary between streamer and coronal hole is smoothly varying such that there is not a density jump across a structural boundary. This density transition is gaussian in latitude so that by selecting regions of constant latitude in both EIS and MK4 data there is no latitudinal variation.

2.4 Results

2.4.1 Best Fit Isothermal Model

For the isothermal temperature model, both the streamer and cavity temperature are set to 1.55 MK. The data used for quantitative analysis and the synthesized best fit model calculations are plotted in Figure 2.4. The structural identity of each point is based on the morphological model. The corona is optically thin so in reality most lines of sight contain both cavity and streamer plasma.

The cavity in the EIS dataset shows a clear depletion in Fe XII line ratio. The depletion is approximately constant with height at 20%. The best-fit model plotted here has a reduced χ^2 of 3.6 for the EIS data. A significant fraction of this total χ^2 comes from specific outlier points in the EIS dataset mainly in the cavity below 1.06 $R_\odot$ and above 1.16 $R_\odot$. For reference Table 2.3

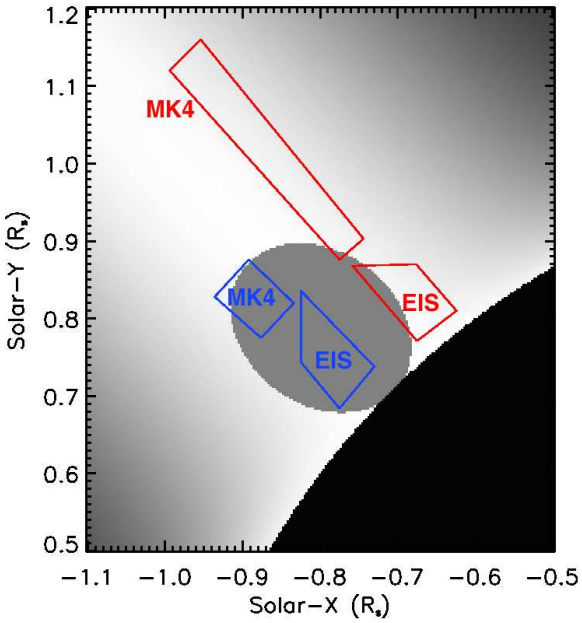

Figure 2.2 The morphological model in the plane of the sky on at 18:00UT 09-Aug-2007. The regions of data extracted for quantitative analysis are shown for both EIS and MK4. Cavity regions are blue. Streamer regions are red.The grayscale image shows the plane of sky density given a constant depletion cavity and a streamer without a radial density falloff.

contains various χ^2 measurements from different dataset regions.

The total reduced χ^2 is 0.8 for the polarization brightness data in Figure 2.4. This low number reflects the large error bars on the MK4 observations. Absolute calibration of white-light coronagraphs is difficult due the level of internal scattered light. This problem is exacerbated by the fact that only a single pixel scans each radial height, making interpixel calibration an issue as well. Above 1.20 $R_{\odot}$, the cavity (at a colatitude of 46°) is brighter than the streamer (at colatitude of 42°) in both the data and the model. In the model, this results from the shape of the streamer. The streamer density profile is gaussian in latitude. The cavity is centered on this gaussian while the analyzed streamer region is offset. Lines of sight in the upper cavity encounter less cavity material so the upper cavity region in Figure 2.2 will appear brighter than the upper streamer region due to the gaussian density variation in latitude. Figure 2.5 displays the complete EIS line ratio image as well as the model calculation. The solar limb and the plane-of-sky boundary of the cavity based on the morphological model are plotted as white lines. The overall structure of the EIS dataset is radially stratified layers. The observed cavity is an indentation in this stratification that is larger than the plane of sky morphological cavity boundary. This results from the neutral line angle of the cavity which smears out the apparent cavity to a wider latitude range. There are significant model-data discrepancies near the limb. The near-limb data points are not used in the quantitative analysis because of prominence and transition region contributions. Plasma from this height does not enter the line of sight for any of the data used for quantitative analysis. Statistically, the best-fit model does worst off the southern edge of the cavity and at the limb. As previously documented, equatorial structure is more projection-sensitive than that on the poleward side [Gibson et al., 2006], and for this reason the equatorward streamer points are not used for the quantitative analysis. The cavity and streamer vicinity in polarization brightness are plotted in Figure 2.3. The location and slope of the red, blue, and green brightness contours provide some perspective on the quality of the streamer fit. There is approximately equal spacing of the contours in both the model and data. Within the colatitude range of 33-47°, the slopes are also similar. However, model and data differ at the far poleward side of the streamer as well as the streamer core.

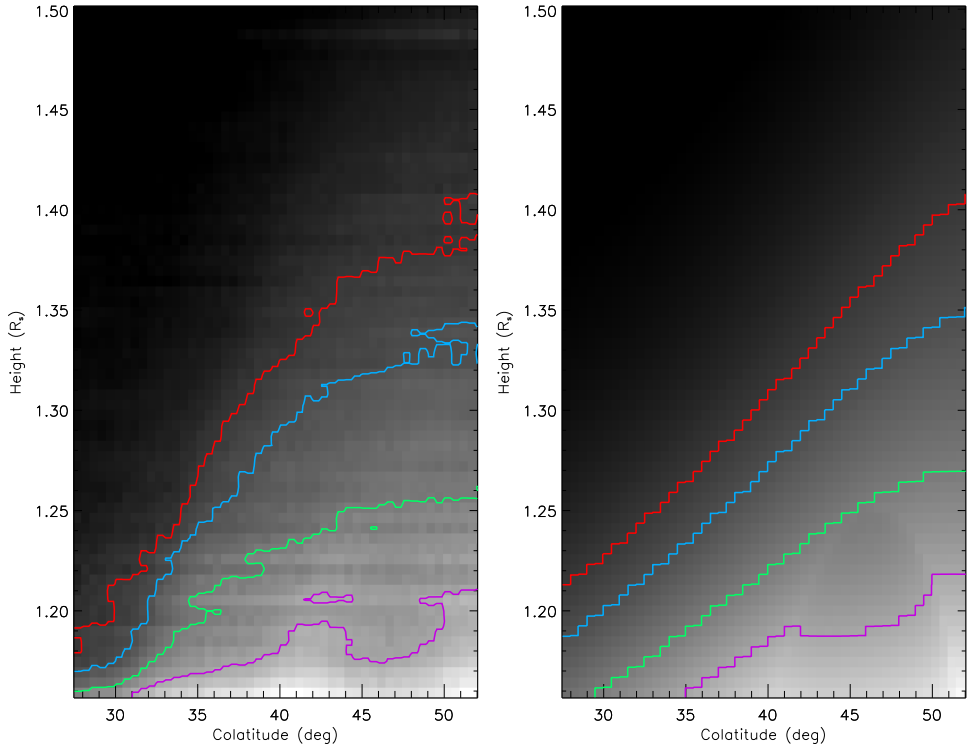

Figure 2.3 MK4 polarization brightness and the synthetic polarization brightness based on the best fit isothermal density model. The contours from lowest to highest height are 1.9, 1.4, 1.0, and $0.7 \times 10^{-7} B_{photo}$ (which is Sun disk center brightness).

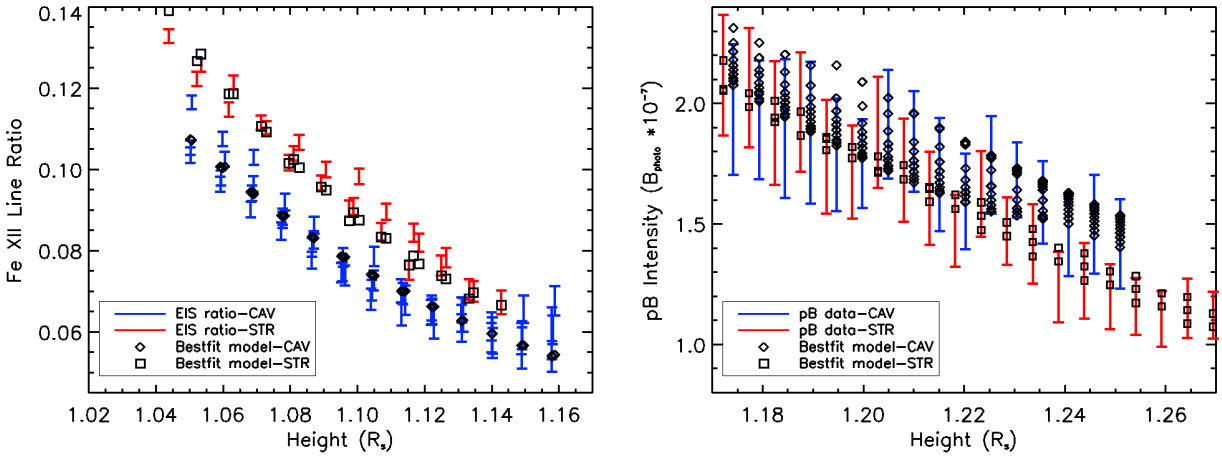

Figure 2.4 Observed data with error bars compared to the isothermal best fit density model. Hinode/EIS 186.8A/195.1A Fe XII line ratio (left). MLSO MK4 polarization brightness (right). Blue bars mark cavity data. Red bars mark streamer data. Diamond symbols are model calculations of the cavity and the squares are streamer.

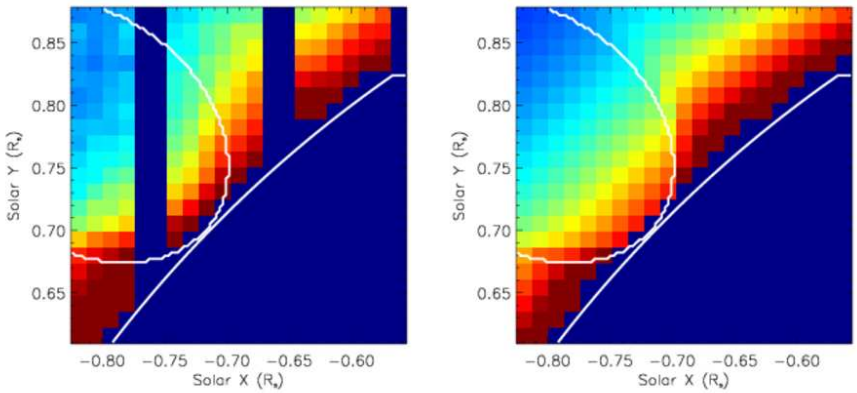

Figure 2.5 EIS line ratio image and synthetic line ratio based on the best fit isothermal density model. The plane of sky model cavity and the solar limb are marked by white lines. Both images use the same color table where blue is 0.04 and red is 0.16 in line ratio.

The observed MK4 streamer is more blunted and has a wider crown than the model streamer. This particular geometric variation cannot be accounted for in the streamer model. Similarly, the slope of poleward edge of the streamer is not well captured by the linearity of the model. Statistically, the model regions which are least accurate are the poleward coronal hole and the equatorial side of the streamer. The χ^2 for the coronal hole is large due the fact that we have not fit the coronal hole due to lack of spectroscopic data. As was discussed for Figure 2.4, the lower cavity is not as strongly contrasted in the model as in the data. This is illustrated by the purple contour.

2.4.2 Derived Densities

Neither EIS line ratio nor polarization brightness uniquely probe the radial density profile of the corona. These observables are convoluted by projection effects. In forward modeling, we synthesize analog observables to test the quality of a given density model. Our derived results are the radial density profiles in the cavity and the streamer. Figure 2.6 shows sets of notable density models. Because every line of sight is a mixture of both streamer and cavity, the derived profiles are not independent of each other. Thus, each cavity and streamer model must be regarded as a set. The best-fit uniform isothermal models are the solid lines. We define depletion (of the cavity)

as

$$\frac{N_{STR} - N_{CAV}}{N_{STR}}$$

The depletion for the best-fit model is 30% and is approximately constant with height. A reduced χ^2 of 1.3 is calculated for this model. This is a low χ^2 which indicates that our model is accurately reproducing the data. Looking at Table 2.3, we must acknowledge that there is discrepancy within the model. Our model fits the MK4 data much better than the EIS data (reduced χ^2 of 0.8 and 4.3). There are two reasons for this. The MK4 data has larger errors relative to the data. The large error bars are largely determined by the amount of scattered light within the telescope. Due to the age and condition of the telescope (the amount of dust on the lens has been shown to cause variability), this quantity is impossible to determine post-observation, and the error bars are large in accord with the recommendation of the observers. The χ^2 value for the EIS data and best-fit model appears to be artificially high. The EIS line ratios vary by 50% between the top and bottom of the cavity. This large scale trend is captured well by the model as is indicated in Figure 2.4. However, there is substantial variation as well at each particular height in the data. This variation occurs from the spatial dimension which is not plotted in Figure 2.4, colatitude. This spatial variation is larger than the photometric error bars for the data. Our smoothly varying spatial model does not capture the small-scale structure which causes these variations. The intention of this diagnostic is not to measure the small-scale structure but to assess the average cavity density. Based on this principle, we find that the model suitably captures the data, which allows us to proceed with an error analysis.

Given the 399 data points and the 12 model parameters and a minimum χ^2 of 520, models with a χ^2 value less than 940 are within the 90% confidence interval. Based on these values, we have extracted approximately 1500 models from the model sets which fall within that confidence interval. These models correspond to a range of densities at any given height, and this range will be used to present error bars in the derived density.

The dashed lines represent the solution set with the maximum cavity density at the cavity

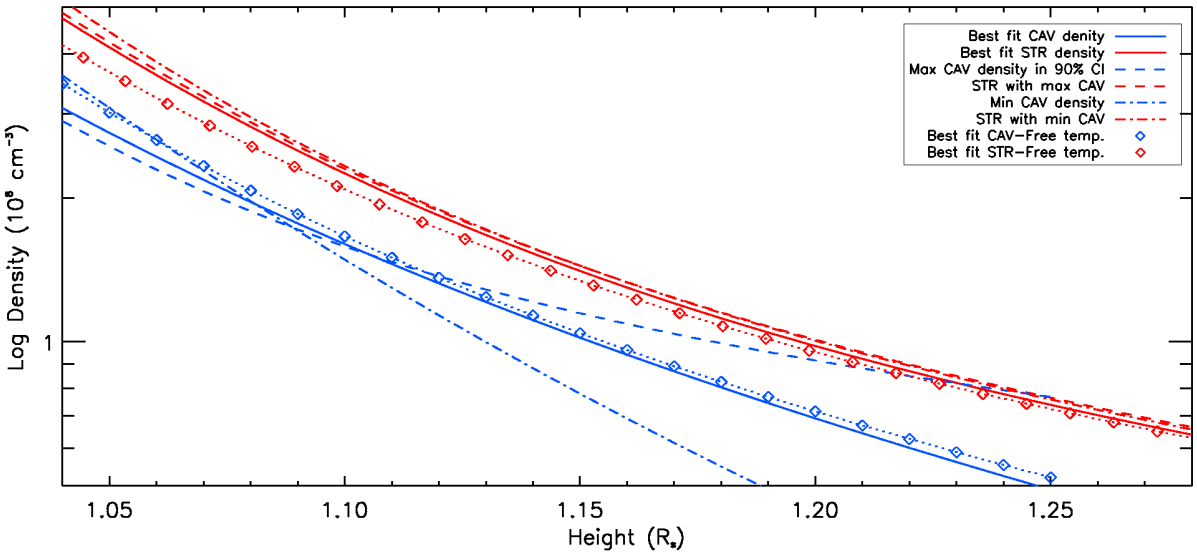

Figure 2.6 Density models derived for the χ^2 minimization PIKAIA model set. The best fit isothermal model has a reduced χ^2 of 1.3 while the free temperature best fit has a reduced χ^2 of 1.1 using 399 data points. The minimum-maximum density cavity models represent the extremes of models within the confidence interval. The model parameters which provide these densities are given in Table 2.2.

top (r=1.25 $R_\odot$) within the confidence interval. At the cavity top, this cavity is 60% denser than the best fit model. The associated streamer model is 5% less dense than the best fit at 1.25 $R_\odot$. The depletion for this model set decreases with height.

There are several important points we consider by comparing the dense cavity model to the best fit model. The streamer is much more tightly constrained than the cavity. This is related to the sampling of the cavity plasma. Our structural cavity model has an elliptical cavity embedded in a streamer. The variation of ellipse height with longitude is gaussian. Near the solar limb, a large percentage of the EUV radiation is emitted from the cavity. Lines of sight which cross the plane of the sky at higher heights contain a smaller percentage of cavity plasma. At the crest of the cavity, only a sliver of cavity encounters the line of sight and a majority of the emission is from the streamer. This geometric property fundamentally limits the degree to which we can diagnose the upper cavity. The analysis of the lower streamer does not encounter this problem, but if we extended our modeling to 2 or 3 $R_\odot$ the streamer also becomes less tightly defined as the coronal hole becomes a significant contributor.

Figure 2.6 shows that the density is most tightly constrained at 1.08 $R_\odot$. The EIS data at 1.05 $R_\odot$ has the highest signal to noise ratio. However, this plasma is not sampled by many lines of sight. The height of 1.08 $R_\odot$ represents the balance between the quality of data and amount of data. The errors are tighter for lower-height lines of sight, but fewer lines of sight encounter plasma at that height. The dashed-dot lines represent the model calculation with the minimum cavity density at the cavity top that was within the confidence interval. This model cavity is 45% less dense than the best-fit model. The depletion of this model increases with height.

Table 2.2 displays the model parameters that produce the profiles plotted in Figure 2.6. Fuller et al. [2008] derived a exponential cavity density profile. Our profile is notably steeper in the lower cavity, which was not diagnosed by Fuller et al. [2008] because the white-light data being analyzed did not extend to low heights. This steepness increase is consistent with the Gibson et al. [1999] results, in which SOHO/CDS data from low heights were analyzed. By fitting an exponential to our best-fit cavity profile at MK4 heights, we find a scale height of 0.14 $R_\odot$, which is consistent

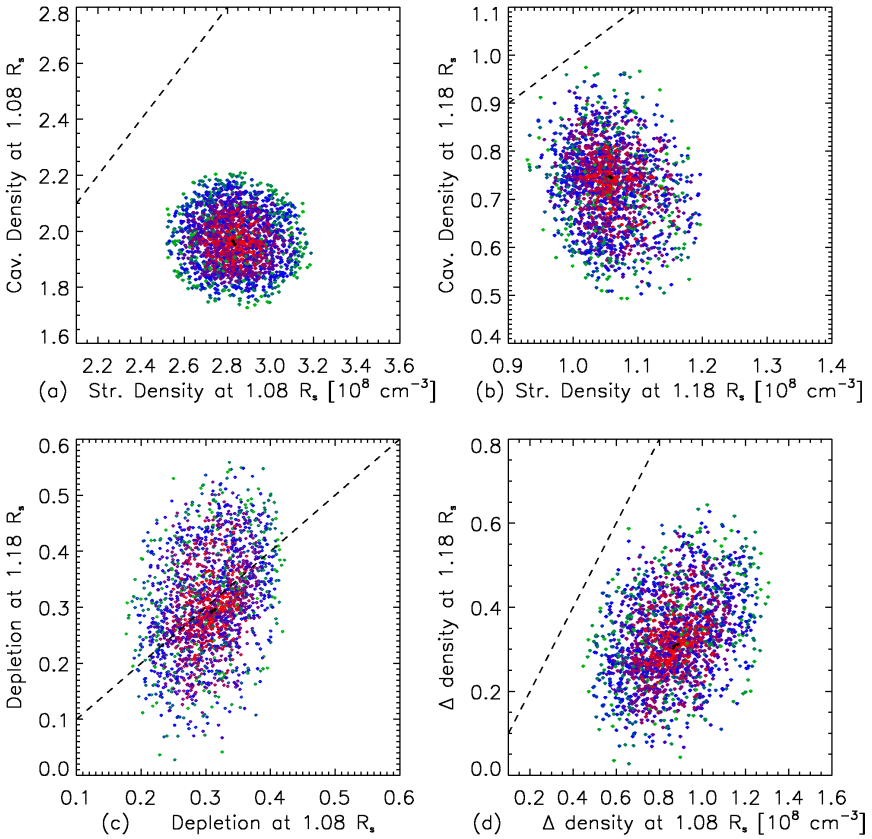

Figure 2.7 Scatter plots of the isothermal model sets within the error bars. Color represents individual model χ^2. Red are the best models with χ^2 less than 1.5, blue have χ^2 less than 2, green are $\chi^2 = 2.4$ or below. (a) Density at 1.08 $R_\odot$ where the fit is most tightly constrained. The dashed line marks models with equal cavity and streamer densities. (b) Density at 1.18 $R_\odot$ where the models are constrained by both EIS and MK4. (c) Depletion at the two heights where the dashed line marks the division between models in which depletion increases or decrease with height. (d) Absolute density difference at two heights. The dashed line marks where the density jump is constant with height.

Table 2.2. Density model parameters

Model	a_{str}	b_{str}	c_{str}	d_{str}	e_{str}	f_{str}	a_{cav}	b_{cav}	c_{cav}	d_{cav}	e_{cav}	f_{cav}
best fit[1]	1.27	22.8	5.97	16.0	1.57	3.87	0.91	23.6	2.33	16.6	1.96	6.81
max cav[1]	1.50	23.8	5.99	16.3	1.69	3.94	2.46	24.3	1.26	16.5	1.45	3.12
min cav[1]	5.57	22.3	3.07	13.4	1.71	4.10	3.94	20.7	2.03	15.2	1.01	8.33
best fit[2]	2.54	18.8	3.35	14.4	1.51	3.81	2.19	26.9	2.66	16.6	1.64	5.81

Note. — [1] isothermal model of 1.55 MK. [2] free temperature model: cavity at 1.9 MK, streamer at 1.1 MK. All streamer parameters are defined relative to the r_{piv} radial coordinate which is tilted by the streamer angle as discussed in Gibson et al. [2010].

with Fuller et al. [2008] given our stated errors.

The models plotted in Figure 2.6 illustrate the extremes of the set of model calculations. The errors on the derived density are based on the entire distribution of solution sets within the stated confidence interval. Figure 2.7 plots some key quantities from the 1500 isothermal model calculations that lie within the confidence interval. Figure 2.7a and 2.7b show the range of densities at two different heights. The height of 1.08 $R_\odot$ is shown in Figure 2.7a. The distribution of densities is elliptical in regards to χ^2. The axes of the ellipse are perpendicular to the plot axes implying no correlation between the streamer density and the cavity density. This property is due to the fact that the lines of sight in this region of the datasets are predominately composed of streamer or cavity without much convolution of the two. The streamer densities are centered on $2.8 \times 10^8 \mathrm{cm}^{-3} \pm 10\%$. The cavity densities are centered on $1.9 \times 10^8 \mathrm{cm}^{-3} \pm 13\%$.

At 1.18 $R_\odot$, the distribution is less regular. The ellipse has a slightly negative tilt to the vertical axis implying an anticorrelation in model parameter space between the streamer density and cavity density at this height. In the upper corona, each line of sight involves contribution from both cavity and streamer. Given a polarization brightness, if the streamer is less dense, the cavity must be more dense to compensate. This relationship is not linear, however, because the radial density derivative also plays a role. The range of streamer densities has increased to $1.06 \times 10^8 \mathrm{cm}^{-3} \pm 14\%$. The range of cavity densities is $0.75 \times 10^8 \mathrm{cm}^{-3} \pm 36\%$. All of the models sit below the dashed line which marks the cavity-streamer density ratio of unity.

Figure 2.7c shows the relative depletion at the two heights. The dashed line marks the solutions with a constant depletion with height. The best fit solutions lie close to this line although there is a wider spread at the higher height. There is a positive correlation between the depletion at 1.08 $R_\odot$ and the depletion at 1.18 $R_\odot$. Given our error bars, it is impossible to determine whether the cavity depletion is increasing or decreasing with height.

Figure 2.7d shows the change in density in absolute difference. This quantity is arguably the most physically significant as it uniquely determines the gas pressure discontinuity across the cavity boundary in an isothermal approximation. The change in density decreases with height which is

consistent with the radial falloff of density. There is a positive correlation between the ΔN at $1.08R_{\odot}$ and 1.18 $R_{\odot}$.

Figure 2.7 illustrates that the derived density is regularly distributed as a function of χ^2. Based on the distribution, errors bars on the density as function of height have been defined at specific heights. Despite this overall error measure, individual errors on the parameters listed in Table 2.2 have not been determined. There are strong correlations between the model parameters in Equation 2.1, and thus marginal errors on the parameters themselves are not useful.

Table 2.3 lists the χ^2 values for several locations besides the subregions that are explicitly used for the minimization. Our fit is consistent with the data which were not used. The near-limb data in EIS and the poleward streamer-coronal hole boundary are the least accurate regions of the best fit isothermal model.

2.4.3 Temperature Effects

The corona is not accurately described by an isothermal approximation. DEM analysis and the broad range of spectral lines from UV to hard X-ray implies that temperature gradients are ubiquitous in the corona [Rosner et al., 1978, Craig et al., 1978]. However, in the interest of model simplicity the isothermal approximation is a common one in coronal physics. Our modeling technique makes use of both EUV emission lines and white-light scattering data. White-light scattering is solely dependent on free electron density. The EUV observable we have been forward modeling in this work is only weakly temperature dependent. However, the excited electron states for the 195.1A and 186.8A lines are not the same so there is a temperature dependence on the population of these levels and the emissivity of the lines. The treatment of temperature-dependent emissivity is discussed in section 2.3.1.

In this work, we do not attempt to determine the plasma temperature inside the cavity and streamer. This problem is ill-posed with our chosen datasets. In order to test the robustness of our density result to variations in temperature, we have conducted a model minimization which allows the isothermal temperature of cavity and the isothermal temperature of streamer to vary as

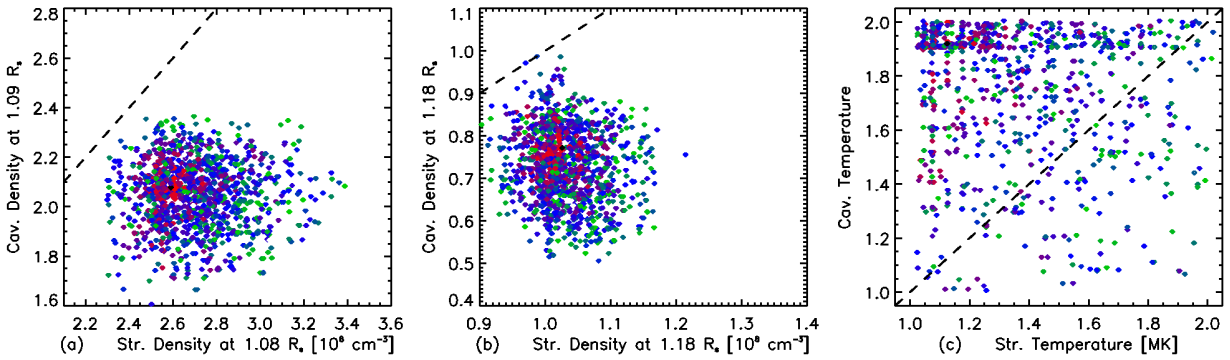

Figure 2.8 Scatter plots of the free-temperature model sets within the error bars. Plots (a) and (b) are identical to Figure 2.7a and 2.7b respectively, except the temperature has been allowed to vary. Distribution of temperatures for model sets (c).

separate parameters. Figure 2.8 plots the model sets where temperature has been allowed to vary. Separate isothermal temperatures are set in the model cavity and streamer. These temperatures are varied as model parameters by the genetic algorithm. Figure 2.8a shows the range of densities at $1.08R_{\odot}$ within the error bars. This figure is comparable to Figure 2.7a which illustrated the isothermal model sets. The best-fit temperature-varying model has a lower density in the rim and a higher density in the cavity than the best fit isothermal model. Overall the distibution at $1.08R_{\odot}$ has also shifted in this direction. The shape of the distribution is less elliptical than the isothermal model set. This results from the additional degrees of the freedom in temperature which can have differing effects on the 186.8A and 195.1A lines. The PIKAIA model distribution is affected by the poorly constrained temperature. We have chosen the Fe XII line ratio because it is only weakly temperature dependent. Therefore, temperature is very weakly constrained by the forward model. Figure 2.8c illustrates the struggles that PIKAIA has with deriving a temperature. The lowest χ^2 models (red points) are clustered near 1.4-2 MK cavity and a 1-1.2 MK streamer. The clustering is a consequence of the selectivity of the genetic algorithm.

The minimum χ^2 for the free temperature models in only a 18% reduction compared to the isothermal model. The purple points in Figure 2.8c represent models with reduced χ^2 of 1.3 approximately. These points span the entire temperature domain. The best fit temperature

Table 2.3. Regionalized χ^2 for the best-fit isothermal model

	Total sub	EIS sub	MK4 sub	EIS all	MK4 all	Cav low	Cav hi	Str low	Str hi
Pts	399	76	323	139	147117	71	13875	33	80865
χ^2	1.34	4.26	0.80	5.00	3.62	3.79	0.51	4.1	0.60

Note. — "Sub" are regions used for minimization. "All" are all regions with viable data. "Low" are regions below $1.15R_\odot$, "Hi" are regions above $1.15R_\odot$

models suggest a cool streamer and a hot cavity. This, however, is not statistically significant, as a minor increase in χ^2 provides solutions which fill the temperature domain. Using the Fe XII 186.8A/195.1A line ratio and the MK4 white light data, we cannot constrain the temperature, and the set of model solutions shows little structure in temperature as a result.

2.5 Discussion

2.5.1 Errors

In searching for a density model which best fits the MK4 and EIS datasets, we use observational errors to assign weights to each observational measurement. The distribution of χ^2 values in parameter space allow us to assign error bars in density which are based on the observational errors. In this section, we discuss the errors present elsewhere in the model and the affect they have on our derived quantities.

In this work, we have not allowed the morphological parameters to vary as free model parameters. The morphology has previously been determined with both stereoscopic and time-dependent analysis [Gibson et al., 2010] . We have not quantitatively incorporated structural errors into the quoted density errors. However, we have tested the robustness of our best fit isothermal model to modification of the following structural parameters: streamer width, streamer height, streamer angle, streamer length, cavity width, and cavity height. In the Gibson et al. analysis, the cavity height and width are the most tightly constrained parameters. In this analysis, we find that these

parameters have little effect on the solution. The cavity parameters most strongly affect the upper cavity density. This quantity is inherently the most error prone. A line of sight at central cavity colatitude (47°) with a plane of sky height of 1.25 $R_\odot$ contains only 4% of its line emission from the cavity structure. Variations exceeding 30° in cavity length are necessary to push the cavity top density beyond the errors already determined by the isothermal model sets.

In this work, we establish the streamer morphology which was not explicitly fit in Gibson et al. [2010]. We have chosen regions which are the least sensitive to morphological discrepancies. By choosing a MK4 streamer region near streamer center, we are assured that line of sight encounters a minimum of 90% streamer scattering as opposed to coronal hole. Of these parameters, the streamer width most strongly affects the measured streamer density profile. Variations in streamer width of 10° at the photosphere and 5° at the streamer cusp are necessary to affect the derived density beyond the stated error bars below 1.5 $R_\odot$. Variations at that level are impossible to reconcile with the streamer shape seen in Figure 2.3a.

Another likely source of error in this analysis is the incomplete nature of atomic data. In calculating the temperature and density sensitivity of the Fe XII lines, level populations are solved for based primarily on electron collisional excitation and radiation de-excitation. The temperature dependence of collisional strengths have largely been measured using numerical models. The Fe XII ion is of particular interest in solar physics and has been the target for detailed studies [Storey et al., 2005]. However, laboratory measurements of these specific plasma processes are lacking. Our analysis has benefited by the inclusion of two separate datasets which rely on separate physical processes. The degree to which model solutions match both EUV spectra and electron scattering data is reassuring, especially considering polarization brightness can be determined wholly analytically.

Our treatment of coronal temperatures is meant to test the robustness of our density measurement to temperature perturbation. We use a simplified model in which we assign isothermal temperatures to the streamer and cavity. Kucera et al. [2012] focus on temperature diagnostics inside the cavity based on EUV intensities in a much more comprehensive approach. We have shown that our density results are not strongly affected by temperature variations that are within

the likely regime for the lower corona.

2.5.2 Conclusions

The goal of this research was to constrain the density of a coronal cavity and that of the surrounding streamer using a forward modeling approach. We have used Hinode/EIS and MK4 data as observables to which we compare the synthetic forward model analogs. Using the PIKAIA genetic algorithm to minimize the χ^2 statistic, we find a best-fit density models for the streamer and the cavity. For a density model, a 6-parameter power law is used. Two temperature models were used: uniform isothermal corona at 1.55 MK and two temperature isothermal streamer and cavity.

We have measured a cavity density in the range of 1.05 $R_\odot$ to 1.25 $R_\odot$. The errors on the cavity measurement vary with height and are smallest at 1.08 $R_\odot$. The best-fit isothermal model determines a density of 1.95×10^8 cm^{-3} of the cavity and 2.85×10^8cm^{-3} in the streamer at that height. In the uniform isothermal approximation, the errors bars are $\pm 0.25 \times 10^8$cm^{-3} in the cavity. Allowing temperature to vary increases the density range to $\pm 0.4 \times 10^8$ cm^{-3}.

The range of possible densities changes with height. The error on the streamer densities decrease with height. Above 1.15 $R_\odot$ the error is always less than 15%. This does not hold true for the cavity. The cavity errors increase with height. This is primarily due to the proportion of cavity along the line of sight. With the two-temperature isothermal approximation, we find that the cavity is depleted compared to the streamer up to a minimum height of 1.20 $R_\odot$. Smaller observational errors would allow us to better constrain the density in the upper cavity, but the geometric properties of the system will always force the largest relative errors in this region.

This work is the first time that cavity densities have been measured below 1.10 $R_\odot$. It is also the first time that a multi-instrument approach has been taken in cavity diagnostics. Given the different physical processes for white light scattering and the EUV line emission, the coherency of density results between datasets validates our technique.

These observational diagnostics are proposed in order to understand the force and energy

balance of the prominence, cavity, and streamer interfaces. The force balance in the low-β corona is dominated by the magnetic field. Although gas pressure plays a role across the cavity-streamer boundary, we need coronal magnetic field measurements to analyze this region. Coronal spectropolarimetry holds promise, although these results must account for line-of-sight projection effects as well [Dove et al., 2011].

An additional complication to this work is the recent observations of ubiquitous flows in cavities [Schmit et al., 2009, Wang and Stenborg, 2010]. Time-independent diagnostics of the static cavity structures must be reconciled with the time-dependent flows and emission variations. This is the area of cavity-prominence research where the Solar Dynamics Observatory will have the largest impact, which will be discussed in Chapter 3.

Chapter 3

Diagnosing the Dynamic Cavity

Prominences are dynamic structures. The finest resolved structure in prominences varies on the order of minutes, and these variations are believed to be a result of motions of the plasma as well thermodynamics changes in the plasma. There is a dichotomy in prominences in that they are dynamic on short timescales but maintain a long-term stability.

In this chapter, we observe the dynamic structure of the cavity in both flows and emission variability. Using the SDO/AIA dataset, we find evidence for ubiquitous correlated prominence-cavity dynamics. We extract and statistically analyze these events to develop a set of constraints on the energetic process which creates the emission variability.

The strongest coronal emission variations that occur in the cavity are brightenings in the 171Å bandpass, known as prominence horns. Prominences horns are characterized by 3-hour brightening events which geometrically resemble segments of concave-up coronal loops which extend 10-50 Mm above the prominence. These events project throughout the cavity. They are closely associated with extensions of the prominence and weakly associated with other coronal emission.

In Chapter 4, we use energetic models of coronal loops to identify the physical source of prominence horns. In particular, we will test the idea that the prominence and cavity are linked by a dynamic mass-loading, catastrophic cooling process as suggested by the thermal non-equilibrium model. The layout of this chapter is as follows: Section 1 describes observations of dynamics in prominences, Section 2 describes observations of flows in cavities, Section 3 describes the emission variability of cavities, and Section 4 describes the conclusions of the dynamics analysis.

3.1 Prominence Dynamics

Prominences have long been observed as dynamic phenomena [Rudnick, 1934]. The seminal observations are described in Zirker et al. [1998]. Doppler measurements are used to show that bulk motions in the prominence can be aligned but anti-parallel despite spatial separations a few hundred kilometers (prominence thread widths are on the order ≈ 100 km). This implies a highly coherent magnetic field but with distinctly non-coherent thermodynamic processes. Zirker et al did not find a coronal emission component associated with the prominence dynamics. In addition to thread motions, bubbles are also a dynamic prominence feature [Berger et al., 2011]. Bubbles appear as emission voids and vary between 1 Mm and 50 Mm in size. Bubbles are believed to be low density, magnetically-isolated structures which buoyantly rise through prominence material. The prominence material passively shifts around the bubbles. Both bubbles and thread motions operate on sub-megameter spatial scales, but despite these small scale dynamics, the large scale prominence structure remains intact. Both of these observations highlight the complex interaction of the magnetic field and plasma in the prominence. However, neither observations addresses the role the cavity plays in the dynamics.

3.2 Flows in Cavities

Spectroscopic observations allow us to measure flows in the corona through the Doppler shift of spectral lines. Doppler velocities are derived from the position of emission line centroids as described in Appendix C. We have observed cavities with two spectrographs and found the evidence for coherent large scale flows.

A large cavity was observed using the MLSO Coronal Multichannel Polarimeter (CoMP) on 21-April-2005 [Tomczyk et al., 2008]. CoMP measures the spectral profiles of the Fe XIII 1074.7 nm forbidden line in the near-infrared. CoMP employs a birefringent filter with an instrumental profile that is 0.13 nm at full-width-half-maximum.

Figure 3.1a shows intensity of the 1074.7 nm line observed by CoMP in grayscale. The edge

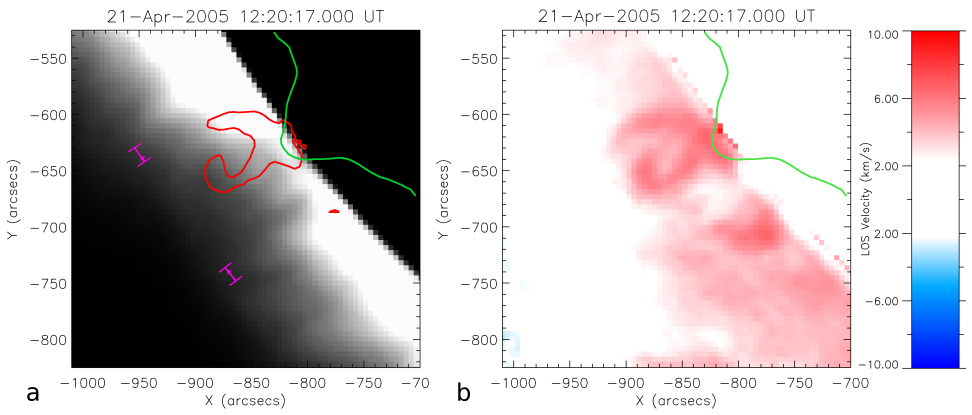

Figure 3.1 (a) Log intensity of cavity as seen in Fe XIII 1074 nm by CoMP. The green contour marks the solar limb and the prominence from SOHO EIT 304Å. The magenta error bars mark the location of the density cavity as determined by MLSO MK4. The red contour marks the velocity structure at +5 km s^{-1}. (b) Line-of-sight velocity from CoMP.

of the coronagraph is visible at 1.05 $R_\odot$ as a black disk. A contour showing the solar limb as seen in SOHO EIT 304Å [Delaboudinière et al., 1995] is shown in green. A prominence protrudes above the limb near (-800", -650"). Prominences emit strongly in He II 304Å. Above the prominence is a low intensity cavity. Although the intensity contrast between the cavity and streamer surrounding the cavity is not strong in this emission line, this cavity was also observed using the MK4 coronagraph at the Mauna Loa Solar Observatory. The magenta bars indicate the edge of the cavity as determined from the MK4 data [based on the method of Gibson et al., 2006]. Figure 3.1b shows the line-of-sight velocity as derived by the Doppler shift of the line centroid in Fe XIII 1074.7 nm. A coherent, nonradial velocity structure of +5 km s^{-1} is contained within the intensity cavity in Figure 3.1a. This velocity structure lies directly above the EIT prominence but on the equatorial edge of the cavity. The MK4 data suggests that the cavity extended a few latitudinal degrees northward on the previous day. This may help explain the northward offset of the velocity structure inside the cavity. The overall height of the velocity structure is 70 Mm.

A second cavity was observed using the Hinode/EIS instrument on 8-November-2008. The specifications of EIS were described in section 2.2.2. Figure 3.2a shows the intensity of the Fe XII 195Å line as seen by EIS. This observation uses the 1" slit with 151 raster steps and 100 s

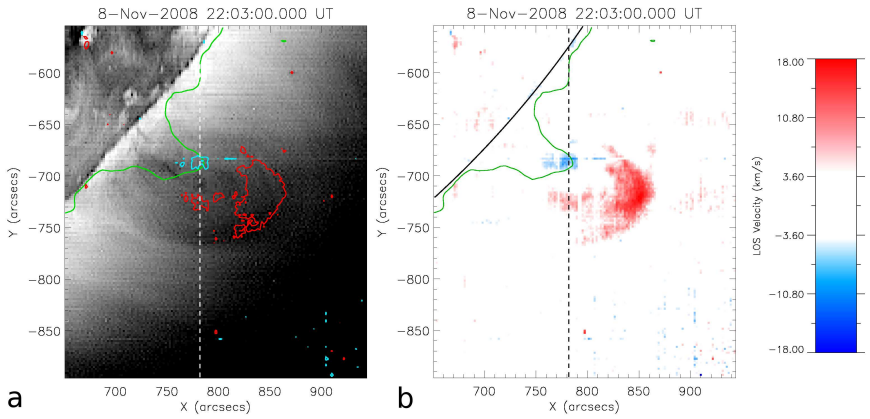

Figure 3.2 (a) Log intensity in EIS Fe XII 195Å. The green contour marks the edge of prominence from SOHO/EIT 304Å. The blue and red contours show ±7 km s^{-1} line of sight velocity. (b) Line-of-sight velocity in Fe XII 195Å.

exposures. The data have been binned 3 x 6 pixels to increase signal-to-noise. The upper extent of the prominence, shown by the green contour, is taken from EIT 304Å data. Figure 3.2b shows the derived line-of-sight velocities. Two coherent regions of measurable velocity are present. A lower region near the prominence shows a line-of-sight velocity of -8 km s^{-1}. This region appears to be located at the upper edge of the prominence, but Fe XII 195Å is a coronal line in which prominences typically do not appear in emission. Located 60" above the blue-shifted region, there is a large-scale red-shifted region with velocity near +8 km s^{-1}. This red region roughly coincides with the top of the cavity, and it overlies the most depleted emission of the structure. The dashed line in Figure 3.2a indicates a slit position where we observed both blue- and red-shifted flows.

The EIS spectrometer does not have an absolute wavelength calibration. There are errors on velocities measurements which are associated with removing time-dependent variations in spectral profiles. In this measurement, we estimate the velocity error at 3 km s^{-1}. Appendix C elaborates on the details of spectral profile errors.

3.3 Emission Variability in Cavities

In section 3.1, we have shown that flows occur within cavities. The source of these flows was not determined, but the direct conclusion is that cavities must be regarded as a structure with internal dynamics, analogous to the prominence.

To extend this work, we have observed cavities in the SDO/AIA dataset [Lemen et al., 2012]. Although the AIA dataset lacks spectral information to derive Doppler flows, it makes use of high resolution, high cadence bandpass imagers which span a broad range of temperature sensitivities. With this dataset, we can observe the changes in emission which are indicative of changes in the thermodynamics properties of the prominence-cavity plasma. Towards this aim, we are interested in one particularly relevant paradigm: is a mass exchange responsible for moving plasma from the under-dense cavity into the over-dense prominence?

3.3.1 SDO/AIA dataset

We use the SDO/AIA dataset to observe dynamics in prominence-cavity system in the EUV. SDO/AIA is composed of 4 Schmidt-Cassegrain telescopes which use multi-coated optics to selectively observe specific bandpasses in the UV and EUV. These telescopes image the Sun in 8 bandpasses, with a cadence of 12 seconds between exposures in each bandpass. Each bandpass observes a 10Å spectral window (approximate full-width-half-maximum) centered on a strong emission line. The strength of these emission lines vary with temperature so the AIA datasets present us with a qualitative temperature diagnostic tool. The AIA field of view extends out to 1.25 $R_\odot$ and the platescale is 0.6 arcsec. Of the 8 bandpasses on AIA, four of the bandpasses useful for prominence-cavity diagnostics: 304Å, 171Å, 193Å, and 211Å. Each bandpass observes emission from additional weak emission lines due to the width of the bandpass. A detailed discussion of spectral contributions to each bandpass is found in Appendix D. The predicted response of each telescope to the integrated spectral contributions as a function of emitting plasma temperature is shown in Figure 3.3.

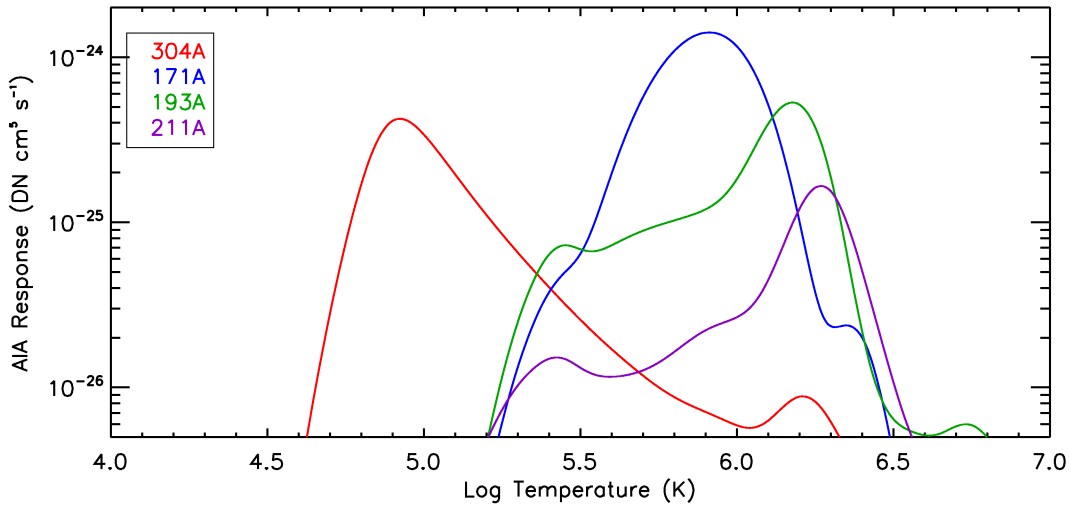

Figure 3.3 The predicted response for each AIA bandpass as a function of temperature. The effects considered are: variation of the coronal spectrum with temperature, the reflectivity of the AIA optics as a function of wavelength, and the CCD response as a function wavelength.

The 304Å bandpass is centered on the singly-ionized Helium Ly-α transition, although it also includes a Si XI line which is generally two orders of magnitudes dimmer. HeII 304Å emission is believed to primarily occur between $0.5 - 1.0 \times 10^5$K although extended optically thin emission throughout the transition region is also possible.

The 131Å bandpass includes several emission lines and its predicted temperature sensitivity is bimodal. The cooler peak is centered near 5×10^5 K and is composed of Fe VIII and Mg V emission. The hotter peak is centered near 12×10^6 K is composed of FeXX and Fe XXIII lines. This hot component is believed to only be present in the corona during strong flaring events, which implies that the ambient 131Å data is primarily imaging cool plasma. Through a combination of atomic physics and detector efficiencies, the observed signal in this bandpass is a factor of 20 lower than the 171Å bandpass, which also images cool plasma.

The 171Å bandpass is centered over a blend of Fe IX and Fe X emission which is strongest at a temperature of 1 MK. These are the strongest lines by an order of magnitude but there is a transition region component between 2.5-5$\times 10^5$ K formed by O V-IV. The 171Å bandpass data has the highest count rate and signal to noise ratio of all the AIA bandpasses (in the quiet sun).

The 193Å bandpass centers on an Fe XII transition which is characteristic of 1.5 MK plasma. Three FeXII ground transitions exist within the bandpass: 192.4, 193.5, and 195.2Å. Weaker FeVIII lines are also present.

The 211Å bandpass is centered on a Fe XIV transition at 211.3Å. In terms of ionization equilibrium, FeXIV reaches a peak ionization at 2 MK. 211Å is one of the more pure bandpasses in terms of spectral blends, but its diagnostic value is damped by its signal strength. 211Å data tends to be a factor of 5 lower in signal than 193Å data.

SDO/AIA allows us to image the solar plasmas with the temperature range of 0.05-2 MK. In practice, the observations provide a convolution of many different temperature structures which complicates our interpretation. Moreover, the data contains instrumental effects and observational uncertainties, which we must derive and understand to accurately state our measurements.

Throughout this section, we will be discussing two particular prominence-cavity datasets.

The first is a 30-hour dataset collected between 28-Feb-2011 09:00UT and 1-Mar-2011 15:00UT, hereby known as D1. The cavity of interest is off the northwest limb at a latitude of 60°. Based on the duration of visibility, the longitudinal length is estimated at 52° or 320 Mm. The second is a 36-hour dataset collected between 10-Aug-2011 00:00UT and 11-Aug-2011 12:00UT, hereby known as D2. This cavity is off the southeast limb at a latitude of -51°. The longitudinal length is estimated at 38° or 340 Mm. Each dataset is composed of full resolution data at 6 minute cadence. Each image in the dataset is the result of median filtering 5 sequential images to increase signal-to-noise ratio.

The first steps to understanding the role of dynamics in cavities is to understand statistically how the cavity differs from the surrounding streamer.

3.3.2 Characterization of Prominence-Cavity Structure in EUV

Figure 3.4 displays the D1 cavity in 5 AIA bandpasses. The 304Å bandpass displays the cool, dense prominence. This particular prominence extends 18 Mm above the limb and has an apparent width of 30 Mm. There is no clear gap between the limb and lower boundary of the prominence.

Figure 3.4b shows the prominence in 131Å. The 131Å bandpass data theoretically contains emission from a FeVIII line (blended with the primary FeXXIII line). The 131Å bandpass simply does not have enough signal to aid in this analysis.

The signal in the 171Å bandpass is much stronger than 131Å. The prominence appears in emission. This emission is peculiar but ubiquitous in prominences. The peak ionization temperature for Fe IX is 8 times higher than that of He II, but there is apparent cospatial 304Å and 171Å emission in the prominence. The explanation for this phenomenon is the "prominence-corona transition region" (PCTR) [Orrall and Schmahl, 1976]. The most basic interpretation is that along the lines of sight which intersect the prominence,there is emission from coronal, transition region, and condensation plasma. The 171Å emission we see in the prominence is being emitted by the transition region between condensed plasma and the corona.

The 193Å bandpass shows the cavity very clearly as an emission-depletion feature. The

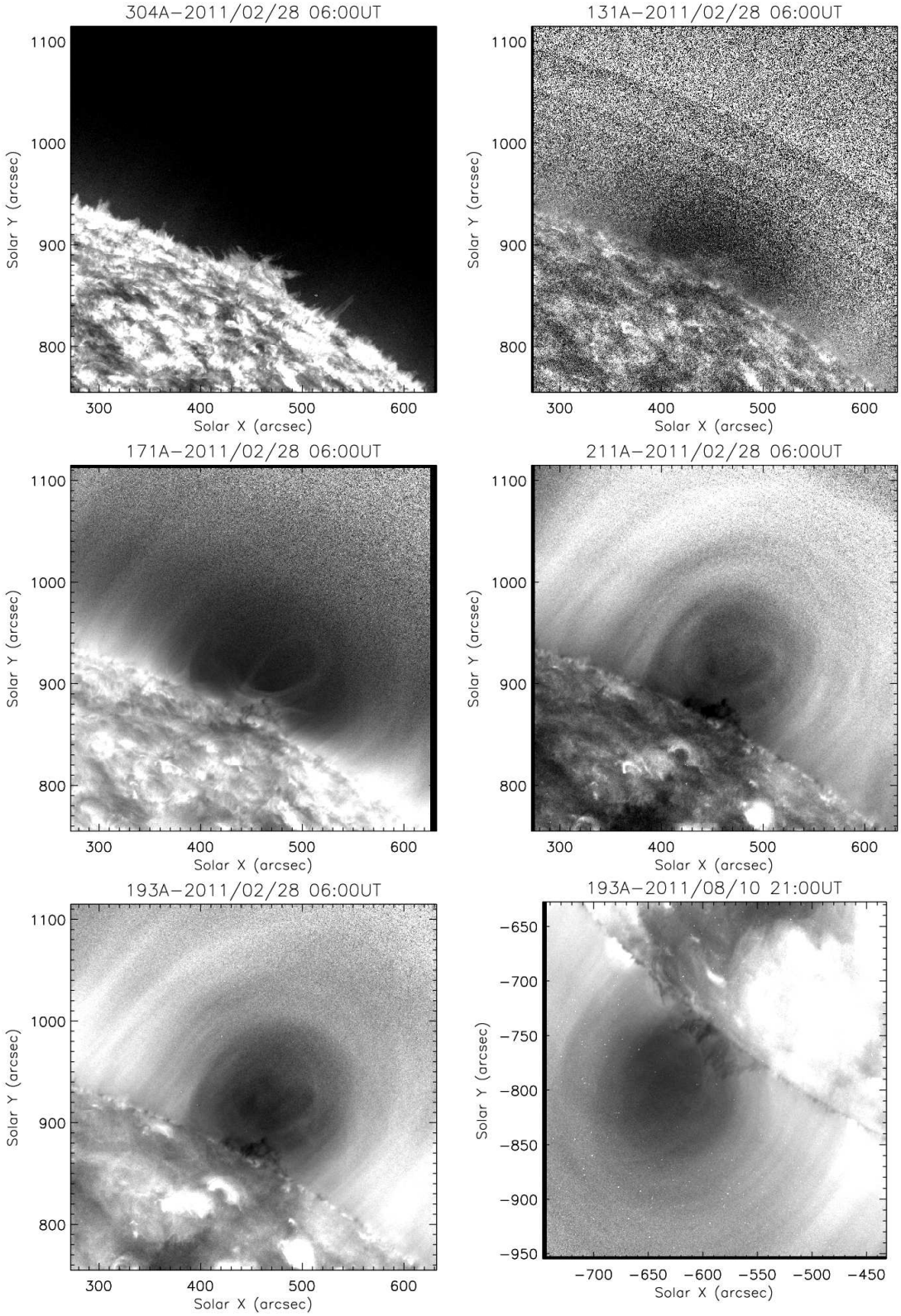

Figure 3.4 Maps in several SDO/AIA bandpasses of cavity D1 (a-e) and D2 (f). HeII 304Å (a). FeVIII/FeXXIII 131Å (b), FeIX/FeX 171Å (c), FeXIV 211Å (d), FeXII 193Å of D1 (e) and D2 (f). Data have radially vignetted to promote structural contrast.

coolest mass of the prominence can be seen in absorption, which is formed by bound-free continuum absorption mostly due to H I. For reference, a 193Å image of D2 is also presented in Figure 3.4f.

The cavities in D1 and D2 differ primarily in two ways. First, D2 is centered around a more angled neutral line. It appears to move north to south as the cavity rotates onto the solar disk. This has the affect of diffusing the contrast between the cavity interior and the streamer. Second, the streamer surrounding the cavity in D2 is brighter than the streamer in D1.

The 211Å dataset looks similar to the 193Å dataset in D1. There is a practically indiscernible difference between cavity morphology as seen between 193Å and 211Å.

3.3.3 Temporal Statistics on Emission Variability

Figure 3.4 served to qualitatively present the morphological differences of the prominence cavity in the various AIA bandpasses. We will now develop a set of statistics to quantitatively describe how the time-dependent cavity differs from the streamer. The AIA observations can be described in the following notation:

$$ {}^{\lambda}\mathbf{I}_t^{ij} \tag{3.1}$$

where $\mathbf{I}$ is the observed intensity (in data number) in bandpass λ at time t for CCD pixel ij. We are attempting to understand the time dependent plasma processes ongoing in the cavity and how those properties differ from the streamer, thus we will largely be ignoring the spatial coordinates ij. Instead we will subdivide the dataset into regions: streamer, cavity, and prominence. The subdivided regions are shown in Figure 3.5. Figure 3.6 illustrates how the median intensity (in time at each individual pixel) in 193Å varies between the streamer and the cavity as a function of radial height in the plane of the sky. The cavity data is presented as red points, while the streamer data is presented as black points. The cavity profile is everywhere reduced compared to the streamer at the same height. This emission depletion varies between 20-50%. Assuming an isothermal corona and ignoring projection effects, the $\int n^2 d\ell$ emission relationship would imply a 29% density depletion. This is typical of cavities as reported by Fuller and Gibson [2009]. To analyze the time-dependent variability in the the AIA data, we will use statistics based on the

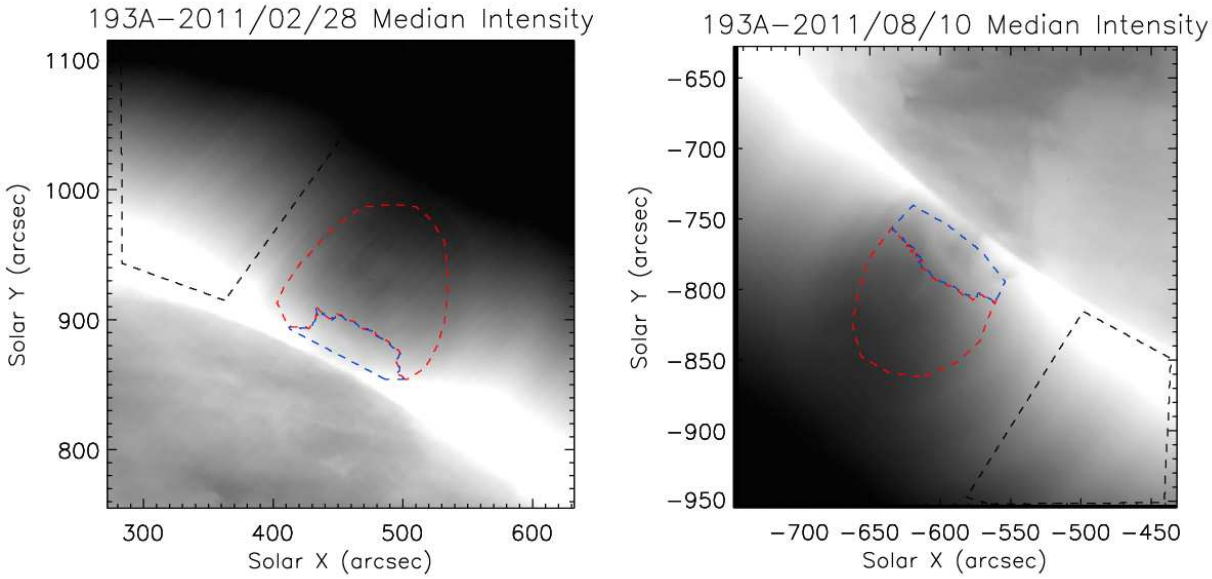

Figure 3.5 Time averaged maps in 193Å for D1 (left) and D2 (right). The red dashed contour denotes the regions selected as cavity. Blue region is prominence. Black region is streamer. These color codes are used in Figures 3.6 and 3.7 as well.

time series of intensity at every pixel within the dataset. Figure 3.8 shows histograms based on the intensity time series. If the emitting structure did not vary in time, these histograms would follow a Poisson distribution.

We have a created a statistic, V^{ij} referred to as variability, designed to quantify the degree to which the intensity of a given pixel varies as a function of time. Variability is given by

$$V^{ij} = \frac{I^{ij}_{MAX} - I^{ij}_{MIN}}{I^{ij}_{MED}} \tag{3.2}$$

where I^{ij}_{MIN}, I^{ij}_{MAX}, and I^{ij}_{MED} represent the intensity value that pixel ij is brighter than through 95%, 5%, and 50% of the time series, respectively (I^{ij}_{MED} will be referred to as median intensity). This statistic is akin to the variance, however the nature of the intensity distributions (i.e. asymmetric) does not make variance a particularly illustrative statistic. Whereas variance weights the entirety of a distribution, our variability statistic cares specifically about the "wings" of the intensity histograms. It measures how the intensity span of the wings compares with median intensity.

Figure 3.7 plots variability in the three structural regions for 171Å, 193Å, and 211Å. The upper row of plots presents variability versus radial height. Examining the streamer distributions for the three bandpasses, we find there is a linear relationship between variability and altitude for all bandpasses. Moreover, the distributions are fairly tightly clustered. The cavity and prominence distributions are not so simple. The 193Å and 211Å both show variabilities which are stronger in the cavity than the streamer. The prominence shows higher variability than the cavity at low heights. In the 171Å distributions, there is a striking difference between the cavity region and the streamer region. The cavity has a variability that is a factor of 4 higher than the variability of the streamer. The differences between the variability distributions illustrate that the cavity is much more variable than the streamer, but specifically in the cooler 171Å bandpass.

The lower row of Figure 3.7 presents the variability data as a function of median intensity. While the upper row illustrated that the cavity is more variable than the streamer, it does not describe the significance of that variability. To define the significance of the statistic, we must define a baseline for what the expected observational error should be be. With the AIA data, this is

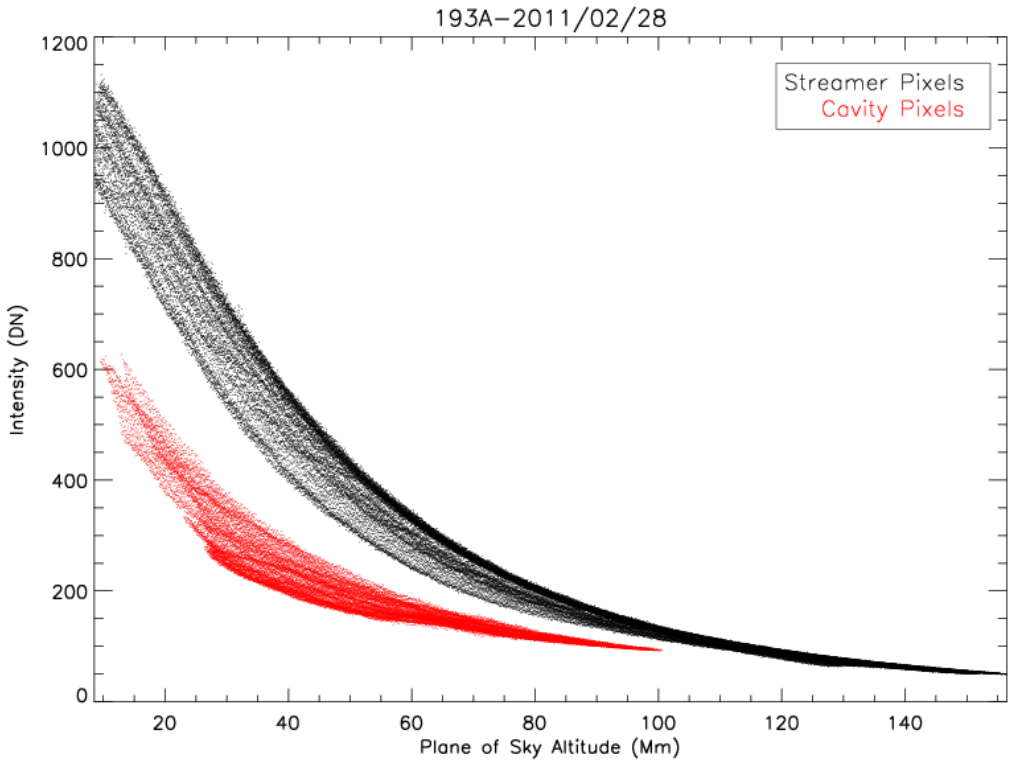

Figure 3.6 Radial profiles of the median intensity, $\mathcal{I}^{ij}(p = 0.5)$, for D1 in 193Å. As in Figure 3.5, red points are extracted from the cavity region, black points are extracted from the streamer region.

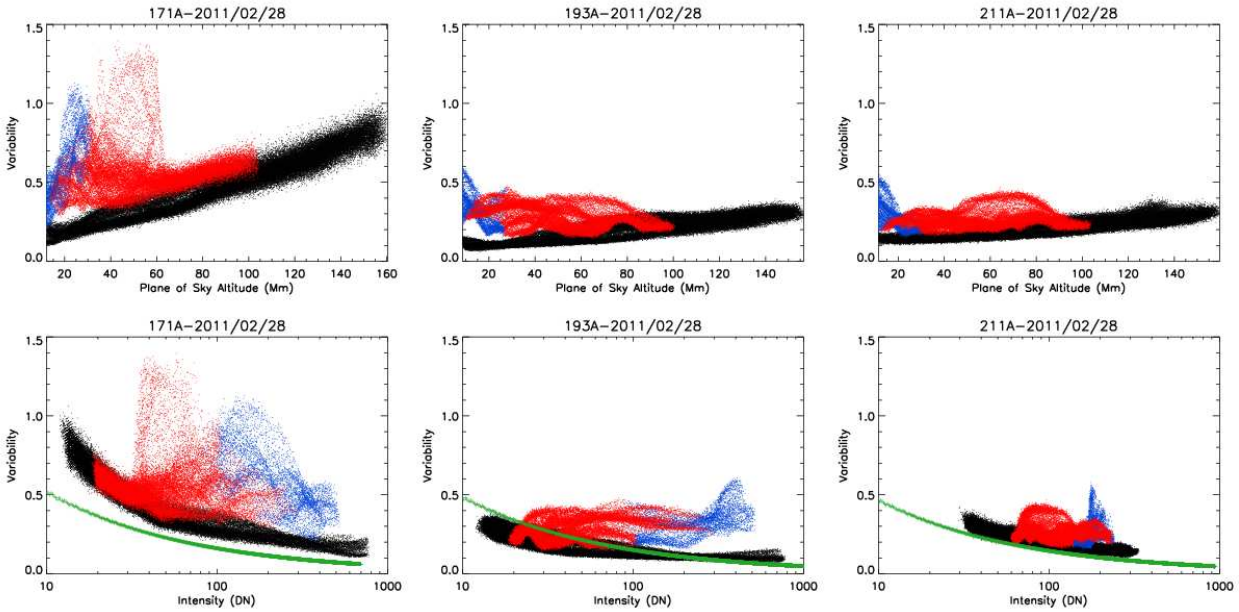

Figure 3.7 Variability statistic plotted against radial height (a-c) and against intensity (d-f) for D1 in 3 different bandpasses: 171Å (a and d), 193Å (b and e), 211Å (c and f). The green profiles are the theoretical Poisson-noise variability. Otherwise, the color code is based on the regions of Figure 3.5.

challenging for two reasons. First, due to the volume of data, the AIA datasets are only retrievable "Level 1" data so the engineering level data (flat field and dark current) are not available, although these systematics have been accounted for at Level 0 to Level 1 conversion. Additionally, bandpass imagers cannot photon count because there is an indefinite range of photon energies impinging on the detector. Due to the non-uniform energy response of the detector, this does not allow a singular photon to electron to data number gain to be assigned. In the lower plots, the expected Poisson noise variability based on the preflight detector calibration is plotted as a function of intensity as green points. In general, the Poisson variability is a close match to the streamer distributions. The 211Å data is perhaps the clearest example of this. The offset between the streamer distribution and Poisson noise can be attributed to a small variability in emission.

The most important feature to take away from Figure 3.7 is that the variability of the cavity in 171Å is excessively strong compared to both the streamer and the baseline Poisson noise. There is also excessive variability in the cavity compared to the streamer in 193Å and 211Å, but the 171Å data is a factor of 3 more variable. Through this statistical analysis, we have identified a unique characteristic of the EUV emission in cavity through the basis of spatially-independent temporal statistics. Now, we will take the next step by honing in on the strongly variable regions of 171Å cavity. What is it about the intensity distributions in the cavity region that increases this statistic?

Figure 3.8 shows the histogram for a strongly variable cavity point in the 171Å and 193Å bandpasses. The variability in the 171Å data is over twice that in 193Å. In terms of the distributions, the most notable feature is the strong asymmetry in the 171Å distribution, which has a high intensity tail. The 193Å histogram, in contrast has a symmetric normal distribution. We have chosen statistics to highlight the nature of these distributions, as the intensity histograms plotted in Figure 3.8 are typical of the cavity. The high intensity wing in the 171Å histogram make both mean and variance (statistics of specific relevance in a normal distribution) of little illustrative value.

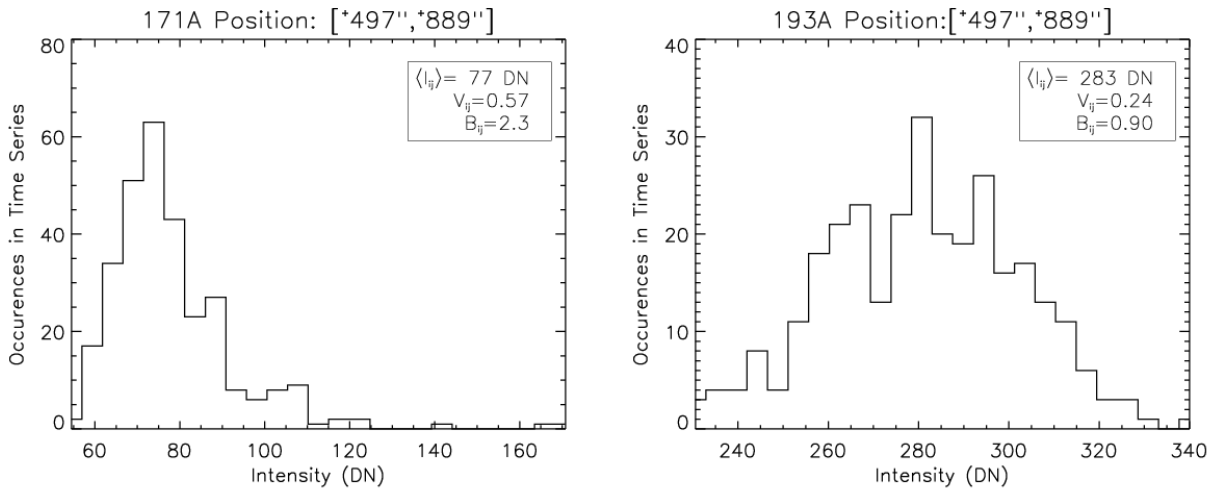

Figure 3.8 Intensity histograms for the intensity of a cavity region pixel of D1 in the 171Å bandpass (left) and the 193Å bandpass (right).

Printed along with the variability statistic in Figure 3.8 is the skew statistic:

$$B^{ij} = \frac{I^{ij}_{MAX} - I^{ij}_{MED}}{I^{ij}_{MED} - I^{ij}_{MIN}}. \tag{3.3}$$

Whereas the variability looks at the spread between the high-intensity and low-intensity wings of the intensity histograms, the skew statistic looks at the relative intensity-difference between congruent positions in the histogram, specifically the brightest 5% of intensities and the dimmest 5% of intensities. The skew is a positive number, and for the AIA datasets it varies between 0.1 and 10. A skew of 1 would imply a perfectly symmetric distribution. We find the lower cavity is characterized by high skew distributions ($B_{ij} > 2$) in the 171Å bandpass but not 193Å bandpass. This signifies that the variability in the 171Å cavity is characterized by short duration, strong brightening events.

Based on the skew and variability statistics, we have found that the cavity exhibits very different temporal variations in intensity than the streamer. Based on these statistics, we now inspect movies of the cavity to determine the spatial and temporal coherency of the 171Å brightening events.

3.3.4 Observation of Prominence Horns

By examining movies of the 171Å bandpass data, the nature of these variability features become more apparent. Figure 3.9 illustrates a subregion of the cavity going through a transient 171Å brightening. The pictured subregion includes the prominence and the western half of the cavity. Over the course of an hour, we observe the formation of a collimated "horn" in the 171Å data which extends nonradially from the 304Å prominence into the lower cavity. The apparent width of the feature is 4.2 Mm and the apparent length is 63 Mm. The maximum brightening (contrast relative to background) is 16%. The spatial geometry of the feature extends from the prominence along a concave up loop-segment into the cavity.

The correlation between the 171Å feature and the structure of the other AIA bandpasses should also be considered. In between 2011-02-28 23:24UT and 2011-03-01 00:24UT, we find that the prominence emission, as seen in the 304Å bandpass, has also changed. A co-spatial, co-temporal

extension of the prominence sits at the base of the 171Å horn. The prominence gradually extends a maximum of 13 Mm along the 171Å feature before gradually contracting.

This observation demonstrates that there is a coronal component associated with prominence dynamics, and moreover the dynamic coronal feature projects into the cavity interior. These correlated features imply there is a magnetic and energetic link between the cavity and prominence, which leads us to the question: what is the physical source for the prominence-cavity dynamics? To address this question, we will look towards statistical analysis of the many prominence horns to identify physical characteristics which will aid us in determine the cause and consequence of these features.

3.3.5 Method of Analyzing Prominence Horns

The first step in this analysis is to build a database of events. As we previously established, the most dominant form of emission variability in the cavity are collimated regions of strong brightening in 171Å emission. We use this trait as the defining characteristic of feature identification, and we use visual inspection to identify potential features in both D1 and D2. We originally attempted to develop an automated approach to extracting features through a spatial-filtering, wavelet approach similar to the OCCULT algorithm suite developed by Aschwanden [2010]. These techniques are not well suited to off-limb corona, where three effects hamper them: the strong radial intensity gradient, the relatively diffuse structure, and the lower signal-to-noise ratio. Instead of investing time into automating the initial processing, we have opted to manually identify potential features, which are later verified through through tests described later in this section. We identify a total of 48 potential features (in 66 total observing hours) between our two datasets: 27 features in D2 and 21 features in D1.

To quantify the changes in intensity as a function of time along each feature, we synthesize a curved slit which is selected to overlay the potential feature. The data from the 193Å, 171Å, and 304Å datasets are extracted in the vicinity of the slit and are transformed into a curvilinear coordinate system, the axes being distance along the slit, y', and distance from slit-center, x'. The

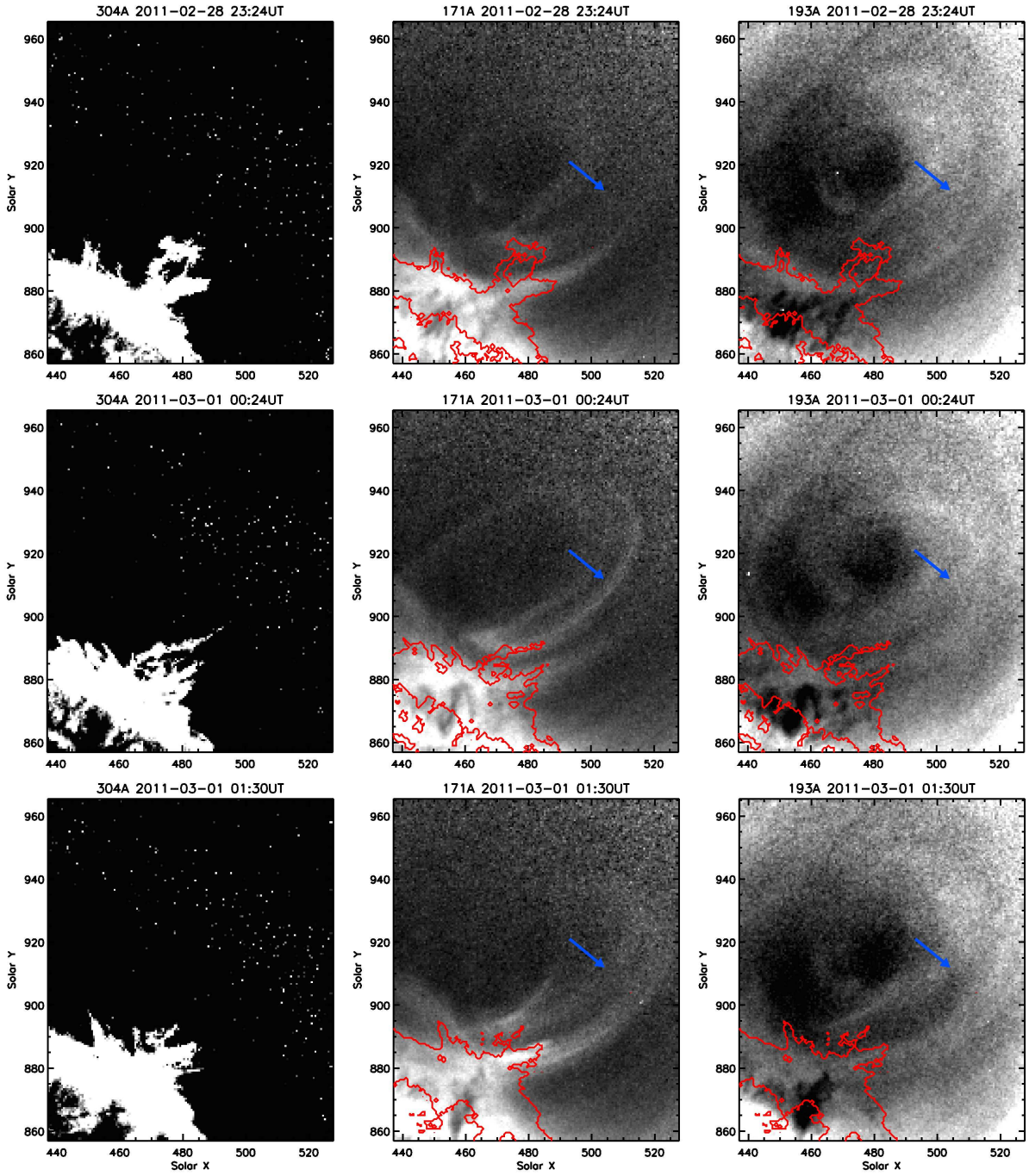

Figure 3.9 Snapshots at 3 times in 3 bandpasses of a prominence horn, zoomed into D1. Prominence material, HeII 304Å emission (left). Transition region FeIX-X 171Å (middle). Coronal FeXII 193Å (right). The horn is 171Å brightening feature which the blue arrow points to. It remains nominally brighter than the background for 1.5 hours. The red contours show the perimeter of strong 304Å emission. The horn in cospatial with an extension of the prominence. There is weak, correlated signal in 193Å radially above the blue arrow, but overall the structure in 193Å is distinct from that of 171Å. A movie of this figure is presented in the electronic version.

transformation is done using a triangulation, nearest-neighbor interpolation scheme. An example of a transformed curvilinear dataset is shown in Figure 3.10. In the temporal domain, we extract data from 2 hours prior to the potential feature and 3 hours after.

In order to quantify the time-dependent intensity variations in these datasets, we produce light curves as a function of position along the slit. The curvilinear dataset is divided into background regions (5 pixels$< |x'| \leq 15$ pixels) and feature regions ($|x'| \leq 5$ pixels). These regions are then coadded at 5 pixel intervals in the y'-direction (along the slit). A gaussian temporal smoothing is applied to the light curves, with a width of 9 minutes. We present light curves which display the ratio of feature intensity to the background intensity at each segment along the slit as a function of time. Example plots of these light curves are shown in Figure 3.11. The color of each curve denotes in position along the slit. A colorbar matching the y' coordinate is plotted in between maps in Figure 3.10. A vertical offset has been applied to the light curves shown in Figure 3.11 so that they do not lie on top of each other.

The final step in the processing of our datasets is finding and fitting the locations of minima and maxima of each individual light curve. This process serves two purposes: it allows us to automatedly check to make sure that the potential features we identified by inspection are actually coherent structures, and it allows us to develop statistics on the onset, duration, and time-lag between different bandpasses of each event. For each light curve, we use an algorithm to determine the location of local maxima between $0 < t < 40$. For a potential feature to be labeled as an event, we require that at least 8 sequential heights along the slit ($\approx$17 Mm) have local temporal maxima within 3 timesteps of both the neighboring heights. This basic test is a simple method which checks the coherency of a potential feature. Applying this filter to our 48 potential features, we return 45 confirmed prominence horns.

We extend this technique to measure the start and end times of each brightening. These time intervals are assessed by extracting the nearest two local minima on either side of the prominence-horn maximum. We apply a linear fit to these data (time of event vs. position on the slit) where

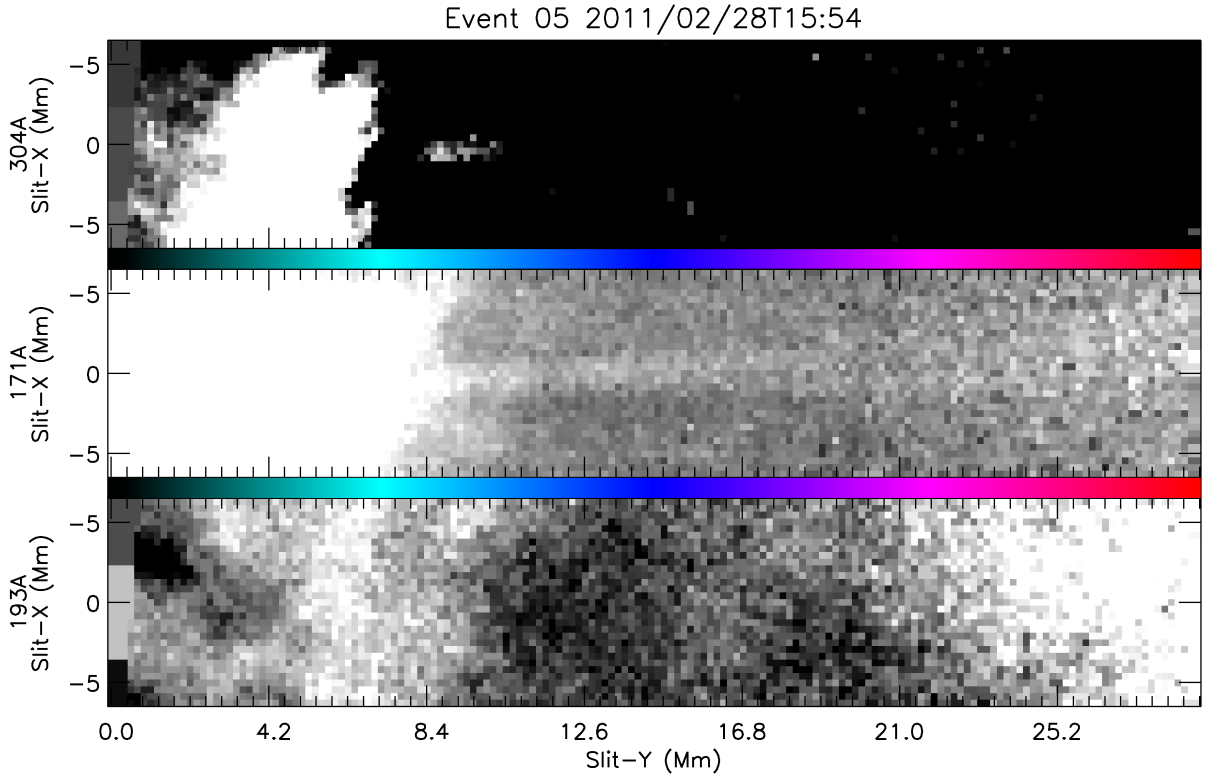

Figure 3.10 A single horn image, transformed into curvilinear coordinates using a curved slit. In this event, a blob is ejected from the prominence to a slit-height of 9 Mm. This ejecta coincides with a coherent 171Å brightening which extends from 5 Mm to 23 Mm. There is also a correlated 193Å brightening which is not visible in this map because it has not been background-divided. The color table plotted horizontally between maps indicate the slit-height of the light curves which are plotted in Figure 3.11.

the weight of each minima is inversely proportional to its depth relative to the maxima:

$$\sigma = (I(t = t_{MAX}) - I(t = t_{MIN}))^{-1}$$

where the linear fit takes the form

$$t' = m * y' + t_0. \tag{3.4}$$

The quantity t' is the best-fit time of event (event in this context being the initial brightening, peak brightness, end of subsequent dimming). The derived quantity m has units of km^{-1} s. Its reciprocal is therefore a velocity which gives us an estimate of how the observed disturbance propagates along the slit. The fitting routine minimizes the quanity,

$$\chi^2 = \sum_{y'} \frac{(t_{obs}(y') - t'(y'))^2}{\sigma^2}. \tag{3.5}$$

where t_{obs} is the observed timestep of the event. The weighting function values deeper minima more than shallow minima, and strictly-based on number of points, minima which are well correlated between several heights result in lower χ^2 values. Figure 3.11 has black lines overplotting the derived linear fits for the feature initiation, peak, and dimming.

3.3.6 Results

Using the above described methodology, we will now go into characterization of prominence horns. The basic configuration for 171Å events is as follows: a rapid, large-scale brightening begins with its base near the prominence. From onset time to peak brightness takes 85 minutes with a standard deviation of 19 minutes. The brightness enhancement is not constant with distance along the feature, and the brightest point along the feature tends to occur within the first 15 Mm. The peak brightness contrast generally decreases as a function of distance along the horn, such that the horn fades into the background at higher heights. We observe that there is a weak correlation (Pearson coefficient: 0.26) between the peak brightness of a horn and its length. For the 45 measured horns, the median peak brightness contrast is 34%, and 9 features have a peak brightness over 50%.

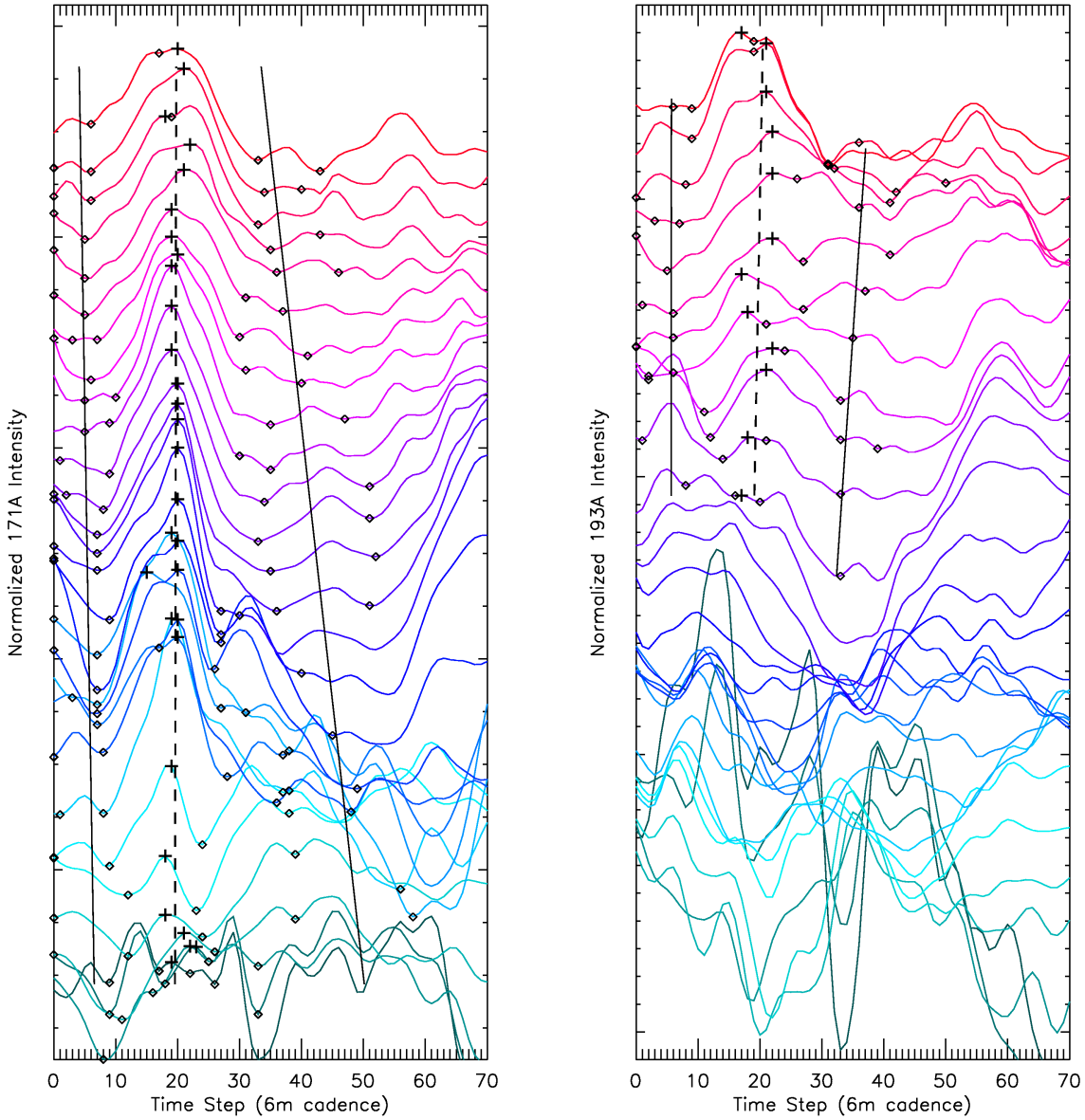

Figure 3.11 Light curves of Event 5 (shown in Figure 3.10) in the 171Å bandpass (left) and the 193Å bandpass (right). The color of the light curve denotes its height along the slit (see colorbar, Figure 3.10). The teal curve is extracted from a height of 4 Mm while red curve is extracted at a height of 27 Mm. The light curves are offset in the vertical direction for clarity. The time of maximum brightness contrast of the feature is marked with black crosses, while the surrounding minima are marked in black diamonds. The linear fit (Equations 3.4 and 3.5) is overplotted with black lines to show the temporal progression of brightening event as a function of slit-height.

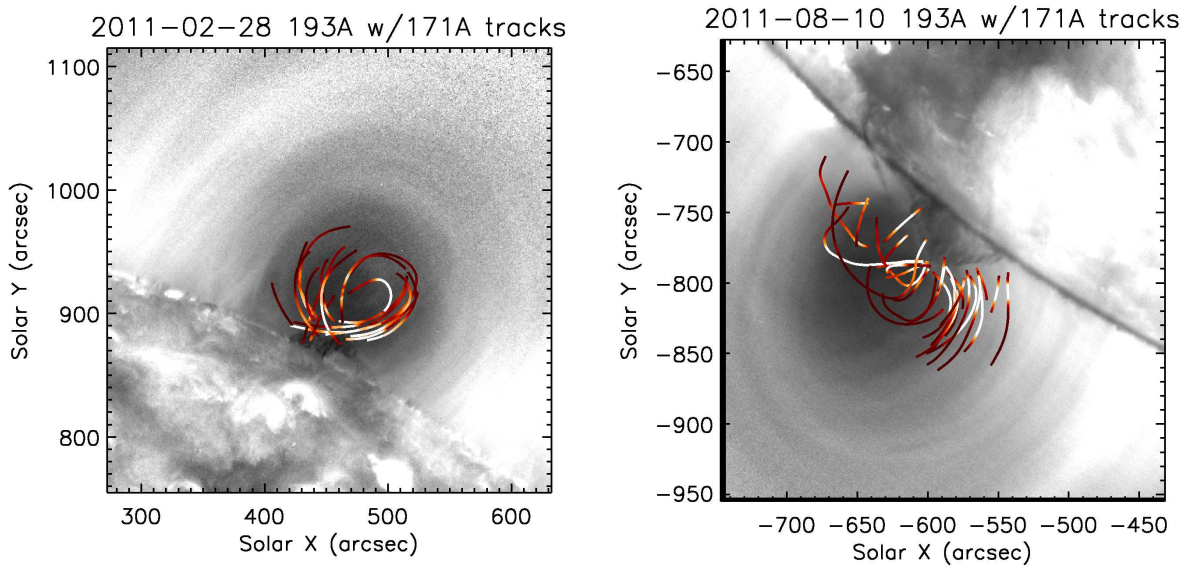

Figure 3.12 193Å map of D1 (left) and D2 (right) in grayscale. Location of horns in the 171Å bandpass. Color table advances black to orange to white with increased maximum (in time) contrast to background.Range: 4% to 50%

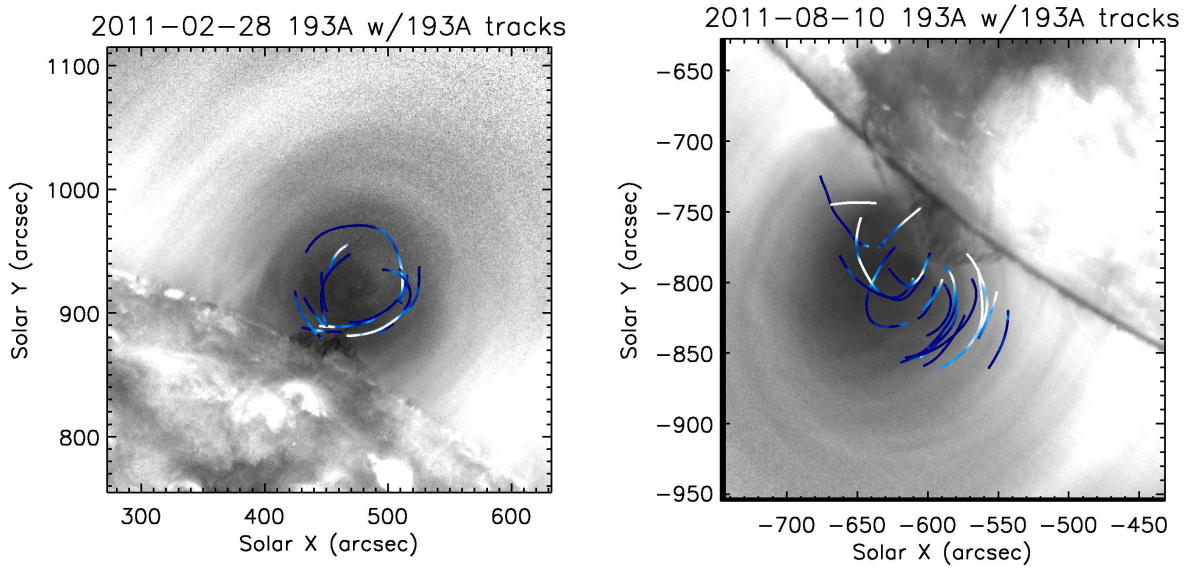

Figure 3.13 193Å map of D1 (left) and D2 (right) in grayscale. Location of brightenings in the 193Å bandpass associated with horns. Color table advances black to blue to white with increased maximum (in time) contrast to background. Range: 1% to 20%.

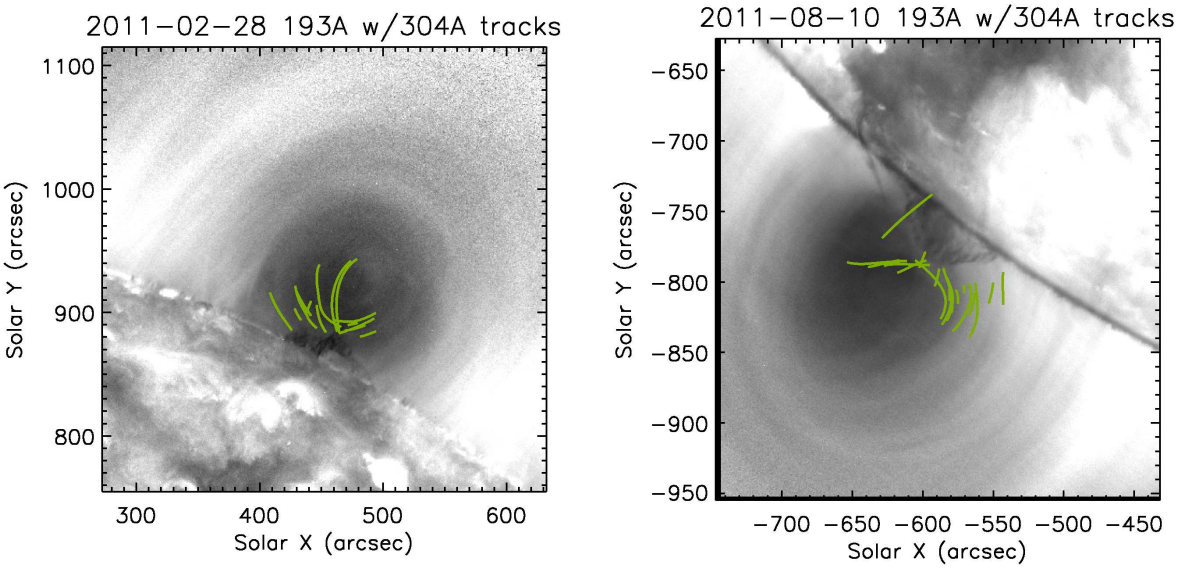

Figure 3.14 193Å map of D1 (left) and D2 (right) in grayscale. Location of prominence extensions in 304Å emission associated with the horns. These tracks represent the range of prominence extension or ejection. No color range is applied.

Maps showing the positions and strengths of the 171Å horns are shown in Figure 3.12. Both maps illustrate the proximity of the these coronal features to the prominence. The dense, absorbing regions of the prominence appear to be the emanation point. The structure is more complex in D2. In the 304Å movie, we are able to see that there are two unique prominence spines. The smaller northern spine is observed exchanging plasma with the larger southern spine, which is centered under the cavity. These "connection" events have similar traits to the more vertical horns in the 171Å light curves despite there different geometries. However, they do not typically show much structure in 193Å. For D1, the overall appearance of the 171Å brightenings are concave loop segments surrounding an axial structure located at ($^{+}475''$,$^{+}915''$) at a height of 1.07 $R_{\odot}$.

Of the 45 horns found in the 171Å bandpass, 32 exhibit correlated brightenings in 193Å bandpass data. The associated 193Å features are plotted in the maps of Figure 3.13. Of the events which do show correlation between 171Å and 193Å light curves, there is generally not a correlation throughout the entire horn. The 193Å brightenings tend to occur in the upper sections of the 171Å horns, the median offset is 6.3 Mm above the 171Å base. The most striking difference between the 171Å and 193Å features are that the 193Å events are significantly dimmer. The median peak brightness is 7% in 193Å compared to the 34% in 171Å.

From the 32 joint 193Å-171Å events, we have 450 co-spatial light curves which exhibit correlation. From these points, we measure an average time lag of -0.6 minutes ±23 minutes between the peak brightness in 171Å and the peak brightness in 193Å. The same applies for the event onset time. These measurements show there is not a clear temporal pattern the 193Å brightening and 171Å brightening.

Maps which show the extent of 304Å features correlated with 171Å horns are shown in Figure 3.14. We find 34 of these events. Unlike Figure 3.12 and 3.13, there is no color range applied to the 304Å features. We did not extend the same intensity analysis to the 304Å dataset because of the large intensity gradients on small-spatial scales within the prominence. The basis of our comparison with 304Å data is changes in the perimeter of the prominence, as was seen in Figure 3.9. There are generally two type of events we observe in the 304Å data. In 20 of the 304Å events, we

observe simple extensions of the prominence. In the other 14 events, we actually observe ejection of prominence material such that no 304Å emission is detected between the 304Å ejecta and the prominence itself. In both cases, the median rise time and fall time is 24 minutes. The median maximum length for ejecta is 10.5 Mm, while the median maximum length for extensions is 7.6 Mm. In general the rise of 304Å material begins after the initiation of the 171Å brightening by 30 minutes. We find a Pearson coefficient of 0.44 for the correlation of the peak 304Å extension time and the time of peak 171Å brightness.

Velocities are a fundamental quantity associated with dynamics, however this is a difficult measurement to make in prominence horns. We do not have spectral Doppler observations for these cavities, and the application of feature tracking techniques is not obvious; our features appear to maintain a constant spatial orientation and position over their 3 hour duration. As described in Section 3.3, we have attempted to assess a velocity based on the time of initial brightening and peak brightening. While this quantity has physical units, we must be clear on what is being measured in terms of basic physics: *there is a perturbation happening along a coronal loop which is changing the amount of photons being emitted along that loop as a function of time.* We are measuring the time that a discernible change in photoemission has occurred at a particular position along the loop relative to other positions on the loop.

The derived velocities based on the initial brightening and the peak brightening are shown in Figure 3.15 as a function of feature length and reduced χ^2 of the model fit (using Equations 3.4 and 3.5). Feature length is important in this diagnostic because we have more points to track the apparent propagation of the feature. The x-axis is due to the nature of the fitting. The fit-parameter, m is converted into a velocity by

$$v = \frac{\Delta y'}{\Delta t} m^{-1}$$

where $\Delta y'$ represents the plane of sky distance of 5 slit-pixels (2100 km) and Δt is the cadence of the data (360 s). A negative value of m would imply a propagation from higher radial heights downward, while a positive m implies a propagation from the prominence upward. The median

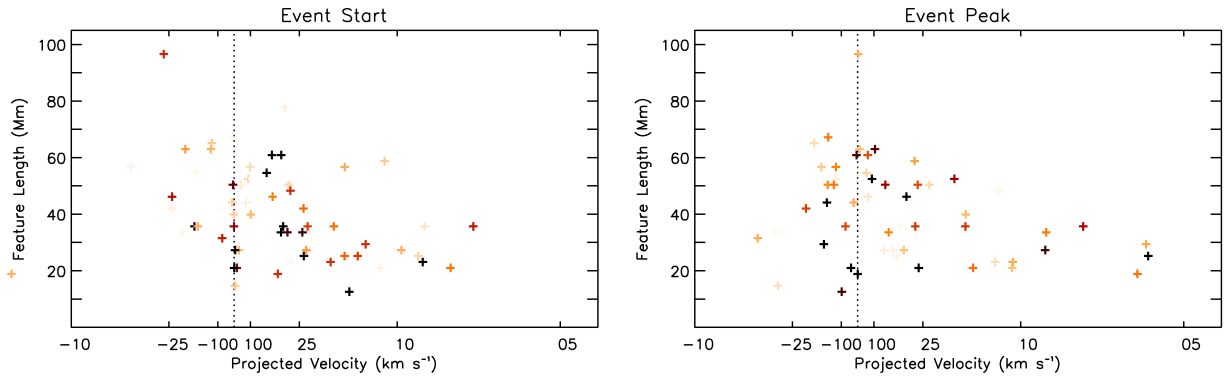

Figure 3.15 Scatter plots of the derived horn velocity along the slit versus horn length. Color table advances black to orange to white with increasing χ^2 value. Derived velocity for the horn initiation (left) and horn maximum (right). Black crosses represent the most reliable velocities. χ^2 range for initiation: 0.1 to 1.4; χ^2 range for maximum: 0.8 to 6.5. The black dotted line represents an infinite and directionless speed ($m = 0$).

derived m for the 171Å data for the brightness initiation is 0.056 which corresponds to a velocity of 104 km s^{-1}. Given the errors in measurement, we are not able to discriminate between high speed ($|v| > 100$ km s^{-1}) features moving upward and downward.

The derived velocities in Figure 3.15 are sparsely distributed, but the highest quality fits tend to cluster between $|v| > 20$ km s^{-1}. These velocities are intriguing considering the event durations. A transient disturbance traveling at 20 km s^{-1} would advance 60 Mm in 5 minutes. Our observed features last longer than 1 hour. This implies that the propagation of the perturbation and the subsequent equilibration or damping of the perturbation are based on different energetic processes and timescales.

3.3.7 Estimate of Horn Density

We wish to estimate the density of the horns, and this requires us to account for projection effects. Past efforts by Schmit and Gibson [2011] and Kucera et al. [2012] have gone through modeling efforts to quantify the density and temperature effects which are manifest in optically-thin EUV emission. Extending this work to the D1 cavity, we can make a back-of-the-envelope calculation for prominence horns. Let us consider a line of sight which observes a 38° long cavity embedded with in a 53° long streamer. Using the forward modeling technique of Gibson et al. [2010], we predict there should be approximately 5×10^{28} cm^{-5} of emission measure along the line of sight at a height of 1.07R$_s$. Assuming an isothermal cavity and streamer of 1.7 MK, we can write the intensity ratio of the prominence horn to the static cavity in the form,

$$\frac{I'_{171}}{I_{171}} = \frac{\mathcal{A}_{171}(T = 1.7\text{MK}) * \text{EM}_s + \mathcal{A}_{171}(T = T_{peak}) * \text{EM}'}{\mathcal{A}_{171}(T = 1.7\text{MK}) * \text{EM}} \tag{3.6}$$

where $\mathcal{A}$ represents the AIA temperature response function per unit emission measure. The forward model predicts that most of the ambient 171Å emission comes from low-density, weakly-emitting plasma, but the plasma is quite extended (the full-width half-max for emission measure is ±70 Mm out of the plane of the sky). The ratio of $\mathcal{A}_{171}(T = 1.7$ MK$)/\mathcal{A}_{171}(T = T_{peak})$ is approximately

4.5%. We have divided emission measure distribution into three components

$$\mathrm{EM} = \int_0^\infty n^2 \; d\ell,$$

$$\mathrm{EM}_s = \int_{2.5\ Mm}^\infty n^2 \; d\ell,$$

$$\mathrm{EM}' = \int_0^{2.5\ Mm} n'^2 \; d\ell,$$

where n' is the horn density and n is radial density profiles from Schmit and Gibson [2011]. These emission measures are the full line of sight, the horn region in the ambient cavity, and the horn region during the 171Å brightening respectively. We estimate the line-of-sight width of the horn at 2.5 Mm which assumes a circular cross section. Substituting in these equations, we can solve the minimum density perturbation necessary to produce a 50% increase in 171Å intensity

$$\frac{n'(\ell = 0)}{n(\ell = 0)} \approx 5.$$

This multiplicative increase in density assumes that the plasma has also cooled to 1 MK, where it emits 20 times more strongly than at 1.7 MK, the original imposed temperature. This assumption makes it such that the predicted density change is a minimum value, whereas a weaker temperature perturbation would result in a weaker enhancement in emission.

We can apply this same technique for 193Å emission where we use the same temperatures and the derived n' and solve for I'_{193}/I_{193}. We now have the ratio in the temperature response function of

$$\frac{\mathcal{A}_{193}(T = 1.7\ \mathrm{MK})}{\mathcal{A}_{193}(T = 1\ \mathrm{MK})} = 2.4$$

The reduction in temperature which raised the emissivity for the 171Å bandpass by a factor of 20, acts to reduce the 193Å emissivity. However, the strong predicted density enhancement more than balances the temperature-dependent emission loss. The predicted ratio I'_{193}/I_{193} has a value of 3% compared to 50% for I'_{171}/I_{171}. In other words, the intensity produced by a corona dominated by > 1.5 MK structure will not vary drastically for localized (short line of sight contributions) cool-coronal events. This suggests that horns are cool, dense features relative to the cavity.

3.4 Conclusions

We have demonstrated that the cavity exhibits fundamentally stronger dynamics than the surrounding streamer. This was illustrated through a statistical analysis of EUV observations from the SDO/AIA instrument. In particular, the statistics indicate that the lower-cavity region surrounding the prominence undergoes strong brightening events in the 171Å bandpass, which is typically dominated by 1 MK plasma.

Analyzing movies in the 171Å bandpass, the observations indicate that these events are collimated coronal loop segments, called prominence horns, which extend from the prominence into the cavity. The 171Å emission of horns is often correlated with weakly-enhanced emission in 193Å bandpass,which contains hotter coronal emission. The 171Å emission is often co-spatial with extensions of the prominence material as seen in the 304Å bandpass.

We have gone through many details of these emission signatures, but we have not yet addressed the physical nature of these events. There are several obvious puzzles present in the data. First, how do we explain the apparent co-spatial 304Å and 171Å emission? There is a large temperature discrepancy between the theoretical peak emissivity of HeII 304.3Å and Fe IX 171.4Å. There are two possible explanations: cool blends in the 171Å bandpass or projection effects.

There are cool blends in the red periphery of the 171Å bandpass, in particular resonance lines of OV 172.2Å and OIV173.0Å. Del Zanna et al. [2011] concluded thorough analysis of Hinode/EIS data that the contributions of these lines is limited to a few percent on disk. These lines will not emit strongly in equilibrium because of the large difference between the excitation energy (70 ev) and the temperature associated with the peak ion population (O VI population peaks at 4×10^5 K $\approx$ 35 eV). Radiative recombination could play a role in populating these excited levels in a non-equilibrium processes. However, the magnitude and duration of this recombination emission is unlikely to explain prominence horns.

Another possible explanation for the correlated 304Å and 171Å emission is projection effects. Horns may have a significant component of their geometry aligned along the line of sight. Emission

which appears cospatial would occur along separate segments of an individual magnetic field line. The prominence-corona transition region, which would separate these segments, is predicted to be less than 5 Mm thick.

Another peculiar aspect of prominence horns is the weak correlation between 171Å emission and 193Å emission. There are relative weak separations between the ionization energies for Fe IX and Fe XII. This has the effect that the predicted AIA temperature response function has significant overlap between the 171Å and 193Å bandpasses. Moreover, there is precedence that Fe IX 171Å and Fe XII 195Å emission are often highly correlated in dynamics heating events [Viall and Klimchuk, 2011, Aschwanden et al., 2000]. The most likely explanation for the weak correlation in horns is that the dominant component emission in the 171Å is formed at temperatures less than 0.8 MK. This cool plasma would not have strong emission in the 193Å bandpass. Temperature dependent projection effects may also play a role as described in section 3.4.1.

In Section 3.3, we discussed that there was more variability in the 171Å bandpass than the 193Å bandpass. While horns explain our statistical analysis of the 171Å cavity, the associated 193Å component of the horns does not explain the cavity variability in that bandpass. In examining the light curves, we find that there are intensity variations a factor of 3 larger in the 193Å cavity than the intensity variations related to the horns. The power seems to be strongest for variations with a 4-8 hour period and is more evenly distributed between dimming and brightening events. We believe that it is this variability component that Wang and Stenborg [2010] have studied through their wavelet analysis.

We have created a framework with which we could measure the characteristic velocity of the prominence horns, but found that the spread in the derived values was large relative to the values themselves. We find several examples from our 45 events where an entire 50 Mm long structure undergoes a uniform and *simultaneous* change in intensity. In terms of basic physics, these large-scale isotropic changes are most readily explained through thermal conduction.

The details of conduction are presented in Appendix A. Conduction is a diffusive operator. Given a thermal perturbation on a coronal loop, anisotropic thermal conduction rapidly redis-

tributes the energy associated with the perturbation. These characteristics match the scale (> 50 Mm) and velocity (> 50 km s^{-1}) of horns. In the corona however, thermal changes and density changes are inseparable. Due to the different velocity scales associated with thermal conduction and siphon flows, a change in temperature will always result in a change in density. A change in density, given mass conservation, requires velocities. The hydrodynamic equations must be self-consistently solved to truly understand the implications for any thermodynamic perturbation. Of special interest to these observations is a detailed analysis of a catastrophic cooling model for prominence formation. Chaper 4 will use a hydrodynamic code to synthesize light curves for cooling events along coronal loops.

We have not yet discussed the observed geometry of the prominence horns. Horns are tightly-collimated and exhibit little structural variation over their duration. These characteristics indicate that these are magnetically-aligned structures, or more specifically segments of coronal loops. We have speculated they may be explained as thermal structures,and thermal conduction is dominantly field aligned. Thus, we posit the extracted prominence horns are indicative of the magnetic field geometry of the lower cavity.

In both D1 and D2, a discernible axis can be found which the horns circumscribe. Horns imply that there is a component of the prominence magnetic field which is non-axial. This is an indication that twist is present in the quiescent prominence-cavity system. In observing the cavity in projection however, we cannot be completely certain that these magnetic structures are within the cavity itself.

These observations are the first attempt to quantify the connection between cavity dynamics and prominence dynamics through an observational analysis. We have identifies a strong emission variability connection between the prominence and the cavity, but we have not gone so far as to determine the physical source of these dynamics. In the next chapter, we will use a hydrodynamic loop code to forward model the emission signature for prominence formation through catastrophic cooling. There is a compelling paradigm for the prominence-cavity connection: a mass exchange feeds condensing plasma out of the low-density cavity into the cool, overdense prominence. The

models for catastrophic cooling make predictions on what coronal perturbations are necessary to drive this process. We will test these predictions against the emission variability we have documented in the prominence environment.

Chapter 4

Energetics and the Magnetic Structure of a Flux Rope

The ubiquity with which prominences and cavities are observed together has always suggested that there is a magnetic connection between these structure. We do not have the magnetic observations that allow us to unequivocally prove a magnetic link. However, SDO/AIA has provided observations which demonstrate correlated prominence-cavity dynamics on what appears to be field aligned structures.

We use a one-dimensional hydrodynamic model to compare prominence horns with prominence formation through thermal non-equilibrium. The analysis is complicated by the disparate nature of the one-dimensional model and the three-dimensional (projected onto two dimensions) EUV corona. We find that the primary constraints derived from the observations can be satisfied by the thermal non-equilibrium model. However, a primary prediction of this loop cooling model is that condensation-holding field lines must be more dense than geometrically identical non-condensed field lines. This is contradictory to the primary observational constraint on cavities; they are low density.

To understand the role projection effects play in the observed structure of prominence horns, we dissect the magnetic structure of the flux rope model for prominences. We show that the flux rope is composed of several geometrically distinct magnetic regions. The field lines which can hold prominence material are shown to be contained within small fraction of the flux rope volume. Cooling loops in this region would project throughout the cavity.

We extend our 1D energetic modeling, by solving for hydrostatic balance throughout the

three-dimensional structure of the flux rope. We find the interior of the flux rope has a 30% lower density than the surrounding arcade. The density-depleted structure is formed by the axial field which is not dipped.

By viewing these independent results in unison, we suggest that the flux-rope interpretation for prominence structure can account for the nuances of observed cavity structure. The prominence is formed through a dynamic cooling process, which occurs on dipped field lines. These field lines form a morphological boundary which surrounds the cavity, but they are not density depleted. The central flux-rope region of weakly twisted axial field is the source of density-depleted cavity.

In this chapter we will use two different 1D models to investigate the energetic balance and magnetic structure of the prominence-cavity system. In section 4.1, we will consider the thermal non-equilibrium (TNE) model for the prominence formation. We will apply a 1D time-dependent loop model to dipped flux rope field lines and compare the predicted emission signature to the prominence horns observed in section 3.2. We go on address the compatibility of this model with the observed cavity structure as a whole. In section 4.2, we break down the various magnetic geometries which comprise the flux rope model for prominence structure. Using these geometries, we consider the observational consequences that hydrodynamic and hydrostatic loop models predict over the 3D structure.

4.1 The Thermal Non-Equilibrium Model

The thermal non-equilibrium (TNE) model is a theory that describes the formation of prominences. TNE refers to a specific form of catastrophic cooling, in which heating drives the radiative instability in a coronal loop. This heating function selectively adds energy to the loop foot points. Foot point heating changes the pressure gradient between the loop base and midpoint, and flows respond to equalize the difference. The additional mass in the coronal segment of the loop drives strong radiative cooling. This begins the catastrophic cooling phase of the loop evolution.

A large degree of research has been directed into understanding the nuances of this model. The original paper to describe the TNE model was Antiochos and Klimchuk [1991]. This pa-

per solved the 1D hydrodynamic loop equations with time-dependent heating using a symmetric half loop geometry. The major limitation in this paper is that the numerical method could not handle the strong temperature gradient which occurs between the condensation and the corona, thus the authors only described the loop evolution up to point of condensation. Dahlburg et al. [1998] added an adaptive grid refinement scheme to the loop model which allowed the authors to study the growth rate of the condensation. Following that numerical improvement to code, a set of papers by Karpen and coauthors discusses how the TNE model varies between loop geometries and heating methods. Karpen et al. [2001] found that magnetic dips are not necessary to form condensations. Karpen et al. [2003] examined a variety of different dipped geometries to determine which geometries promoted static or dynamic condensations. Karpen and Antiochos [2008] found that impulsive heating could also produce condensations. A few notable results are worth summarizing. The TNE model can produce a condensation regardless of loop geometry. However, the stability of the condensation varies greatly. Given strong heating and a shallow dip, condensations can be displaced from the dip and will fall to the chromosphere. These loops typically undergo cycles of condensations given a constant heating. Loops with strongly asymmetric geometries or strongly asymmetric heating exhibit condensations which oscillate about the dip. The physics of these oscillations is detailed in Luna et al. [2012a]. These papers focused on advancing the theory of TNE. In our work, we conduct the first systematic study to address if TNE is observed in the real corona.

4.1.1 Numerical Scheme

The TNE model solutions described here were calculated using the ARGOS loop code. ARGOS is a finite-volume solver which uses a second-order Godunov scheme to conserve mass, momentum, and energy [Antiochos et al., 1999]. It solves the one-dimensional hydrodynamic equations:

$$\frac{\partial}{\partial t}\rho + \frac{\partial}{\partial s}\rho v = 0 \tag{4.1}$$

$$\frac{\partial}{\partial t}\rho v + \frac{\partial}{\partial s}\left(\rho v^2 + p\right) = -\rho g \tag{4.2}$$

$$\frac{\partial}{\partial t}U + \frac{\partial}{\partial s}Uv - \frac{\partial}{\partial s}\kappa T^{5/2}\frac{\partial}{\partial s}T = -p\frac{\partial}{\partial s}v + E - n^2\Lambda \tag{4.3}$$

where ρ is the mass density,s is the loop position, v is the velocity, g is gravitational acceleration, is the thermal conductivity, E is the heat input, and Λ is the radiative loss function. The pressure is defined $p = 2nkT$, and the internal energy is defined $U = 3p/2$. ARGOS incorporates the PARAMESH [MacNeice et al., 2000] adaptive grid refinement subroutine, which allows to the code to capture the time-dependent location of the transition region (between chromosphere-corona and corona-condensation).

Before we go into details of how the TNE model works, there are a few nuances to the numerics that we must consider. One of the primary shortcoming of the ARGOS loop code is its inability to describe the physical parameters of the condensation. The ARGOS code is a coronal loop code. It can solve the for the evolution of a coronal loop which forms a condensation. It cannot however accurately describe the physics within the condensation. The primary issue is the radiative loss function. The radiative loss term in Equation 4.3 is based on the optically thin approximation. The optically thin approximation breaks down when the plasma is cool enough to have a less than complete ionization level (He II ionizes around 10^5 K) and dense enough such that the photon mean free path is less than the collisional mean free path. Due to this process, the optically thin approximation loses accuracy in between 5×10^4 K and $2{\times}10^4$ K (the peak for Lyα emission). Because ARGOS does not capture this physics, the code puts a hard boundary on the temperature: it cannot decrease below 3×10^4 K. To maintain the stability of the code, the heating rate in these regions is artificially set to equal the radiative losses. What does this alteration mean for the model results? The strongest effect will be on calculations of the dynamics of the prominence. The growth rate for the condensation is set by the pressure gradient in corona and is physically accurate. The distribution of mass within the condensation is based on non-self-consistent energy balance and is not physically accurate. This numerical trick is also present at the loop foot points. For the TNE model to operate, there must be a reservoir of mass at the model boundary, which can be

redistributed into the corona after the base heating is turned on. Whereas it is often construed as a "chromospheric evaporation", the process would be more effectively described as "chromospheric siphoning". Evaporation implies a phase transition, which cannot occur given the above method of chromospheric heating. It is the relative increase in pressure in the loop foot points relative to the loop mid point that drive mass redistribution.

The ARGOS code is based on a single fluid approximation for coronal plasma. This assumption reduces the physics of a kinetic, multi-species plasma to single variables describing the density temperature, and velocity of the plasma. This reduction is justified by the dominant timescales of the system. The single fluid model requires that the ion and electron energy distributions are Maxwellian and that the characteristic temperature of these distributions are equal. Collisions drive the equilibration of these quantities; electron-electron and ion-ion collisions set the Maxwellian relaxation time and electron-ion collisions set the thermal equilibration time.

The collision frequency of these process may be calculated using transport theory. The Fokker-Planck derived frequency for electron-electron collisions is approxmately

$$\nu_{ee} \approx \frac{n_e e^4 \ln \Lambda}{m_e^2 V^3} \tag{4.4}$$

where n_e is the electron density, e is the electron charge, $\ln \Lambda$ is the Coloumb logarithm, m_e is the electron mass, and V is the thermal velocity of the particles [Boyd and Sanderson, 2003]. This is approximately 10^3 s^{-1} in the coronal regime. The rate for ion-ion collisions decreases due the increased mass, and the rate is approximately 10 s^{-1}. The exchange of energy between electrons and ions is a more elastic process, which results in a slower thermalization rate approximately, 10^{-1} s^{-1}. All of these timescales are fast relative to the characteristic timescale for the evolution of the thermodynamic evolution coronal plasma. In the context of the single fluid hydrodynamic model, we can compare these rates to the cooling rate of the corona which is approximately 10^{-4} s^{-1}.

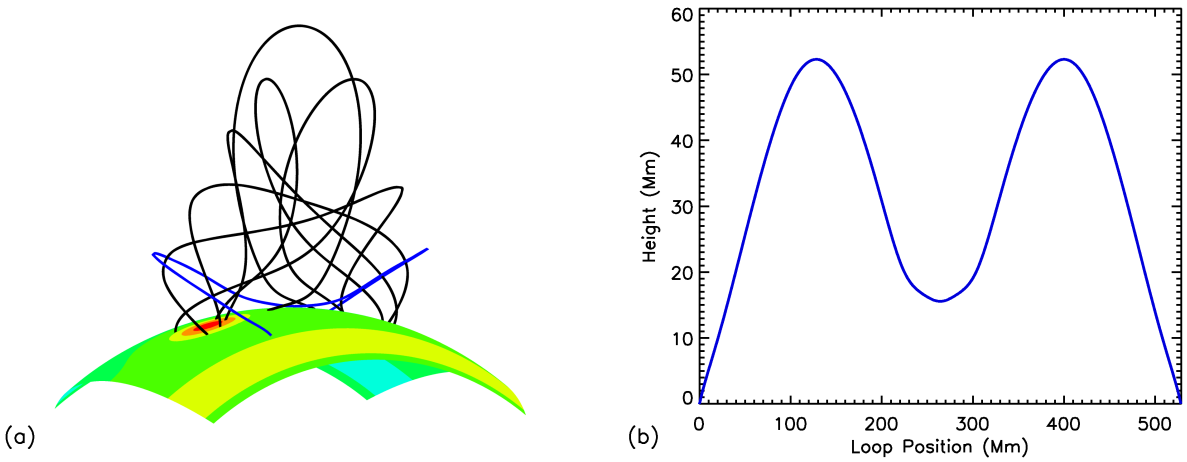

Figure 4.1 (a) A symmetric dipped field line extracted from the flux rope model. (b) The geometry of the loop as it is used in the ARGOS hydrodynamic code.

4.1.2 Driving the Model

The TNE model specifically describes a methodology whereby a equilibrium coronal loop is driven radiatively unstable by excessively heating the foot points. The ARGOS loop model allows us to simulate this process through two inputs: loop geometry and heating.

The ARGOS code has been implemented along a number of different field line geometries [Karpen et al., 2001]. It has been found that the TNE can occur regardless of geometry (dipped, undipped, arched, and flat loops). For the purposes of this thesis, we conducted catastrophic cooling experiments on three different loop geometries which where extracted from the Fan and Gibson flux rope model: symmetric dipped, asymmetric flat, and asymmetric dipped (Figure 4.7 shows examples of these geometries). There are two geometric loop properties which come into play in these solutions: the integrated loop length and slope of the loop relative to gravity. Figure 4.1 specifically shows the dipped symmetric field line we will primarily be discussing in this section.

The TNE model deals with a specific empirical form of heating

$$E(s) = E_0 \qquad t < t_0$$

$$E(s) = E_0 + E_1 \cdot \exp\left(-s/\lambda\right)\frac{t - t1}{t_1 - t_0} \quad t_0 < t < t_1$$

$$E(s) = E_0 + E_1 \cdot \exp(-s/\lambda) \qquad t > t_1. \tag{4.5}$$

The model is initiated with a hydrostatic loop heated uniformly. At time t_0 the foot-point heating is turned on and ramped up linearly until t_1 at which point the foot-point heating remains constant.

Physically, foot-point heating is related to heating processes stemming from wave dissipation [Mandrini et al., 2000]. Practically, foot-point heating is an effective mechanism for driving siphon flows in a loop [Antiochos, 1979].

The free parameters in the Equation 4.4 are the uniform heating E_0, the base heating E_1, the scale height λ, and the ramp-up time t_1. Of these parameters, only t_1 does not effect loop evolution. The characteristic time scale for loop evolution is several hours. In the loop examples presented in this chapter, the quantity $(t_1 - t_0)$ is set to 1000s. At time scales shorter than the loop evolution time, the heating ramp up time does not affect the evolution of the loop.

The value E_0 is typically set such the entire coronal loop is held at a temperature above 8×10^5 K. If E_0 is set too low at model initiation, a condensation will form in the loop prior to perturbation. The corona needs a strong enough heat source to exist and not radiate back to chromospheric temperatures as was discussed in section 1.3.2. For loops in the 200-500 Mm range, the uniform heat source is around 10^{-6} erg s^{-1} cm^{-3}. The more uniform heat supplied to a loop, the hotter the loop is.

The base heating and scale terms can have very strong effects on loop evolution. In this work, we have studied loop evolution between with scale heights between 5 Mm and 50 Mm. Considering a dipped loop geometry, if too short a scale height is used, condensations will form directly above the foot point transition region and opposed to near the loop apex or loop dip. In this scenario, both foot points of the loop undergo identical processes without interaction between foot points. These condensations quickly descend back into the chromosphere via gravity, but the formation process is cyclical. This process has been previously discussed in Karpen et al. [2005]. In considering appropriate scale heights, it is useful to consider the work of Aschwanden et al. [2001]. In solving for hydrostatic balance in a variety of half circular loops using a foot-point-heating scheme, the

authors found that a short scale height could lead to a density-inversion in the coronal region of a loop. They suggest that in a dynamical scenario, long loops with a short scale height cannot be stable.

We vary the base heating in our experiments according to the uniform heating, such that the base heat varies between 3 and 100 times the uniform heating. Given a heating scale with varies from 2% to 30% of the loop length, this results in a ratio for total energy deposition (base/uniform) from 1 to 20. In loops which go thermally unstable, the base/uniform ratio generally needs to exceed 3, but this relationship is not linear with variation in scale height.

4.1.3 Cooling Loop Evolution

To present the model solutions, we will be using position-time diagrams as shown in Figure 4.2. The 1D loop position is projected against the time evolution of various quantities. Figure 4.2 shows the loop segment extending from 10 Mm above the chromosphere to 25 Mm past the field line dip (this is the field line shown in Figure 4.1). The field line and the heating are symmetric.

The TNE model begins with a uniformly heated hydrostatic loop. Over the first 1000s of the evolution, the base heat is flipped on. In this model the uniform heating, base heating, and scale height are set to 6×10^{-6} erg cm^{-3} s^{-1}, 5×10^{-4} erg cm^{-3} s^{-1}, and 25 Mm respectively. After the base heating is switched on, it takes approximately 3000s for the energy to get redistributed and the loop to reach its maximum temperature. In this run, the loop temperature peaks at 2.25 MK. Throughout the rise in temperature there is also a net increase in density in the loop. This additional coronal mass is suctioned out of the loop foot points. The ARGOS code makes use of a moving lower boundary, such that when the base heating is turned on, the location of the chromosphere descends lower in the loop by 5 Mm.

The catastrophic cooling phase of the loop begins after the temperature maximum is reached. The monotonically increasing loop density allows the loop to radiate more effectively. Despite the fact that loop top is conductively dominated, the enhanced radiative cooling leads to a net pressure decrease. The decrease in pressure leads to a constant siphon flow of material from the foot points

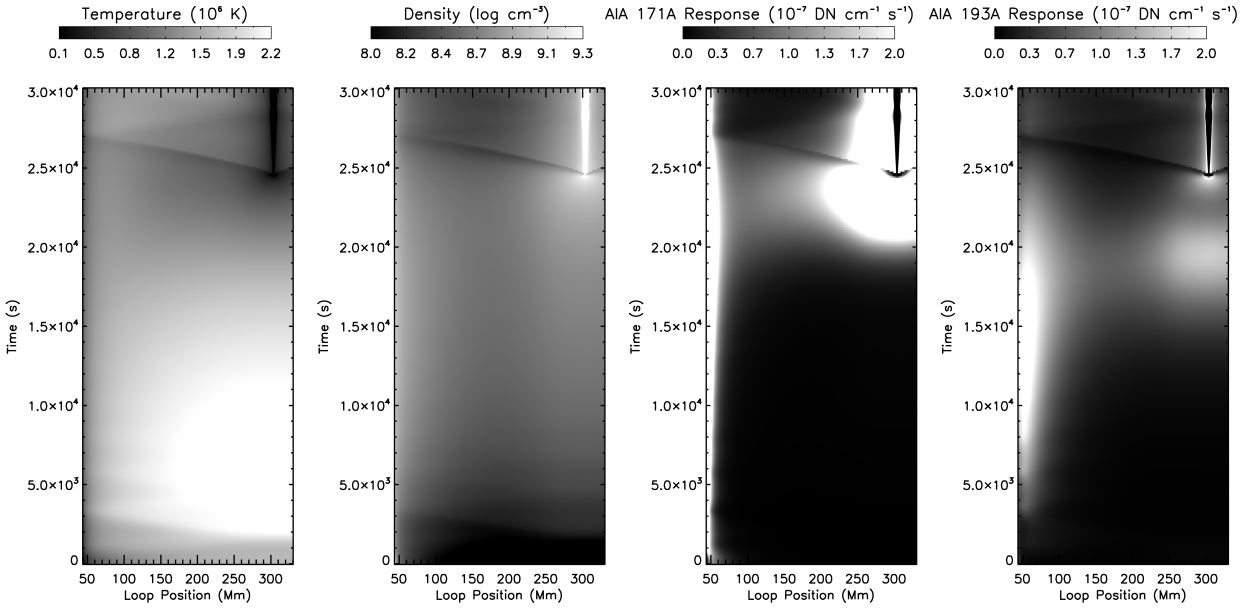

Figure 4.2 The evolution of a catastrophically cooling loop based on the thermal non-equilibrium model of prominence formation. Temperature (a), density (b), predicted emission in SDO/AIA 171Å (c) and 193Å (d) are plotted in grayscale as a function of position along the loop and time.

which further enhances the radiative losses. It is this feedback process which drives catastrophic cooling and the TNE model. Thermal conduction effects are important to the process. Thermal conduction acts diffusively to smooth localized temperature gradients and thus preferably damps high-wave number perturbations which might catastrophically cool [Meerson, 1996]. In this manner, catastrophic cooling must be a full loop process. Figure 4.2b confirms this, as the density increase between 0 and 20000s is isotropic along the loop as is the cooling.

The hypobaric cooling rate grows exponentially, and a condensation is formed at 24500s. The rapid infall of material leads to a shock which propagates from the condensation point towards the base. After the shock traverses the loop, both the temperature and density of the loop oscillate as the loop finds a new equilibrium. The dipped loop now has basically become two separate arched coronal loops, which each have a "foot point" at the dip/condensation. Each loop half can achieve a higher density, higher temperature equilibrium different from the initial condition due the base heating as well as the "half-length" coronal segment. The condensation maintains a lower pressure than the chromospheric foot point, and a siphon flow maintains an approximately constant accretion rate for the condensation.

This description defines the standard process of the TNE models. As mentioned in the preceding section, based on the geometry and heating parameters there are divergent evolutions for loops. In the example of undipped or weakly dipped field lines, a condensation will form and then proceed to accelerate to one or the other foot points. This occurs near the free fall speed so this particular process should not play a role in large-scale, long-duration quiescent prominences. If the total base heating is too high, condensations form near the loop base as opposed to mid-loop. This generally occurs when the total base heat to total uniform heat ratio is ten or above. A third evolutionary branch occurs with weak heating. Weak base heating can create a situation where density is added to the loop, but at a slow enough rate that the loop achieves a high-density, cooler-temperature equilibrium without condensing. In 34 model runs, this result was achieved once with a value of 1.02 for the total base heat to total uniform heat ratio.

4.1.4 Cooling Loop Emission

We have discussed the physical properties of a coronal loop undergoing TNE, but using remote observations, we cannot directly measure those quantities on the Sun. As we discussed in section 1.4, EUV emission contains a convolution of information on the density, temperature, and velocity of the emitting plasma. Thus, to compare the model to the observations we will forward model the observables using the ARGOS loop solutions.

This process was described in some detail in section 2.2. In that diagnostic study, we synthesized three observable quantities: two EUV integrated-line fluxes and the polarization brightness. In this section, we seek to compare our 1D loop model to the dynamic EUV variability structures which were diagnosed in section 3.2. Compared to our previous forward model, this process is complicated by two additional factors. First, the ARGOS loop code is one-dimensional, while the optically-thin EUV corona is inherently 3D. Second, we no longer have spectrally resolved measurements but instead only bandpass images.

The plots for predicted emission (as seen in Figure 4.2c) were made using the 1D model solutions and do not assume any projection effects. Our plots for forward-modeled emission are created in the following process. The temperature is converted in an AIA signal via the instrument temperature-response function. This temperature-response lookup table was produced at Lockheed Martin Astrophysics Laboratory, specifically to model the predicted instrument responses pre-launch. It incorporates the throughput of the optics, the predicted temperature-dependent spectrum of the corona, and the sensitivity of the detectors to photons of different energies. The optics and CCDs are laboratory tested on the ground [Boerner et al., 2012]. The CHIANTI atomic database is used to synthesize the coronal spectrum within the bandpass of each telescope. Each bandpass includes several emission lines which are described in detail in Appendix D. The AIA temperature response function is produced by convolving the CHIANTI spectrum with the AIA laboratory spectral response. The CHIANTI spectrum is based on a constant pressure plasma of abundance from Feldman [1992] and ionization equilibrium from Dere et al. [1997]. It is calculated

in units of erg s^{-1} $Å^{-1}$ cm^{-5}, which is the spectral irradiance per unit emission measure. Emission measures is a conveniently defined quantity for the collisional-excited, optically thin corona

$$EM = \int n^2 d\ell \tag{4.6}$$

Off the solar limb, the emission measure is typically highest at the plane of the sky.

To produce the intensity plots, we interpolate the calculated AIA response function for the temperature and multiply by the square of the density. The units of emission for the 1D models are in DN (data number) s^{-1} cm^{-1} where the distance unit represents the fact that we do not assume a finite line-of-sight width. Figure 4.2c and 4.2d show the emission signatures for the TNE process in the 171Å bandpass and the 193Å bandpass. The cooling process creates enhancements in emission is both bandpasses which occurs throughout the loop. Peak emission in 171Å occurs at time 23000s, and peak emission in 193Å occurs at 19000s. Both of these emission peaks occur before the formation of the condensation, and the relative contrast of these brightenings differ throughout the loop.

4.1.5 Comparing Prominence Horns and the TNE Model

In our observations of prominence-cavity dynamics we were able to probe the interrelation of three AIA bandpasses: 304Å, 171Å, and 193Å. The primary result of the dynamics observations was correlated prominence/condensation and coronal dynamics in prominence horns. These dynamics appeared to be field-line aligned. In this section, we will use the ARGOS hydrodynamic code to see if horn observations are compatible with a catastrophic-cooling scenario for prominence formation.

In order to reduce the complications associated with the multiple free parameters in the TNE model, is this section we will focus on the variation of one variable: base heating. The primary consequence of varying base heat is variation in loop temperature

The TNE model uses an one-dimensional geometry as an input, and we have used a specific dipped field line from the flux rope model as that input. Although, this geometry is unique within the flux rope model, the one-dimension model solution is not unique to that geometry. There are

two field line properties which feed into the ARGOS solution: the slope of the field line relative to gravity and the total field line length, and these two quantities could arise from an infinite set of Cartesian geometries. Thus, we will not focus on the specific appearance of the model solution projected into 3D space as we compare them to the observations of prominence horns. Rather, we will be presenting the model data in ways which illustrate the fundamental observable constraints: the duration of brightenings, the correlation and time-lag between bandpasses, and the spatial scales of the brightenings.

Based on these observational constraints, we present Figures 4.3, 4.4, and 4.5. These plots demonstrate the relationship between 171Å emission, 193Å emission, and the condensation. The plots differ in that they represent three different base heatings, while the scale height (25 Mm), and uniform heating (6×10^{-6} erg s^{-1} cm^{-3}) remain constant. The variation in base heat has two effects on the loop: it changes the maximum temperature of the loop prior to cooling as well as final post-condensation loop temperature. It does not have a strong effect on the cooling time of the loop. The difference in cooling time for a 1 MK (maximum post-condensation temperature) run and 2MK run is approximately 20 minutes (or approximately 15% of the cooling time). The models are plotted such that the condensation forms at $t = 0$.

Figure 4.3 represent a loop with a base heat of 1×10^{-4} erg s^{-1} cm^{-3} and a final maximum post-condensation temperature of 0.8 MK. Figure 4.4 represent a loop with a base heat of 4×10^{-4} erg s^{-1} cm^{-3} and a final maximum post-condensation temperature of 1.2 MK. Figure 4.5 represent a loop with a base heat of 1.6×10^{-3} erg s^{-1} cm^{-3} and a final maximum post-condensation temperature of 2.0 MK.

These position-time plots allow us to demonstrate what relationships are constant in the TNE model regardless of heating and which are variable. The grayscale in both Figure 4.3a and 4.3b presents the emission in 171Å. In Figure 4.3a, the emission has been normalized to emission in the post-condensation equilibrium loop. This serves the same function as a radial vignette in observational data. In Figure 4.3b, the emission has not been normalized because this is the region of the loop which contains the condensation. The 171Å emission from the condensation is four

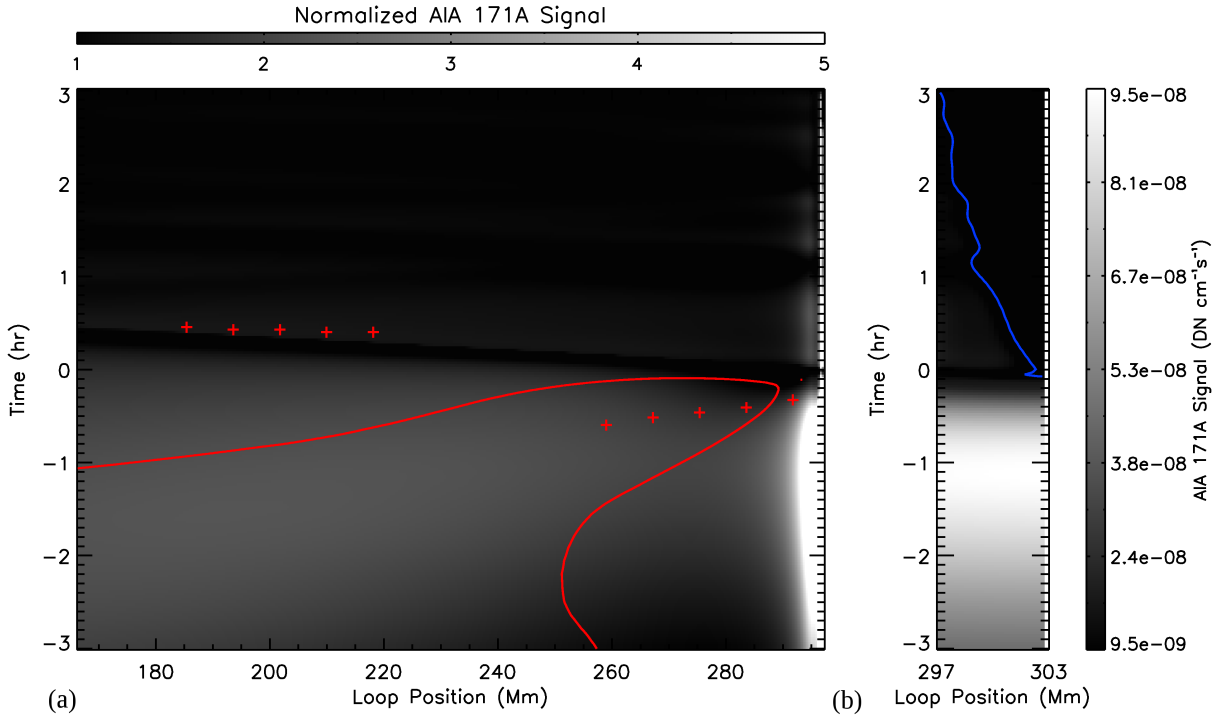

Figure 4.3 Emission structure in a cooling loop. Base heat: 1×10^{-4} erg s^{-1} cm^{-3}. Maximum temperature, post-condensation equilibrium: 0.8 MK. The greyscale indicates the predicted signal for SDO/AIA in the 171Å bandpass. The red contour show the region and time where the predicted 193Å signal is twice the equilibrium signal (red crosses show temporal maxima in the 193Å signal). The blue contour shows the boundary of sub-10^5 K plasma. The dip of the field line is located at s =303 Mm

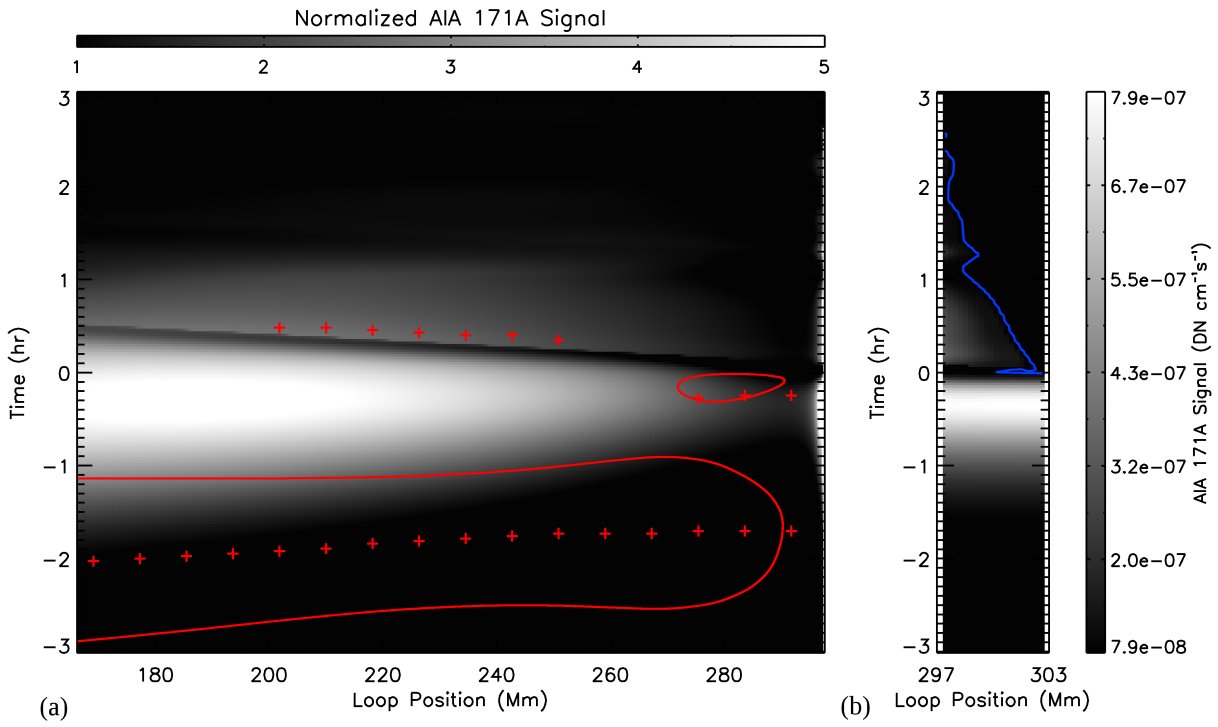

Figure 4.4 Emission structure in a cooling loop. Base heat: 4×10^{-4} erg s^{-1} cm^{-3}. Maximum temperature, post-condensation equilibrium: 1.2 MK. See Figure 4.3 for details.

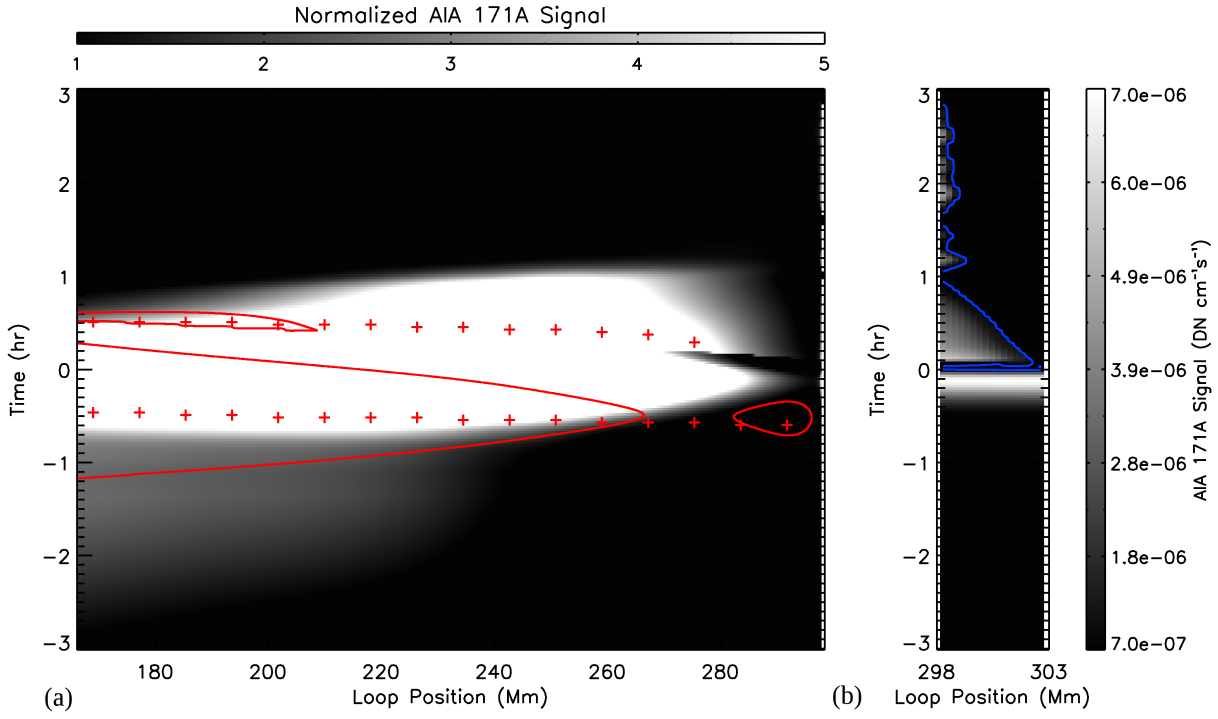

Figure 4.5 Emission structure in a cooling loop. Base heat: 1.6×10^{-3} erg s^{-1} cm^{-3}. Maximum temperature, post-condensation equilibrium: 2.0 MK. See Figure 4.3 for details.

	Horn	0.8 MK	1.2 MK	2.0 MK
171Å Duration	3±0.6hr	5hr	3hr	1.75hr
171Å Peak Brightening	>25	6	18	35
171Å s_{max} [a]	15 Mm	10 Mm	110 Mm	30 Mm
Δt Condensation[b]	+30m	+66m	+20m	+0m
s_{max} Condensation	8 Mm	1 Mm	3 Mm	8 Mm
193Å Peak Brightening	-	5	3	7
193Å Δt	±0.3hr	-2.5hr	-1.7hr	-0.5hr

Table 4.1 Comparison of prominence horns and the thermal non-equilibrium model. The model runs are divided by the post-condensation equilibrium loop temperature maximum. [a]Position along the loop where the brightening reachs maximum. [b]Time lag for the formation of the condensation.

orders of magnitude weaker than the surrounding transition region due to its cool temperature. The spatial scaling of Figure 4.3b is larger than Figure 4.3a. For convenience, Table 4.1 lists the characteristics of each position-time plot.

Figure 4.3, 4.4, and 4.5 all show coherent large scale 171Å brightenings associated with the cooling process. This is a basic prediction of the TNE model. The brightening is caused by the loop plasma cooling into the temperature regime of strong Fe IX emissivity.

While the presence of a 171Å brightening is ubiquitous in the TNE model, the duration of the brightening and its magnitude vary with loop temperature. The 0.8 MK model exhibits a brightening that lasts for 5 hours. The peak magnitude of the brightening occurs within the 10 Mm closest to the condensation and peaks at 6 times brighter than the equilibrium loop. The 1.2 MK model exhibits a brightening that lasts for 3 hours. The peak magnitude of the brightening is 18 times brighter than the equilibrium loop and occurs near the loop apex. The 2.0 Mk model exhibits a 1.75 hour brightening. The peak magnitude is factor of 35 brighter than the equilibrium loop and occurs near the midpoint between the condensation and the loop apex. For comparison, prominence horns were found to last 3.0±0.6 hours with the maximum brightening located 10 Mm plane-of-sky distance from the prominence. The peak brightening for horns was 1.7 times the static emission without considering projection effects. We estimated that the horn would need a density of approximately 5 times the background density to produce the brightening, with correlates with a factor 25 brightening.

Based on the prominence horn observation, we need to assess how the 171Å correlates with He II 304Å emission. In this work, we have not synthesized 304Å emission for several reasons. First, 304Å becomes optically thick in prominence material [Labrosse et al., 2007] which does not allow us to use the optically thin approximation as we did with the coronal lines. Second, as the heating model inside the condensation is not accurate, the predicted condensation emission is not a valid model constraint. In lieu of calculating 304Å emission, we use a temperature threshold to illustrate which regions of the model solution should emit in He II 304Å. We have used 0.1 MK as the threshold, based on the ionization balance of Batalha and de La Reza [1989]. The boundary of this cool plasma is shown as the blue contour in Figure 4.3b, 4.4b, and 4.5b. The condensation rights to the right of the contour.

Figure 4.3, 4.4, and 4.5 all show the formation of the condensation, but these models vary in the extension of the cool plasma as well as the time lag between the formation of the cool plasma and the peak of the 171Å brightening. The 0.8 MK model has the first cool plasma form 1.1 hours after the peak emission in 171Å. The cool plasma extends approximately 1 Mm from the condensation. The 1.2 MK model forms cool plasma 0.3 hours after the peak emission in 171Å. The cool plasma extends 3 Mm from the condensation. The 2.0 MK model forms cool plasma simultaneous with the peak 171Å emission. The cool plasma extends 8 Mm from the condensation. For comparison, we found prominence extensions in horns occurred 0.3±0.1 hours after the peak in 171Å emission. There were significant variations in the range of prominence extensions in horns, from 2 Mm to 25 Mm.

The third observable we consider in Figure 4.3 is the presence of a 193Å brightening. The red contour shows the region where the 193Å emission is a factor of 2 brighter than the equilibrium loop emission. Additionally, red crosses mark regions of local maximum (brightenings which exceed 10% enhancment over the two nearest local minima) in the 193Å light curves.

Figure 4.3, 4.4, and 4.5 all show coherent brightenings in 193Å. There is a variation with temperature in the magnitude of the brightening and the time lag between the peak emission in 193Å and 171Å. The 0.8 MK model brightens in 193Å emission by a factor of 5 at peak, 2.5 hours

before the peak in 171Å emission. The 1.2 MK model brightens in 193Å emission by a factor of 3 at peak, 1.7 hours before the peak in 171Å emission. The 2.0 MK model brightens in 193Å emission by a factor of 7 at peak, 0.5 hours before the peak in 171Å emission. In addition to the strong brightening in 193Å emission associated with the cooling loop, all of the models exhibit a weaker 193Å brightenings associated with the transit of the post-condensation shock. The prominence horn observations indicated that most horns had an associate 193Å brightening. Compare to the observed 171Å brightening, the 193Å brightening was an order of magnitude weaker and spatially smaller. The 193Å brightening varied more widely in duration, and there was not a statistically significant time lag with the 171Å emission.

Figure 4.3, 4.4, and 4.5 have allowed us to describe the temporal differences between emission structures. All the models show coherent brightenings in 171Å and 193Å, but we have not addressed the spatial extent of these observables. The determining factor in which segments of a brightening coronal loop are visible is projection. The observed emission enhancement depends not only on how that loop emits in equilibrium but how the surrounding loops emit in equilibrium.

In an effort to understand this projection effect, Figure 4.6 plots emission as a function of height for two different segments of a 1.5 MK loop undergoing TNE. The black and orange profiles represent the loop segment between the magnetic dip and the loop apex, at the time of peak emission and final equilibrium, respectively. The blue and red profiles represent the loop segment between the loop apex and the foot point, at the time of peak emission and final equilibrium, respectively. The dipped segment is 112 Mm long while spanning 37 Mm in height. The leg segment is 112 Mm long while spanning 51 Mm in height

The dipped segment and the leg segment emit differently. The dipped segment emit more strongly in 171Å and 193Å. There are substantial differences between the 171Å and 193Å profiles. The variation in 171Å emission in stronger. The difference between the weakest emitting segment (leg at equilibrium) and the strongest emitting segment (dip at peak) is a factor of 200. The difference between the same segments but in 193Å emission, is a factor of 4. Figure 4.6 leads us to the following conclusions. The strongest emission signature for TNE occurs 171Å between the

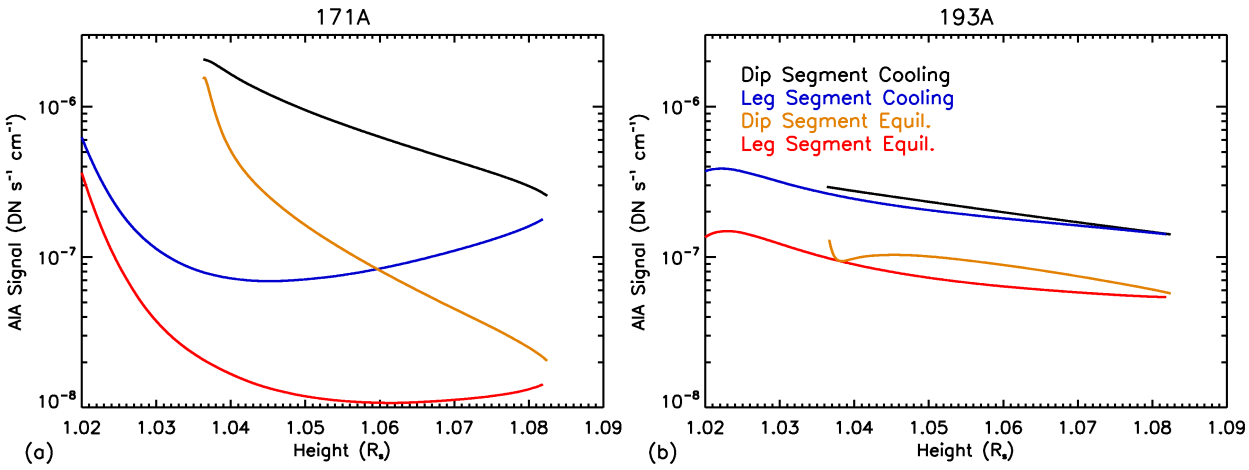

Figure 4.6 Radial profiles for emission is various loop segments. The red and blue profiles show the emission between s=10 Mm and s=122 Mm (see Figure 4.1 for geometry) at equilibrium and peak emission, respectively. The orange and black profiles show the emission between s=259 Mm and s=147 Mm at equilibrium and peak emission, respectively.

region of condensation and the loop apex. TNE produces an inherently weaker signal in 193Å. In our observations of prominence horns, we found very few instances of horn emission which extends through the loop apex. We also found the average 193Å brightening to be significantly weaker than the 171Å brightening.

4.1.6 Conclusions on the Thermal Non-Equilibrium Model

In this section, we have extracted constrained quantities from the TNE model of prominence formation. We have sought to compare the observations of prominence horns to the TNE model. Because the model is one dimensional and the observations are two dimensional, we have used temporal and spectral characteristics to compare the two rather than spatial characteristics which are susceptible to projection effects. Based on our comparison, we find that the TNE is compatible with the strongest observational constraints from prominence horns. These constraints are: brightening structures in 171Å emission which extend for over 30 Mm, last for 3 hours, and occur 30 minutes prior to extensions in prominence material. Given that the TNE model depends on an empirical heating function to drive prominence formation, we have compared several variations on heating to the observations. The observations most closely match a coronal loop with a temperature in the range of 1.0 MK to 1.6 MK. Cooler loops exhibit too long of a duration for the 171Å brightening. Hotter loops exhibit too short of a time lag between the 171Å brightening and the formation of the condensation.

Despite the match between model and data for the primary observables, we find that the 193Å dynamics are not an ideal fit. In the observations, we found a majority of the horns exhibited correlated 171Å and 193Å brightenings. The spatial extent was smaller and the strength of the brightening weaker in 193Å. We found that the duration of the 193Å brightening was similar to the 171Å brightening, although the standard deviation was higher. The TNE model predicts there should be a coherent brightening in 193Å which precedes the 171Å brightening by approximately 1.5 hours. This brightening will not be as strong as the 171Å brightening, relative the equilibrium loop. We suggest that there are two possible reasons for this discrepancy with the

observations. First, there is an observational bias. In analyzing the 193Å light curves (described in section 3.2.3), we looked for local maxima in the temporal vicinity of the 171Å maxima. We attempted to remove this bias by requiring that multiple neighboring slit regions exhibit a similar brightening in 193Å to validate each potential feature. In this way, our observational analysis is more sensitive to weak 193Å emission maxima close to strong maxima in 171Å emission than it is to strong maxima in 193Å temporally-distant from 171Å maximum. Based on this bias, we suggest that the 193Å brightening that we find are closely correlated with the 171Å brightening may be associated with the propagating shock of the condensation. The shock is associated with weaker 193Å maxima as displayed by the red crosses in Figures 4.3, 4.4, and 4.5.

Up to this point, we have compared the TNE model predictions to our dynamic observations of prominence horns. Let us now take a step back and address how the TNE model compares with our static observations of the cavity. The TNE model forms a prominence by initiating the radiative instability. It does this using an energetic perturbation which initially raises the temperature of the coronal loop while steadily increasing the density throughout this loop.

Our static observations of the cavity imply a cavity density which is nearly 40% depleted relative to the streamer. If the TNE process is forming a prominence in the cavity and not the streamer shouldn't the cavity be more dense? The evolution of a cooling loop undergoes multiple phases throughout which the density in the corona is changing. In the TNE model, a uniform heated loop is perturbed with strong foot-point heating. In the models studied here, the density in the coronal segment of loop increases by about a factor of 10 between the initiation of base heat and the formation of the condensation. Immediately after the formation of the condensation, plasma rapidly falls into the condensation reducing the mass in the corona. Over the course of hours a new pressure equilibrium is established in the corona. The corona, in the post-condensation equilibrium, is still a factor of 5 more dense than the hydrostatic uniform heated coronal loop.

Based on this TNE model prediction, prominence horns cannot form the cavity. Based on our observations however, the horns lie inside the cavity. To address this disparity between model and data, we will now introduce a three dimensional model for prominence structure. The flux

rope model will allow us to analyze the projection effects that produce the substructure of the prominence-cavity system. In particular, we ask the question: *how can prominence field lines be related to cavity field lines?*

4.2 The Magnetic Structure of a Flux Rope

In section 4.1, we have described the prominence-cavity structure in terms of one-dimensional dynamics. We have not described how those dynamics project into the three dimensional corona. The three dimensional structure of the prominence-cavity system is described by the magnetic geometry. In this section, we introduce the flux-rope model of the prominence. We will use the 3D geometry of the flux rope to predict the projected structure of hydrostatic and hydrodynamic models of the prominence-cavity system. Through this method, we will show a low density cavity is compatible with the TNE model for prominence formation based on the magnetic geometry of the flux rope.

In section 4.2.1 and 4.2.2, we will discuss the magnetic substructure of the flux rope. In particular, we discuss the distribution of dipped field lines within that structure. By projecting the TNE model onto dipped field lines, we show that the flux-rope model can explain the connection between prominence horns and the cavity. In section 4.2.3, we introduce a hydrostatic model for the flux rope. The axial region of the flux rope is found to be density depleted relative to the surrounding arcade. The hydrostatic model and the hydrodynamic TNE model, when taken in conjunction, can predict both the static and dynamic observations of the prominence-cavity system. Based on the results of section 4.1, we assume that prominence horns are the result of the TNE model occurring along dipped magnetic field lines. Using the magnetic structure of the flux rope model, we find that prominence horns would project throughout the cavity while in three-dimensional space they are limited to a small fraction of the flux rope volume. The density depleted cavity is formed by the interior axial field.

4.2.1 Flux Rope Model

Flux ropes are a universal concept in magnetic fields. In the context of the corona, the Fan and Gibson flux rope is a prominent example. The 3D MHD solution we will be referring to here has already been documented in Gibson and Fan [2006], although we will be analyzing the dataset with a different perspective: we will be identifying the magnetic substructure within the flux rope. We will go on to show that changes in the magnetic geometry results in changes to the thermodynamic properties along that magnetic geometry.

Fan and Gibson model the emergence of an idealized pre-formed flux rope through the photospheric lower boundary of a spherical coronal volume. The model is evolved using an explicit finite difference solver, ZEUS [Stone and Norman, 1992]. ZEUS solves the 3D MHD equations

$$\frac{\partial \rho}{\partial t} + \nabla \cdot (\rho \mathbf{v}) = \mathbf{0} \tag{4.7}$$

$$\rho \left[\frac{\partial \mathbf{v}}{\partial t} + (\mathbf{v} \cdot \nabla)\mathbf{v} \right] = -\nabla p - \rho g \hat{r} + \frac{1}{4\pi}(\nabla \times \mathbf{B}) \times \mathbf{B} + \rho \nu \nabla^{\mathbf{2}} \mathbf{v} \tag{4.8}$$

$$\frac{\partial \mathbf{B}}{\partial t} = \nabla \times (\mathbf{v} \times \mathbf{B}) \tag{4.9}$$

where ρ is density, v is velocity, B is the magnetic field, and p is the pressure. The explicit viscosity term is set relative to the Alfven speed ($v_a = 2 \times 10^3$ km s^{-1}) to 3×10^8 km^{2}s^{-1}. This system is closed using an *isothermal* energy equation for computational simplicity. In the Fan-Gibson model a twisted flux rope is kinematically emerged through the photosphere. The model is evolved through quasi-static (approximately force-free) equilibria, where the flux rope maintains a neutral buoyancy. In this paper, we will be discussing the magnetic structure of this flux rope after the axis of the flux rope has completely emerged, but the flux rope is still in equilibrium with the surrounding arcade. This corresponds with time $70\tau_A$ as shown in Gibson and Fan [2006].

4.2.2 Field Lines in the Flux Rope

The observational studies we have detailed in previous chapters have discussed the unique conditions (low density, strong dynamics) that exist in the cavity. The question we address here is: how do these observational structures relate to the magnetic structure?

To examine the substructure of the flux rope model, we will use magnetic field lines. Field lines follow the relationship:

$$\frac{dx}{B_x} = \frac{dy}{B_y} = \frac{dz}{B_z} \tag{4.10}$$

One of the primary factors in hydrostatic coronal energy balance is field line length. Length (along with temperature maximum and foot point pressure) is one of the three quantities used by Rosner et al. [1978] to define the seminal coronal loop scaling law. Figure 4.7 shows the division of the flux rope structure based on field line length. Strong gradients in length as a function of position within the flux rope structure depict the separation of flux systems.

In this section, we will be discussing the flux systems which comprise the flux rope and arcade. We present these system through example field lines in Figure 4.7. Loop 1 is the red loop which extends from the flux rope base to the arcade boundary. These types of loop are the longest within the flux rope due to there the verticality and twist. Loop 2 is a twisted flat loop. Loop 3 is a twisted, dipped field line. Due to the dip, Loop 2 is long relative to its surrounding field lines.

Loops 1, 2,and 3 are the principle line types which fill the sub-axis flux rope volume. They also form a spatial progression. Loops which lie closest to the flux rope axis are highly asymmetric with a high-arcing apex segment and a low flat segment (corresponding to the left and right segments of Loop 2 in Figure 4.7d). With increasing radial distance from the flux rope axis, the loop apexes reduce in the height while the flat segments expand. There is a geometric transition from the flat asymmetric field lines toward dipped symmetric field lines. One of the important characteristics for Loops 2 and 3 is that their apex segments like along a major topological boundary: the division between the near-potential arcade and the flux rope.

Loop 4 is an axial field line. The current which produces the twist of the flux rope is centered along this line. It is short (low length) given its height, and it is this field line type which fills a bulk of the flux rope volume.

Loops 5 and 6 represent arcade loops. These loops are no longer potential as they were prior to the flux rope emergence. In Loop 5, the loop is now taller due the increase in magnetic energy

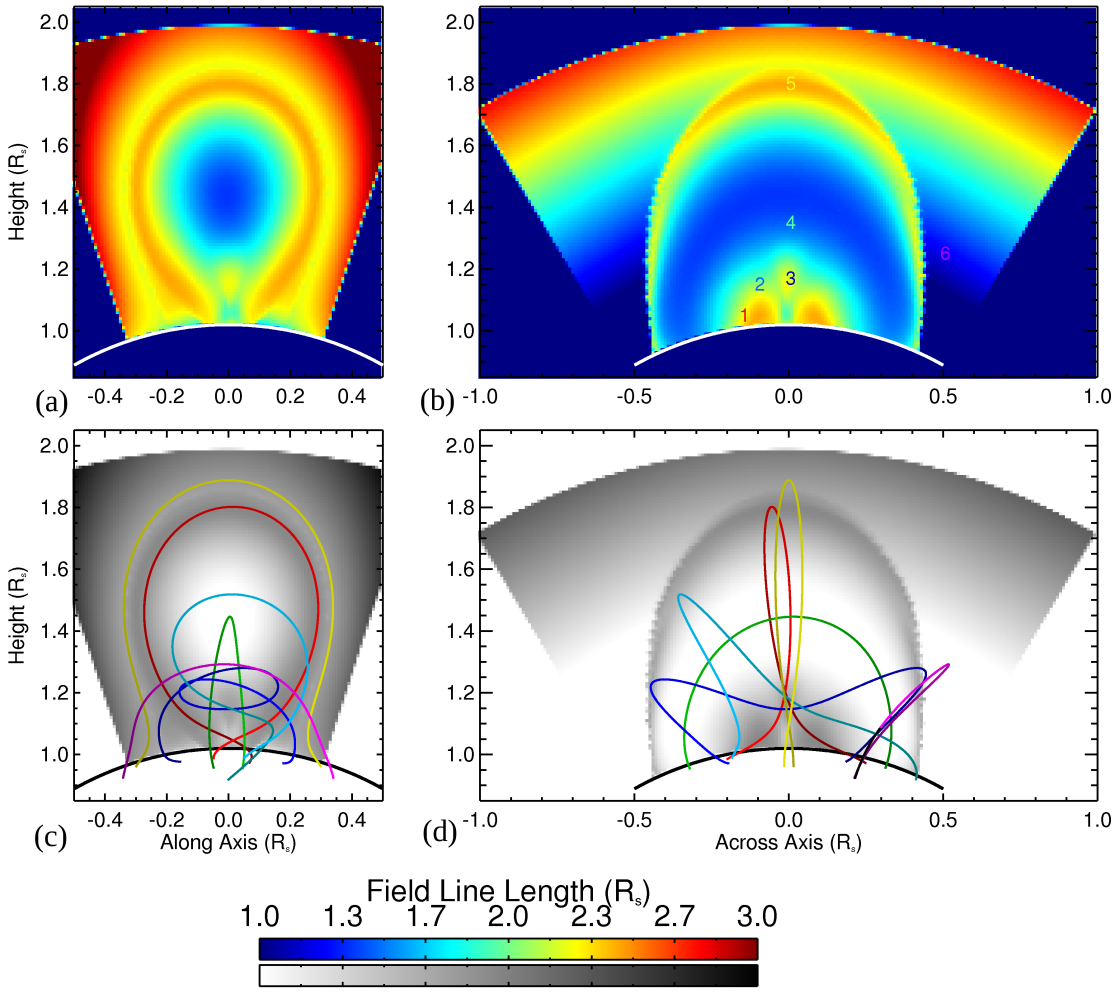

Figure 4.7 Field line length in the flux rope model. Cross section at z=0, looking along the axis (a and c). Cross section at x=0, looking across the axis (b and d). Example field line are plotted (c and d), as color-coded numbers marking where this field lines cross the x=0 plane (b).

underneath the loop. The toroidal flux has pushed Loop 6 normal to the flux rope axis.

These geometries signify the point that the flux rope is not a single, uniform structure. Rather the flux rope can be deconstructed into distinct magnetic geometries. We will go on to demonstrate that these field line geometries and their relative position can play a significant role in determining the observational appearance of a flux rope structure.

4.2.3 Magnetic Dips and Prominence Horns

Now that we have introduced the magnetic substructure of the flux rope, let us return to the question of prominence formation. In section 4.1, we found the TNE model of prominence formation accurately described the emission signatures of prominence horns. Given a flux-rope model for the prominence magnetic field, we ask the question: where would prominence horns occur within the flux rope?

Karpen et al. [2001] showed that a dipped field line geometry is not necessary to form a condensation. Condensations can form on any field line geometry. However, stable condensation need dipped or flat geometries to survive more than a few hours. Based on this result alone we cannot infer that any particular magnetic substructure within the flux rope should be more likely to produce prominence horns than any other. However, one of the primary constraints of prominence horns is that they always *extend from the prominence*. The base of horns lies within the static prominence structure. Both of the cavities displayed in Figure 3.12 exemplify this characteristic. Based on the fact the prominences in Figure 3.12 both existed stably for a minimum of 30 hours, we conclude that the magnetic geometry within these prominences must be dipped. Therefore, we will compare the magnetic geometry of dipped field lines within the flux rope to the geometric structure of prominence horns.

To identify dipped field lines within the flux rope model, we extract 1281 uniformly distributed field lines within the Fan and Gibson data cube.. Two criteria are used to identify dipped field lines: the field line must contain two local maxima (in radial height) which are separated by at least 0.05 R_s (along the field) and the interior minimum must be at least 0.01 R_s lower than both neighboring

maxima. This second criteria is approximately the scale height for prominence material. Of the 1281 field lines, 117 contain dips which meet these criteria.

Gibson et al. [2004] studied the location of dips within the flux rope model. In that work, the authors found that the dipped field region formed a surface in the interior of the flux rope, which they related to the prominence. In our work, we are interested in not only in the prominence but in the coronal connection to the prominence. Figure 4.6 showed that in the TNE model the strongest dynamic emission occurs between the magnetic dip and the loop apex. With this model prediction in mind, Figure 4.8 shows the magnetic-dip-to-loop-apex field line geometries which were extracted from the flux-rope model. These geometries indicate where prominence-forming horns would occur in the flux-rope model.

The 117 dipped field lines have each been divided into two segments. Each segment extends from the dip to one of the neighboring maxima. The loop segments are divided according to which half loop has the high maximum, and are plotted accordingly. The color of the field line depicts the depth of dip relative to shorter maximum. There are several features that are worth noting about these geometries. A majority of the field lines are highly asymmetric, with a high arcing segment and flat, slightly dipped segment. Karpen et al. [2006] predicts that these loops would be the most dynamic, as thermal perturbation to the loop can more easily drive the condensation over the short-side loop apex. The lower segments, pictured in Figure 4.8a, are the segments which would stably hold prominence material. These segment do not extend above the flux rope axis. The segments also grow narrower with height which is a common trait in prominences [see Heinzel et al., 2008].

Prominence horns should occur along both the high and low segments. However, horns which occur along the lower segments would likely be obscured by absorption in the prominence and emission from the steady state condensation-corona transition region. There are structural similarities between the high dipped segments in Figure 4.8b and the horn geometries in Figure 3.12. Both figures show nested loop segments which appear to circumscribe a central axis. The 2011-08-10 horn observations are more ambiguous than the 2011-02-28 observations, due to the

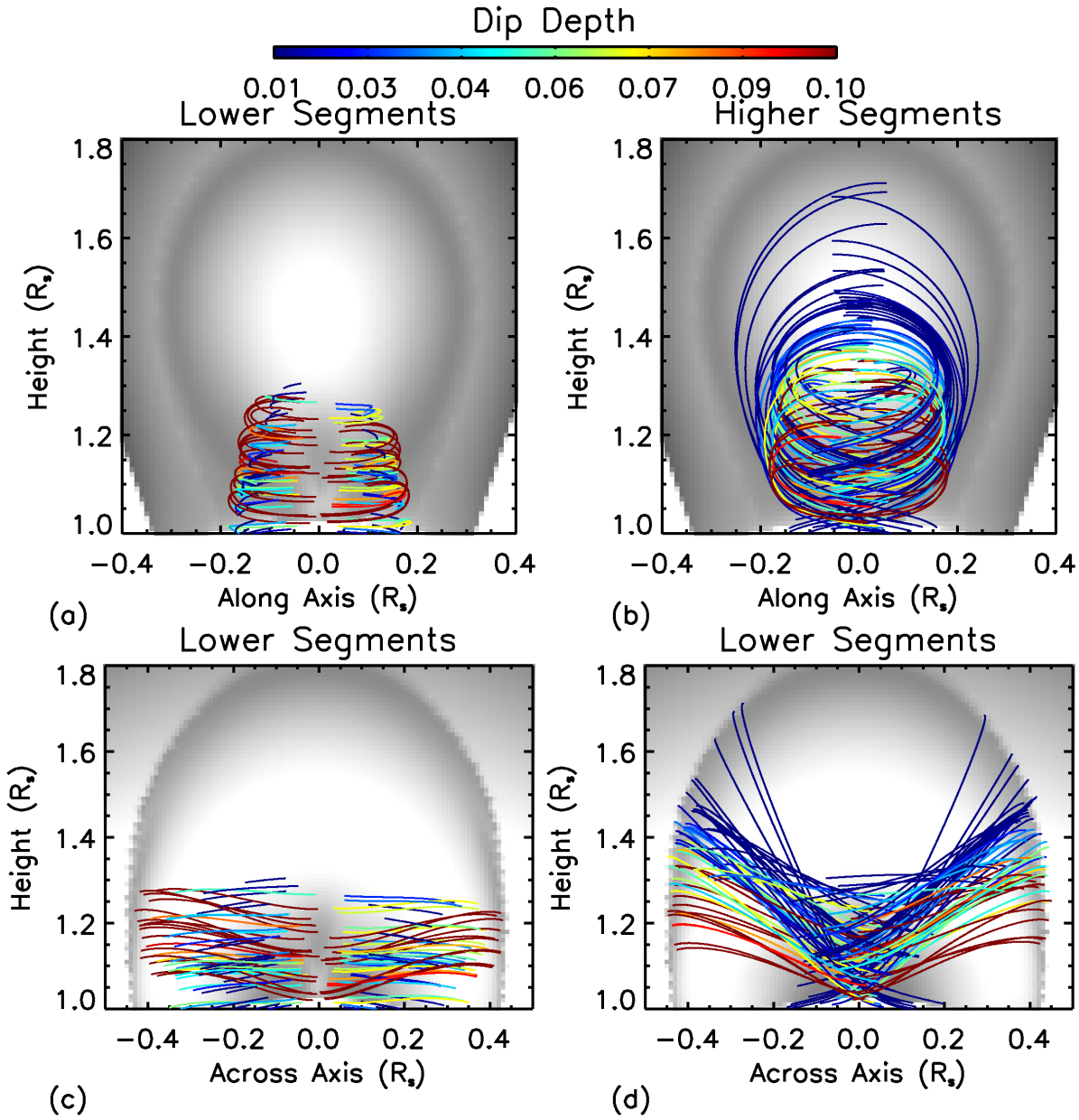

Figure 4.8 Geometry of dipped magnetic field lines in the flux-rope model. Segments are plotted from the dip to the loop apex. The grayscale image shows the field line length on the same color table as Figure 4.7.

angled neutral line. Based on the flux rope model, prominence horns viewed obliquely would be a convolution of structure of Figures 4.8b and 4.8d.

These structural comparisons are inherently qualitative. Given the idealized nature of MHD models and the chaotic nature of the solar atmosphere, we could not expect the model to precisely describe our observations. Rather we look to models to provide insight into the observations. Figure 4.8 demonstrates that the flux rope model is a reasonable interpretation for the projected appearance of prominence horns. Let us now address the original question: how do high density prominence horns occur in the low density cavity? The nested loop segments in Figure 4.8b appear to fill the entire *area* of the cavity. Prominence horns cannot fill the cavity *volume* because based on the TNE model they would produce a high density cavity.

The appearance of Figure 4.8b is produced by projection effects. It is difficult to capture this three dimensional effect in two dimensional plots, but Figure 4.8d provides some insight. The apexes of the dipped field lines occur specifically along the topological boundary between the flux rope and arcade. The upper segments of the dipped field lines form a sheath around the flux rope with an approximate width of $0.1R_s$. In this manner, these field lines make up a relatively small portion of the flux rope volume.

This geometric effect of the flux rope model offers us a solution to problem of prominence horns; Prominence horns are dense, and project throughout the cavity, which is rarefied. If the TNE process of prominence formation only occurs along dipped field lines, the flux rope model predicts that the dynamics would project throughout the cross-sectional area of the flux rope. In three dimensional space however, these dynamics would only occur in the boundary region between the flux rope and the arcade. This description matches our dynamic and static observations of the prominence-cavity system given the following conclusion: the prominence and the density depleted cavity must occur along separate field lines.

The flux rope geometry explains our observation of prominence horns, but it has not identified what structure within the flux rope would form the density depleted cavity. We will now use a hydrostatic model of the flux rope to address how density structure varies along the different

magnetic topologies in the flux rope system.

4.2.4 Hydrostatic Structure of a Flux Rope

The Fan-Gibson flux rope model was originally solved for using a isothermal atmosphere. There is no anisotropic conduction is this approximation. As detailed in section 1.3, the corona is conduction dominated, thus we do not expect the plasma properties within the MHD solution to be accurate.

In order to solve for hydrostatic balance through the flux-rope structure, we use the methodology first used by Vesecky et al. [1979]. The third-order nonlinear ordinary differential equations are solved using a shooting method with an Adams-Bashforth-Moulton integrator [Shampine and Gordon, 1975]. Vesecky et al solves for hydrostatic balance in coronal half loops. Given a geometrically symmetric loop, boundary conditions are easy to define: the temperature at the loop base, the conductive flux at the base, and the conductive flux at the loop apex. The conductive flux at the loop base is set to zero implying that the steep temperature gradient through the transition region is greatly reduced at the optically thick chromosphere. The conductive flux at the loop top is set to zero on the basis of symmetry. The temperature at the chromosphere is set to 3×10^4 K which is approximately where partial ionization and opacity effects become strong. The density at the chromosphere is varied such that the loop-top flux boundary condition is met. Boundary conditions for the flux rope field lines cannot be so neatly defined. Asymmetric field lines cannot be solved as separate halves, otherwise the solution will be discontinuous at the midpoint [Schrijver et al., 2004]. In this work, we numerically integrate from foot point to foot point. However, we now have an asymmetry in the boundary conditions. We cannot dictate the temperature and the temperature gradient at both boundaries; this over specifies the problem. In our solutions, the shooting algorithm varies the near-side foot-point base density until we arrive at a solution where the far-side foot point temperature reaches 3×10^4 K. However, we only regard solutions which have a conductive flux which is decreasing (but necessarily zero) at the foot point as valid.

We have extracted 1281 field lines from the Fan-Gibson dataset and automatedly solved for

hydrostatic balance along these lines. We have used a uniform heating of 2×10^{-6} erg s^{-1} cm^{-3}. This value was chosen so that the shortest field line in the set would have a peak temperature above 8×10^5.

We are interested in the density substructure that is predicted by a hydrostatic flux rope. Figure 4.9a shows the variation of densities through two different lines of sight in the flux rope model as a function of distance from the plane of the sky. The crosses in Figure 4.9 represent a line of sight through the flux rope axis at y=1.4 R_s and x=0. The diamonds in Figure 4.9 represent a line of sight through the arcade at y=1.4 R_s and x=0.35 R_s. The spacing of the densities is irregular due to the nature of the extracted field lines. We have included points that project to within a radius of 0.01 R_s as being in the line of sight.

In hydrostatic balance, we can see that density gradients exist across field lines. For the arcade line of sight, the plane-of-sky density is highest and density monotonically decreases moving out of the plane. This progression is based on the change in height of these field lines. The flux rope has a maximum height in the plane of the sky (as shown in Figure 4.7).

The density profile for the flux-rope line of sight is more complex. Moving out of the plane of the sky, the density varies little. The variation in density is related to the variation in field line length. The line of sight encounters more twisted field farther from the plane. There is a spike is density between 0.35 and 0.45 R_s. This area corresponds with the dipped, highly twisted field, represented as the green loop in Figure 4.7b and 4.7c. These field lines are actually density-enhanced compared to the arcade at that plane of sky position. Past a plane of sky distance of 0.45 R_s, the field geometry is arcade, and the axial and arcade lines of sight are similar.

Based on this hydrostatic approximation there are a few key points to take away. First, the flux-rope model predicts a density-depleted substructure at the center of the flux rope. The density depletion is approximately 35% relative to the arcade and is related to the axial field, not the dipped field. In the hydrostatic model, this depletion is related to the change in field line length and height between the largely-vertical arcade and the short (in length and height) flux rope axis. We suggest that this structure represents the cavity in the flux-rope model.

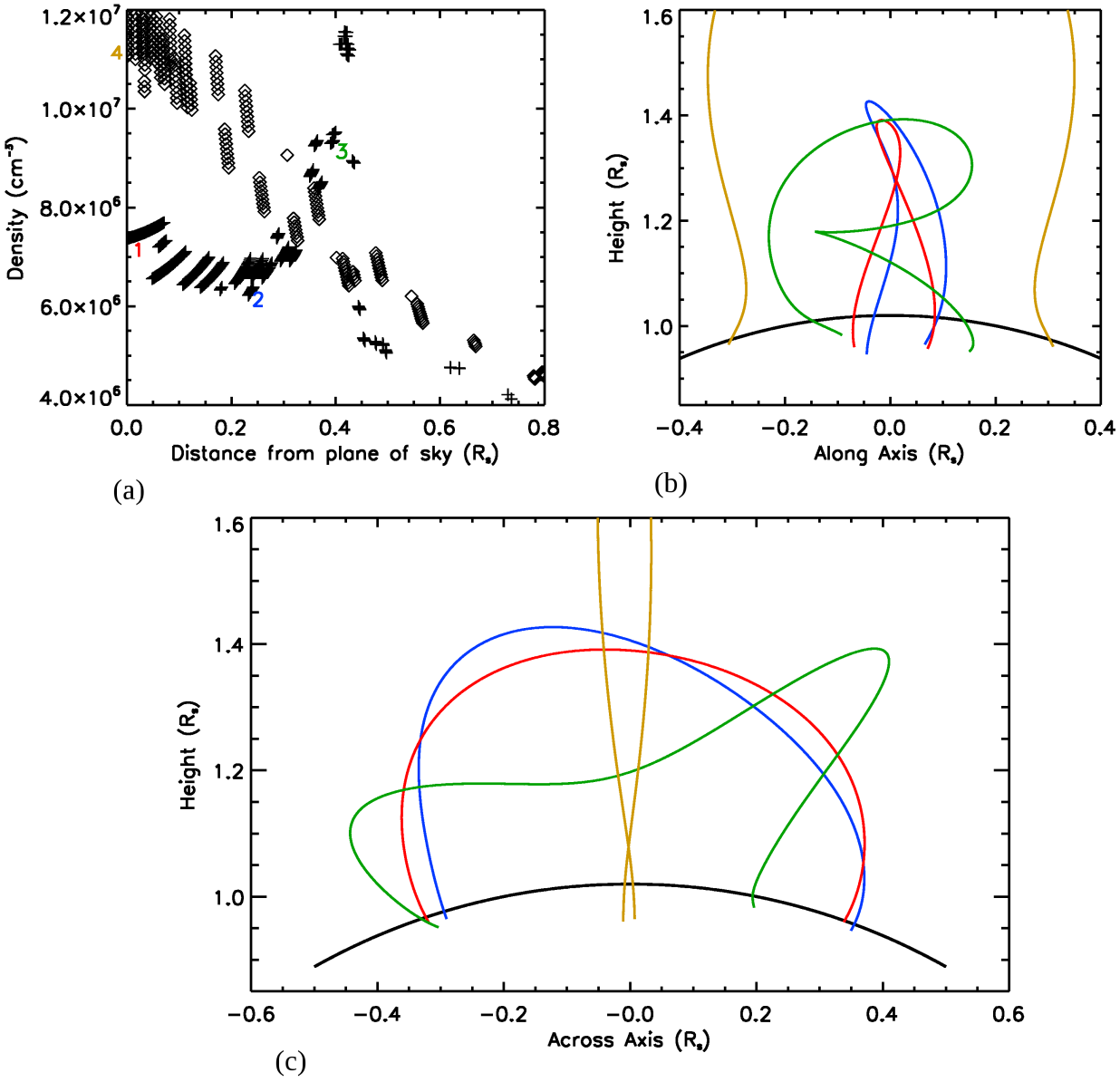

Figure 4.9 The line of sight projection of density through the hydrostatic flux rope and arcade. Crosses display the flux rope line of sight (x=0, y=1.4 R_s), diamonds display the arcade line of sight (x=0.35 R_s, y=1.4 R_s (a). Color coded number in (a) refer to the loop geometries in (b) and (c).

Second, the density solutions illustrate the relatively abrupt increase in field line length near the outer boundary of the flux rope. This distribution is not a product of the initial conditions, which specify a smoothly varying twist profile inside the pre-emerged flux rope.

There are several caveats to consider for the hydrostatic model. First, we use a uniform heating modeling which is universally stable for all loop geometries. Observational studies have shown foot-point-heated loops are a closer approximation to real corona. As was discussed in section 4.1, foot-point heating is not necessarily stable for all loops, thus we have not implemented this heating method. Second, the hydrostatic solutions are found by varying the base density of the loop. This approach is less than satisfying as we do not see strong coronal/chromospheric structural coherence in the real corona. If the arcade has denser foot points than the flux rope, we should be able to define the flux-rope foot points by observing the chromosphere. This is not the case, as the chromosphere does not exhibit that structure. However, the transition region is *the only heat-sink* for the corona. The density of the transition region, for that reason, must exhibit a delicate balance of supporting the mass of the corona and radiating away its excess energy. For this reason, the hydrostatic solutions have physical merit. A final consideration for the hydrostatic solutions is that they are not inherently self consistent. As pointed out in Low and Hundhausen [1995], pressure gradients across field lines will result in non-force-free currents, which are perturbations to the force-free magnetostatic state.

4.3 Conclusions

In this chapter, we have introduced the concept of a coronal flux rope as a large-scale magnetic structure with embedded topologically-distinct substructure. We have used two 1D models to compare our static and dynamic observations of the prominence-cavity system to the energetics of coronal loops. We have found that the large-scale brightenings observed in the cavity in the SDO/AIA datasets are compatible with the thermal non-equilibrium model for prominence formation. The prediction of the TNE model dictates that these actively-condensing field lines should be denser than stable loops. In this way, the TNE model is not compatible with our diagnosis of

the static cavity: the cavity should be 20% to 50% density reduced from the streamer.

We extend this analysis to incorporate the 3D geometry of the flux rope model for prominence structure. We find that the geometry of the dipped field lines is such that they sheath the axis of the flux rope. If the TNE model was active in a flux rope geometry, the appearance would match the structural layout of the prominence horns. To explain the density-depleted cavity, we apply a hydrostatic model to the 3D structure of the flux rope and find that it there is a large-scale density depletion within the flux rope. This density-depleted structure is formed along the axial structure within the flux rope core. The depletion is related to the stature and length of these field lines relative to the surrounding arcade field lines.

Chapter 5

Conclusions

This dissertation has worked toward addressing the question: how does the prominence connect to the cavity? A dynamical and energetic connection between these structures implies that they occur simultaneously along shared magnetic field lines. Thus the question can be reduced to: can an individual magnetic field line contain both a condensation and coronal plasma which is density-depleted relative to the surrounding corona? We have used a hydrodynamic model for a catastrophic cooling process to calculate the time-dependent density along a magnetic field line pre- and post-condensation. Catastrophic cooling is initiated by a slow stagnating bulk flow from the chromosphere. This density addition is isotropic along the field line. Upon the formation of a condensation, some of this added mass falls into the condensation, but approximately half of the originally-chromospheric mass remains distributed within the coronal plasma which surrounds the condensation. This result of the hydrodynamic model immediately allows use to address the primary question of this dissertation. A condensation-holding field line cannot also contain a density depleted coronal region.

Our observational diagnostic allows us to add detail to this hydrodynamic result. We have used the SDO/AIA dataset to show that the prominence-cavity system is characterized by strong variability in EUV emission. These intensity variations are caused by changes in density and temperature, and it does not appear as if the energetic source of the emission variability is active in the streamer. There are several characteristics of the dynamic prominence-cavity emission which provide us insight into the energetics of the system. We find that there are strong correlations

between the dynamic emission from the prominence and dynamic coronal emission which appears to extend into the lower cavity. The temporal and spatial characteristics of prominence horns imply that they are field-aligned structures. To summarize these observational results: we observe dynamic and correlated emission which spans both prominence and coronal temperatures and appears to structurally link the prominence and the cavity. These observational results are at odds with our hydrodynamic results, which suggest that there cannot be a direct magnetic link between the prominence and the cavity.

In comparing the observations to the hydrodynamic model, we have to consider an additional effect: the projection of the three dimensional corona into a two dimensional EUV image. The corona is optically thin the EUV so that when we observe off-limb we are observing the projection of many magnetic structures along the line of sight. Thus to directly compare the spatial characteristics of the cavity observations to the hydrodynamic one-dimensional model, we project the hydrodynamic model onto the three-dimensional magnetic structure of a flux rope. The flux rope is a MHD model which predicts that twisted magnetic field lines support condensed prominence mass. Specifically, we project the hydrodynamic model onto dipped magnetic field lines in the flux rope and find structural similarities with our observations. The dipped segments of these field lines, which would hold prominence plasma, form a slab-like structure when viewed down the axis of the flux rope. These field lines also contain regions of high-density coronal plasma which extend from photosphere to the apex of the flux rope. When viewed down the axis of the flux rope, these coronal segments project throughout the entire cross section of the flux rope. In three dimensions however, these segments are do not make up a majority of the flux rope volume, which is dominated by axial, undipped field lines. The coronal segments of dipped field lines are isolated to the topological surface which divides the flux rope from the surrounding arcade. The projection of these dipped field lines offer us an explanation for the observations. The field lines which can stably hold prominence material project into the core of the flux rope without comprising a significant volume of the flux rope. The bulk of the flux rope volume must be the source of the density-depleted cavity.

Based on hydrostatic balance, we are able to calculate plasma density throughout the flux rope structure. The flux rope is composed of many different magnetic geometries. Field lines of different arc lengths and heights will have different density profiles as a function of height due to the energy and momentum balance in hydrostatic equilibrium. We find that the low-length, low-height field lines with fill the interior of the flux rope are density-depleted by 40% relative to the surrounding arcade. Based on these hydrostatic models, the density-depleted cavity is formed by the short field lines on the flux rope interior. To understand the complete role of projection effects in the EUV observations, we must consider the hydrodynamic and hydrostatic model in unison. The cavity is formed on the flux rope interior along undipped field lines. These undipped field lines are circumscribed by dipped field lines on which prominences can form. The projection of the coronal segments of the dipped field lines is inside the cavity even though those field lines do not form the cavity.

Let us return to the original question and elaborate on how these disparate results fit as a whole. How is the cavity connected to prominence? Based on the hydrodynamic model, the prominence must form along density-enhanced field lines. Therefore, the cavity and the prominence cannot occur along the same field lines. However, the SDO/AIA observation indicate that there are correlated prominence-corona dynamics which appear to be both field-aligned and inside the cavity. By considering the three-dimensional projection effects of the flux rope model, the dynamic observations are explained as separate field lines which surround the cavity but do not contain cavity plasma. The cavity is formed along undipped, short field lines which fill the flux rope interior.

We suggest that there is a connection between cavity field lines and prominence field lines, but the two sets of field lines are mutually exclusive. Those field line sets represent two distinct magnetic substructures within the flux rope model, dipped field and undipped field. One interesting avenue to further explore is how variations in flux rope geometry effect the relative distribution of those field line geometries. However,we must also keep in mind the idealized nature of the Fan and Gibson flux rope. The turbulent velocity field throughout the convection would likely create a

significantly more complex magnetic structure.

The results presented in this dissertation have focused on the combining multiple facets of active prominence physics. The modeling community has focused on either the hydrodynamic models or the MHD models, individually. Current solar MHD codes are not capable using an accurate energy equation due to computational constraints. On the other hand, the hydrodynamic models use a predetermined magnetic geometry. In the densest regions of the prominence, the plasma β may approach unity. In these regions, the plasma will affect the magnetic geometry, and our separation of the force-free equation and the hydrodynamic equation becomes less defensible.

The work we have compiled in this dissertation represents the most comprehensive effort to bridge the theoretical and observational perspectives on the prominence physics. We have conducted a more detailed observational analysis on prominence cavities dynamics than has been attempted before. We have then brought together the magnetic models and the hydrodynamic models to understand those observations. In particular, our treatment of projection effects through both the structural forward model, and the hydrostatic energetic model represents a unique approach coronal observational studies. While projection effects are understood to be troublesome, they are largely ignored for lack of a comprehensive approach to deal with them.

One of the central ideas highlighted in this research is the relationship between magnetic geometry and the thermodynamic properties of the plasma. We have studied this relationship in the context a highly non-potential magnetic structure. However, this approach could be extended to different magnetic structures. How does the distribution of small scale magnetic elements affect the plasma within the quiet sun corona?

Cavities have been a neglected constraint in prominence physics. By incorporating measurements both prominence and cavity observations, this dissertation has shed a new light on the formation and magnetic structure of the prominence and its relationship with the corona.

5.1 Future Work

Our analysis has focused on methods which work around the geometric disparities of the observational and theoretical datasets. Imaging observations are two-dimensional. Coronal loop models are one-dimensional. The magnetic models and the real corona are three-dimensional. Instead of our piecewise approach, the self-consistent way to solve for 3D prominence structure is using radiative MHD models. The model of Gudiksen and Nordlund [2005] is an example which solves the MHD equations with a detailed energy equation through the chromosphere and corona. It has been suggested that the magnetic formation of prominence structure occurs over the course of weeks [Yeates et al., 2007]. Computational limits have capped the Gudiksen et al model at a duration of hours, so the prominence problem is not yet tractable. The work of Zacharias et al. [2011] uses an MHD code which does not solve the energy equation throughout the chromosphere and is much less computationally expensive. This code might provide a means for self-consistently modeling the formation of prominence.

We have observed both flows and emission variations in the prominence-cavity system. These two observations are sensitive to two different spatial geometries, line-of-sight motions and plane-of-sky thermodynamic changes. If we observe a cavity with both methods, we would have tighter constraints on the 3D geometry of prominence horns. The observation of strong flows in horns prior to the 171Å brightening would be consistent with thermal non-equilibrium model. The planning of these coordinated observations are underway.

A new observational dataset should be available by early 2013. The Interface Region Imaging Spectrograph (IRIS) is a Small Explorer class mission designed to simultaneously image and obtain spectra of transition region structure in the ultraviolet. IRIS will have higher throughput than EIS which will allow rapid cadence observations of the prominence horns. Although IRIS will not observe many coronal lines, it will provide us much tighter temperature constraints on the segment of horns between 10^4 K and 10^5 K.

We would like to extend the magnetic model analysis conducted in section 4.2 to other

models for the prominence magnetic field. How does the distribution of magnetic dips change for flux ropes which have a longer axis or wider cross section? This question requires additional model computations. Ideally, we would be able to compare the sheared arcade model and flux rope model through this analysis. To disentangle the fundamental differences between these models would require both modeling groups to initiate their models with similar boundary conditions.

These projects are indicative of the work left to be done on the prominence-cavity system. Our work has fundamentally expanded on the concept of how that system is structured. The cavity and the prominence do not share field lines, but they can be described by a unified structure. There is much work left to be done in understanding the MHD equilibrium of prominences, and further studies in this field will provide us a more detailed perspective on how the solar corona stores and converts magnetic energy.

Bibliography

W. P. Abbett, G. H. Fisher, Y. Fan, and D. J. Bercik. The Dynamic Evolution of Twisted Magnetic Flux Tubes in a Three-dimensional Convecting Flow. II. Turbulent Pumping and the Cohesion of Ω-Loops. Astrophys. Journ., 612:557–575, September 2004.

S. K. Antiochos. The stability of solar coronal loops. Astrophys. Journ. Lett., 232:L125–L129, September 1979.

S. K. Antiochos and J. A. Klimchuk. A model for the formation of solar prominences. Astrophys. Journ., 378:372–377, September 1991. doi: 10.1086/170437.

S. K. Antiochos, R. B. Dahlburg, and J. A. Klimchuk. The magnetic field of solar prominences. Astrophys. Journ. Lett., 420:41, 1994.

S. K. Antiochos, P. J. MacNeice, D. S. Spicer, and J. A. Klimchuk. The dynamic formation of prominence condensations. Astrophys. Journ., 512:985, 1999.

M. Arnaud and J. Raymond. Iron ionization and recombination rates and ionization equilibrium. Astrophys. Journ., 398:394–406, October 1992.

M. J. Aschwanden. A Code for Automated Tracing of Coronal Loops Approaching Visual Perception. Solar Phys., 262:399–423, April 2010. doi: 10.1007/s11207-010-9531-6.

M. J. Aschwanden, T. D. Tarbell, R. W. Nightingale, C. J. Schrijver, A. Title, C. C. Kankelborg, P. Martens, and H. P. Warren. Time Variability of the "Quiet" Sun Observed with TRACE. II. Physical Parameters, Temperature Evolution, and Energetics of Extreme-Ultraviolet Nanoflares. Astrophys. Journ., 535:1047–1065, June 2000. doi: 10.1086/308867.

M. J. Aschwanden, C. J. Schrijver, and D. Alexander. Modeling of Coronal EUV Loops Observed with TRACE. I. Hydrostatic Solutions with Nonuniform Heating. Astrophys. Journ., 550:1036–1050, April 2001.

C. C. Batalha and R. de La Reza. The helium line formation in late-type stars. I - The quiet sun. Monthly Notices of the RAS, 240:23–32, September 1989.

R. M. Batstone, K. Evans, J. H. Parkinson, and K. A. Pounds. Further X-Ray Spectra of Solar Active Regions. Solar Phys., 13:389–400, August 1970.

P. M. Bellan and J. F. Hansen. Laboratory simulations of solar prominence eruptions. Phys. Plasmas, 5:1991, 1998.

T. Berger, P. Testa, A. Hillier, P. Boerner, B. C. Low, K. Shibata, C. Schrijver, T. Tarbell, and A. Title. Magneto-thermal convection in solar prominences. Nature, 472:197–200, April 2011.

D. E. Billings. A guide to the solar corona. Academic Press, New York, 1966.

P. Boerner, C. Edwards, J. Lemen, A. Rausch, C. Schrijver, R. Shine, L. Shing, R. Stern, T. Tarbell, A. Title, C. J. Wolfson, R. Soufli, E. Spiller, E. Gullikson, D. McKenzie, D. Windt, L. Golub, W. Podgorski, P. Testa, and M. Weber. Initial Calibration of the Atmospheric Imaging Assembly (AIA) on the Solar Dynamics Observatory (SDO). Solar Phys., 275:41–66, January 2012.

T. J. M. Boyd and J. J. Sanderson. The Physics of Plasmas. February 2003.

C. M. Brown, U. Feldman, J. F. Seely, C. M. Korendyke, and H. Hara. Wavelengths and Intensities of Spectral Lines in the 171-211 and 245-291 Å Ranges from Five Solar Regions Recorded by the Extreme-Ultraviolet Imaging Spectrometer (EIS) on Hinode. Astrophys. Journ. Supp., 176: 511–535, June 2008. doi: 10.1086/529378.

L. F. Burlaga and R. P. Lepping. The causes of recurrent geomagnetic storms. Planetary and Space Science, 25:1151, 1977.

S. Chapman and T. G. Cowling. The mathematical theory of non-uniform gases. an account of the kinetic theory of viscosity, thermal conduction and diffusion in gases. 1970.

P. Charbonneau. Genetic Algorithms in Astronomy and Astrophysics. Astrophys. Journ. Supp., 101:309–+, December 1995. doi: 10.1086/192242.

G. S. Choe and L. C. Lee. Formation of solar prominences by photospheric shearing motions. Solar Phys., 138:291–329, April 1992. doi: 10.1007/BF00151917.

I. J. D. Craig and J. C. Brown. Fundamental limitations of X-ray spectra as diagnostics of plasma temperature structure. Astron. and Astrophys., 49:239–250, June 1976.

I. J. D. Craig, A. N. McClymont, and J. H. Underwood. The Temperature and Density Structure of Active Region Coronal Loops. Astron. and Astrophys., 70:1–+, November 1978.

G. W. Cushman and W. A. Rense. Solar He II /304 A/ and SI XI /303 A/ line profiles. Solar Phys., 58:299–305, July 1978.

R. B. Dahlburg, S. K. Antiochos, and J. A. Klimchuk. Prominence Formation by Localized Heating. Astrophys. Journ., 495:485, March 1998.

G. Del Zanna, B. O'Dwyer, and H. E. Mason. SDO AIA and Hinode EIS observations of "warm" loops. Astron. and Astrophys., 535:A46, November 2011. doi: 10.1051/0004-6361/201117470.

J.-P. Delaboudinière, G. E. Artzner, J. Brunaud, A. H. Gabriel, J. F. Hochedez, F. Millier, X. Y. Song, B. Au, K. P. Dere, R. A. Howard, R. Kreplin, D. J. Michels, J. D. Moses, J. M. Defise, C. Jamar, P. Rochus, J. P. Chauvineau, J. P. Marioge, R. C. Catura, J. R. Lemen, L. Shing, R. A. Stern, J. B. Gurman, W. M. Neupert, A. Maucherat, F. Clette, P. Cugnon, and E. L. van Dessel. EIT: Extreme-Ultraviolet Imaging Telescope for the SOHO Mission. Solar Phys., 162: 291–312, December 1995.

P. Démoulin, C. H. Mandrini, L. Van Driel-Gesztelyi, M. C. Lopez Fuentes, and G. Aulanier. The Magnetic Helicity Injected by Shearing Motions. Solar Phys., 207:87–110, May 2002.

K. P. Dere, K. G. Widing, H. E. Mason, and A. K. Bhatia. XUV electron density diagnostics for solar flares. Astrophys. Journ. Supp., 40:341–364, June 1979.

K. P. Dere, E. Landi, H. E. Mason, B. C. Monsignori Fossi, and P. R. Young. CHIANTI - an atomic database for emission lines. Astron. and Astrophys. Supp., 125:149–173, October 1997. doi: 10.1051/aas:1997368.

J.-F. Donati and A. Collier Cameron. Differential rotation and magnetic polarity patterns on AB Doradus. Monthly Notices of the RAS, 291:1–19, October 1997.

J. B. Dove, S. E. Gibson, L. A. Rachmeler, S. Tomczyk, and P. Judge. A Ring of Polarized Light: Evidence for Twisted Coronal Magnetism in Cavities. Astrophys. Journ. Lett., 731:L1, April 2011.

D. F. Elmore, J. T. Burkepile, J. A.. Darnell, A. R. Lecinski, and A. L. Stanger. Calibration of a ground-based solar coronal polarimeter. Proc. SPIE, 4843:66, 2003.

Y. Fan and S. E. Gibson. Numerical simulations of three-dimensional coronal magnetic fields resulting from the emergence of twisted magnetic flux tubes. Astrophys. Journ., 609:1123, 2004.

U. Feldman. Elemental abundances in the upper solar atmosphere. Physica Scripta, 46:202–220, September 1992. doi: 10.1088/0031-8949/46/3/002.

G. B. Field. Thermal Instability. Astrophys. Journ., 142:531, August 1965. doi: 10.1086/148317.

D. R. Flower. Excitation of the Fe XII spectrum in the solar corona. Astron. and Astrophys., 54: 163–166, January 1977.

J. M. Fontenla, E. H. Avrett, and R. Loeser. Energy balance in the solar transition region. III - Helium emission in hydrostatic, constant-abundance models with diffusion. Astrophys. Journ., 406:319–345, March 1993.

J. Fuller and S. E. Gibson. A Survey of Coronal Cavity Density Profiles. Astrophys. Journ., 700: 1205–1215, August 2009. doi: 10.1088/0004-637X/700/2/1205.

J. Fuller, S. E. Gibson, G. de Toma, and Y. Fan. Observing the unobservable? modeling coronal cavity density. Astrophys. Journ., 2008.

S. E. Gibson and P. Charbonneau. Empirical modeling of the solar corona using genetic algorithms. Journ. of Geophys. Res., 103:14511–14522, July 1998. doi: 10.1029/98JA00676.

S. E. Gibson and Y. Fan. The partial expulsion of a magnetic flux rope. Astrophys. Journ. Lett., 637:65, 2006.

S. E. Gibson, A. Fludra, F. Bagenal, D. Biesecker, G. Del Zanna, and B. Bromage. Solar minimum streamer densities and temperatures using whole sun month coordinated data sets. Journ. Geophys. Res., 104:9691, 1999.

S. E. Gibson, Y. Fan, C. Mandrini, G. Fisher, and P. Demoulin. Observational consequences of a magnetic flux rope emerging into the corona. Astrophys. Journ., 617:600, 2004.

S. E. Gibson, D. Foster, J. Burkepile, G. de Toma, and Stanger A. The calm before the storm: the link between quiescent cavities and cmes. Astrophys. Journ., 641:590, 2006.

S. E. Gibson, T. A. Kucera, D. Rastawicki, J. Dove, G. de Toma, J. Hao, S. Hill, H. S. Hudson, C. Marqué, P. S. McIntosh, L. Rachmeler, K. K. Reeves, B. Schmieder, D. J. Schmit, D. B. Seaton, A. C. Sterling, D. Tripathi, D. R. Williams, and M. Zhang. Three-dimensional Morphology of a Coronal Prominence Cavity. Astrophys. Journ., 724:1133–1146, December 2010. doi: 10.1088/0004-637X/724/2/1133.

J. T. Gosling, J. Birn, and M. Hesse. Three-dimensional magnetic reconnection and the magnetic topology of coronal mass ejection events. Geophys. Res. Lett., 22(9):869, 1995.

B. V. Gudiksen and Å. Nordlund. An Ab Initio Approach to the Solar Coronal Heating Problem. Astrophys. Journ., 618:1020–1030, January 2005.

M. Guhathakurta, A. Fludra, S. E. Gibson, D. Biesecker, and R. Fisher. Physical properties of a coronal hole from a coronal diagnostic spectrometer, Mauna Loa Coronagraph, and LASCO observations during the Whole Sun Month. Journ. Geophys. Res., 104:9801, 1999.

P. Heinzel, B. Schmieder, F. Farnik, P. Schwartz, N. Labrosse, P. Kotrc, U. Anzer, G. Molodij, A. Berlicki, E. E. DeLuca, L. Golub, T. Watanabe, and T. Berger. Hinode, trace, soho and ground-based observations of a quiescent prominence. Astrophys. Journ., 2008.

J. Heyvaerts and E. R. Priest. A self-consistent turbulent model for solar coronal heating. Astrophys. Journ., 390:297–308, May 1992.

A. W. Hood and E. R. Priest. Kink instability of solar coronal loops as the cause of solar flares. Solar Phys., 64:303–321, December 1979.

H. S. Hudson, L. W. Acton, K. A. Harvey, and D. M. McKenzie. A stable filament cavity with a hot core. Astrophys. Journ., 513:83, 1999.

S. W. Kahler. Solar flares and coronal mass ejections. , 30:113–141, 1992.

J. T. Karpen and S. K. Antiochos. Condensation Formation by Impulsive Heating in Prominences. Astrophys. Journ., 676:658–671, March 2008.

J. T. Karpen, S. K. Antiochos, M. Hohensee, and J. A. Klimchuk. Are magnetic dips necessary for prominence formation. Astrophys. Journ., 553:85, 2001.

J. T. Karpen, S. K. Antiochos, J. A. Klimchuk, and P. J.. MacNeice. Constraints on the magnetic field geometry in prominences. Astrophys. Journ., 593:1187, 2003.

J. T. Karpen, S. E. M. Tanner, S. K. Antiochos, and C. R. DeVore. Prominence formation by thermal nonequilibrium in the sheared-arcade model. Astrophys. Journ., 635:1319, 2005.

J. T. Karpen, S. K. Antiochos, and J. A. Klimchuk. The origin of high-speed motions and threads in prominences. Astrophys. Journ., 637:531, 2006.

R. Kippenhahn and A. Schlüter. Eine Theorie der solaren Filamente. Mit 7 Textabbildungen. , 43: 36, 1957.

J. A. Klimchuk. On Solving the Coronal Heating Problem. Solar Phys., 234:41–77, March 2006.

T. A. Kucera, S. E. Gibson, D. J. Schmit, E. Landi, and D. Tripathi. Temperature and Extreme-ultraviolet Intensity in a Coronal Prominence Cavity and Streamer. Astrophys. Journ., 757:73, September 2012.

M. Kuperus and M. A. Raadu. The support of prominences formed in neutral sheets. Astron. and Astrophys.., 31:189, 1974.

N. Labrosse and P. Gouttebroze. Formation of helium spectrum in solar quiescent prominences. Astron. and Astrophys., 380:323–340, December 2001.

N. Labrosse, P. Gouttebroze, and J.-C. Vial. Effect of motions in prominences on the helium resonance lines in the extreme ultraviolet. Astron. and Astrophys., 463:1171–1179, March 2007.

N. Labrosse, B. Schmieder, P. Heinzel, and T. Watanabe. EUV lines observed with EIS/Hinode in a solar prominence. Astron. and Astrophys., 531:A69, July 2011.

M. Landini and B. C. Monsignori Fossi. The X-UV spectrum of thin plasmas. Astron. and Astrophys. Supp., 82:229–260, February 1990.

J. R. Lemen, A. M. Title, D. J. Akin, P. F. Boerner, C. Chou, J. F. Drake, D. W. Duncan, C. G. Edwards, F. M. Friedlaender, G. F. Heyman, N. E. Hurlburt, N. L. Katz, G. D. Kushner, M. Levay, R. W. Lindgren, D. P. Mathur, E. L. McFeaters, S. Mitchell, R. A. Rehse, C. J. Schrijver, L. A. Springer, R. A. Stern, T. D. Tarbell, J.-P. Wuelser, C. J. Wolfson, C. Yanari, J. A. Bookbinder, P. N. Cheimets, D. Caldwell, E. E. Deluca, R. Gates, L. Golub, S. Park, W. A. Podgorski, R. I. Bush, P. H. Scherrer, M. A. Gummin, P. Smith, G. Auker, P. Jerram, P. Pool, R. Soufli, D. L. Windt, S. Beardsley, M. Clapp, J. Lang, and N. Waltham. The Atmospheric Imaging Assembly (AIA) on the Solar Dynamics Observatory (SDO). Solar Phys., 275:17–40, January 2012.

J. L. Leroy, V. Bommier, and S. Sahal-Brechot. New data on the magnetic structure of quiescent prominences. Astron. and Astrophys.., 131:33, 1984.

H. Lin, J. R. Kuhn, and R. Coulter. Coronal Magnetic Field Measurements. Astrophys. Journ. Lett., 613:L177–L180, October 2004.

Roberto Lionello, Zoran Mikic, and Jon A. Linker. Magnetic field topology in prominences. Astrophys. Journ., 581:718, 2002.

D. W. Longcope, G. H. Fisher, and S. Arendt. The Evolution and Fragmentation of Rising Magnetic Flux Tubes. Astrophys. Journ., 464:999, June 1996.

M. C. López Fuentes, J. A. Klimchuk, and C. H. Mandrini. The Temporal Evolution of Coronal Loops Observed by GOES SXI. Astrophys. Journ., 657:1127–1136, March 2007.

B. C. Low and J. R. Hundhausen. Magnetostatic structures of the solar corona. ii. the magnetic topology of quiescent prominences. Astrophys. Journ., 443:818, 1995.

M. Luna, A. J. Díaz, and J. Karpen. The Effects of Magnetic-field Geometry on Longitudinal Oscillations of Solar Prominences. Astrophys. Journ., 757:98, September 2012a.

M. Luna, J. T. Karpen, and C. R. DeVore. Formation and Evolution of a Multi-threaded Solar Prominence. Astrophys. Journ., 746:30, February 2012b.

B. J. Lynch, S. K. Antiochos, P. J. MacNeice, Zurbuchen, Fisk T. H., and L. A. Observable properties of the breakout model for coronal mass ejections. Astrophys. Journ., 617:589, 2004.

P. MacNeice, K. M. Olson, C. Mobarry, R. de Fainchtein, and C. Packer. PARAMESH: A parallel adaptive mesh refinement community toolkit. Computer Physics Communications, 126:330–354, April 2000.

C. H. Mandrini, P. Démoulin, and J. A. Klimchuk. Magnetic Field and Plasma Scaling Laws: Their Implications for Coronal Heating Models. Astrophys. Journ., 530:999–1015, February 2000.

C. B. Markwardt. Non-linear Least-squares Fitting in IDL with MPFIT. In D. A. Bohlender, D. Durand, and P. Dowler, editors, Astronomical Data Analysis Software and Systems XVIII, volume 411 of Astronomical Society of the Pacific Conference Series, page 251, September 2009.

C. Marqué. Radiometric observations of quiescent filament cavities. Astrophys. Journ., 602:1037, 2004.

S. Masuda, T. Kosugi, H. Hara, S. Tsuneta, and Y. Ogawara. A loop-top hard X-ray source in a compact solar flare as evidence for magnetic reconnection. Nature, 371:495–497, October 1994.

P. Mazzotta, G. Mazzitelli, S. Colafrancesco, and N. Vittorio. Ionization balance for optically thin plasmas: Rate coefficients for all atoms and ions of the elements H to NI. Astron. and Astrophys. Supp., 133:403–409, December 1998. doi: 10.1051/aas:1998330.

B. Meerson. Nonlinear dynamics of radiative condensations in optically thin plasmas. Reviews of Modern Physics, 68:215–257, January 1996. doi: 10.1103/RevModPhys.68.215.

F. Q. Orrall and E. J. Schmahl. The prominence-corona interface compared with the chromosphere-corona transition region. Solar Phys., 50:365–381, December 1976.

F. Q. Orrall, G. J. Rottman, R. R. Fisher, and R. H. Munro. The solar coronal density irregularity N squared bar/(n bar) squared derived from simultaneous measurements of the EUV and K-coronal brightness. Astrophys. Journ., 349:656–666, February 1990.

E. N. Parker. Instability of Thermal Fields. Astrophys. Journ., 117:431, May 1953.

E. N. Parker. Topological Dissipation and the Small-Scale Fields in Turbulent Gases. Astrophys. Journ., 174:499, June 1972. doi: 10.1086/151512.

A. I. Poland and J. T. Mariska. A siphon mechanism for supplying prominence mass. Solar Phys., 104:303–312, April 1986.

E. R. Priest, C. R. Foley, J. Heyvaerts, T. D. Arber, D. Mackay, J. L. Culhane, and L. W. Acton. A Method to Determine the Heating Mechanisms of the Solar Corona. Astrophys. Journ., 539: 1002–1022, August 2000.

F. Reale, J. M. McTiernan, and P. Testa. Comparison of Hinode/XRT and RHESSI Detection of Hot Plasma in the Non-Flaring Solar Corona. Astrophys. Journ. Lett., 704:L58–L61, October 2009.

K. K. Reeves, S. E. Gibson, T. A. Kucera, H. S. Hudson, and R. Kano. Thermal Properties of a Solar Coronal Cavity Observed with the X-Ray Telescope on Hinode. Astrophys. Journ., 746: 146, February 2012. doi: 10.1088/0004-637X/746/2/146.

R. Rosner, W. H. Tucker, and G. S. Vaiana. Dynamics of the quiescent solar corona. ApJ, 220: 643–645, March 1978. doi: 10.1086/155949.

P. Rudnick. A Study of the Solar Prominence of July 18, 1933. Astrophys. Journ., 80:377, December 1934.

T. Sakurai. A New Approach to the Force-Free Field and Its Application to the Mag- netic Field of Solar Active Regions. Pub. of the Astron. Soc. Pacific, 31:209–230, 1979.

K. H. Schatten, J. M. Wilcox, and N. F. Ness. A model of interplanetary and coronal magnetic fields. Solar Phys., 6:442–455, March 1969.

D. J. Schmit and S. E. Gibson. Forward Modeling Cavity Density: A Multi-instrument Diagnostic. Astrophys. Journ., 733:1, May 2011.

D. J. Schmit, S. E. Gibson, S. Tomczyk, K. K. Reeves, A. C. Sterling, D. H. Brooks, D. R. Williams, and D. Tripathi. Large-Scale Flows in Prominence Cavities. Astrophys. Journ. Lett., 700:L96–L98, August 2009. doi: 10.1088/0004-637X/700/2/L96.

C. J. Schrijver, A. W. Sandman, M. J. Aschwanden, and M. L. De Rosa. The Coronal Heating Mechanism as Identified by Full-Sun Visualizations. Astrophys. Journ., 615:512–525, November 2004.

S. Serio, G. Peres, G. S. Vaiana, L. Golub, and R. Rosner. Closed coronal structures. II - Generalized hydrostatic model. Astrophys. Journ., 243:288–300, January 1981.

L. Shampine and M. Gordon. Computer Solution of Ordinary Differential Equations: the Initial Value Problem. W. H. Freeman and Co., 1975.

L. Spitzer. Physics of Fully Ionized Gases. 1962.

J. M. Stone and M. L. Norman. Zeus-2d: A radiation magnetohydrodynamics code for astrophysical flows in two space dimensions. ii. the magnetohydrodynamic algorithms and tests. Astrophys. Journ. Supp., 80:791, 1992.

P. J. Storey, G. Del Zanna, H. E. Mason, and C. J. Zeippen. Atomic data from the IRON Project. Astron. and Astrophys., 433:717–730, April 2005. doi: 10.1051/0004-6361:20041771.

S. Tomczyk, G. L. Card, T. Darnell, D. F. Elmore, R. Lull, P. G. Nelson, K. V. Streander, J. Burkepile, R. Casini, and P. G. Judge. An instrument to measure coronal emission line polarization. Solar Phys., 2008. in press.

A. A. van Ballegooijen and P. C. H. Martens. Formation and eruption of solar prominences. Astrophys. Journ., 343:971, 1999.

A. M. Vásquez, R. A. Frazin, and F. Kamalabadi. 3D Temperatures and Densities of the Solar Corona via Multi-Spacecraft EUV Tomography: Analysis of Prominence Cavities. Solar Phys., 256:73–85, May 2009.

J. E. Vernazza, E. H. Avrett, and R. Loeser. Structure of the solar chromosphere. III - Models of the EUV brightness components of the quiet-sun. Astrophys. Journ. Supp., 45:635–725, April 1981.

J. F. Vesecky, S. K. Antiochos, and J. H. Underwood. Numerical modeling of quasi-static coronal loops. I - Uniform energy input. Astrophys. Journ., 233:987–997, November 1979.

J.-C. Vial, H. Ebadi, and A. Ajabshirizadeh. The Ly α and Ly β Profiles in Solar Prominences and Prominence Fine Structure. Solar Phys., 246:327–338, December 2007. doi: 10.1007/s11207-007-9080-9.

N. M. Viall and J. A. Klimchuk. Patterns of Nanoflare Storm Heating Exhibited by an Active Region Observed with Solar Dynamics Observatory/Atmospheric Imaging Assembly. Astrophys. Journ., 738:24, September 2011. doi: 10.1088/0004-637X/738/1/24.

M. Waldmeier. The Structure of the Monochromatic Corona in the Surroundings of Prominences. Solar Phys., 15:167–175, November 1970. doi: 10.1007/BF00149483.

Y.-M. Wang and G. Stenborg. Spinning Motions in Coronal Cavities. Astrophys. Journ. Lett., 719: L181–L184, August 2010. doi: 10.1088/2041-8205/719/2/L181.

L. Woltjer. A Theorem on Force-Free Magnetic Fields. Proceedings of the National Academy of Science, 44:489–491, June 1958.

A. R. Yeates, D. H. Mackay, and A. A. van Ballegooijen. Modelling the Global Solar Corona: Filament Chirality Observations and Surface Simulations. Solar Phys., 245:87–107, September 2007.

P. Zacharias, H. Peter, and S. Bingert. Investigation of mass flows in the transition region and corona in a three-dimensional numerical model approach. Astron. and Astrophys., 531:A97, July 2011.

Y. B. Zel'dovich and Y. P. Raizer. Physics of shock waves and high-temperature hydrodynamic phenomena. 1967.

H. Zirin. The helium chromosphere, coronal holes, and stellar X-rays. Astrophys. Journ. Lett., 199: L63–L66, July 1975.

J. B. Zirker, O. Engvold, and S. F. Martin. Counter-streaming gas flows in solar prominences as evidence for vertical magnetic fields. Nature, 396:440–441, December 1998.

C. Zwaan. On the Appearance of Magnetic Flux in the Solar Photosphere. Solar Phys., 60:213–240, December 1978.

Appendix A

Terms of the Coronal Energy Equation

The coronal energy equation can be written as follows:

$$\frac{3}{2}\left[\frac{Dp}{Dt}+\frac{p}{\rho}\ \frac{D\rho}{Dt}\right]=\alpha\frac{\partial^2}{\partial s^2}T^{7/2}-n^2\Lambda(T)+E(s,t) \tag{A.1}$$

with the operator definition

$$\frac{D}{Dt}=\frac{\partial}{\partial t}+v\frac{\partial}{\partial s}$$

where p is the pressure, t is time, ρ is the mass density, α is the conductivity, s is field line position, T is temperature, n is number density, Λ is the radiative loss function, and E is heat input.

The lefthand side of Equation A.1 represents enthalpy. This includes the advection of thermal energy with bulk flows and the adiabatic relationship between the time-dependent density and pressure. The right hand side of Equation A.1 has terms for thermal conduction, radiative losses, and heating respectively. The conduction term is based on calculations for a fully-ionized, magnetized plasma [Spitzer, 1962]. Under these conditions, thermal conduction is anisotropic and stronger along the magnetic field. The derivation of the thermal conductivity of an ionized gas involve the solution to the kinetic transport equations. Electric fields facilitate electron-ion collisions [Chapman and Cowling, 1970], thus the temperature dependency is derive from two terms

$$F_c=\kappa\frac{dT}{ds}\propto\bar{v}\lambda$$

where F_c is the conductive flux, $\bar{v}$the Boltzmann-averaged velocity ($\approx\sqrt{T_e}$), and λ and the mean free path of electrons ($\approx T_e^2$). To first order, the process is diffusive, however the nonlinearity produces

a more shock-like characteristic to the propagation of the temperature-perturbation [Zel'dovich and Raizer, 1967]. Although, conduction is a diffusive process it is worth while to find a estimated velocity scale. Let us assume that a coronal temperature perturbation is diffused away along a loop, we are interested in the time it takes the temperature increase to propagate along the loop. We start with the equation

$$nk\frac{\partial T}{\partial t} = \frac{\partial}{\partial s}\left(\kappa T^{5/2}\frac{\partial T}{\partial s}\right) \tag{A.2}$$

and the propagation time of thermal perturbation will scale as

$$t = \frac{nkL^2}{\kappa T^{5/2}} \tag{A.3}$$

which leads to a velocity of approximately 1000 km/s, given coronal parameters.

The radiative loss function in Equation A.1 is based on optically thin, collisionally excited emission. This function is both extremely important and debatably constrained. Physically, radiation is the only term to remove energy from the coronal system (in 1D). Conduction and enthalpy act only to redistribute energy. However, calculating the function, $\Lambda(T)$, is no simple task. Ideally, an experimental apparatus could be designed to measure this quantity. However, laboratory experiments have not been able to reproduce high density plasma for long durations to mimic the steady corona [Bellan and Hansen, 1998]. Developing the function from theory requires detailed quantum mechanical calculations for each atomic species present in the corona.. The integrated result of these calculations is shown in Figure A.1, which displays the net energy radiated by a coronal abundance plasma as a function of temperature.

The last term in Equation A.1 is the coronal heating term. Arguably, the biggest issue in solar physics is what heats the corona. Although radially separated by only a few megameters,the corona has a temperature of over 1 MK while the photosphere is only 5600 K. What is the energy source for this drastic change in temperature? The magnetic field must be responsible (as the corona is magnetically dominated), but we cannot observational determine how.

Part of the issue is the relative magnitude of coronal heating. If we compared the amount of energy it takes to heat the corona to the amount of energy leaving the photosphere through

Figure A.1 Radiative loss function calculated by Landini and Monsignori Fossi [1990]. The radiative loss function is based on the integration of all spectral and continuum emission from a coronal abundance plasma at various temperatures.

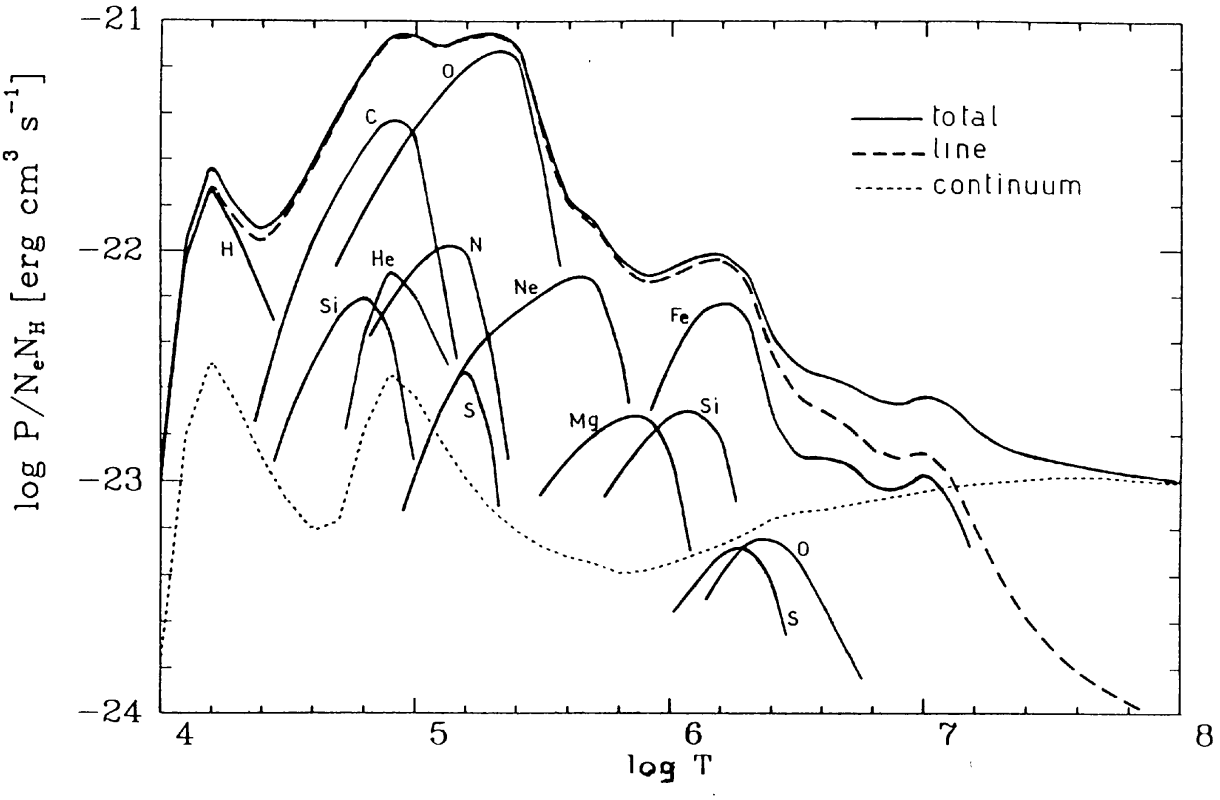

radiation, we have

$$\frac{EL}{F_\odot} = \frac{10^{-5}\ \mathrm{erg\ cm^{-3}\ s^{-1}} \times 10^{10}\ \mathrm{cm}}{10^{10}\ \mathrm{erg\ cm^{-2}\ s^{-1}}} = 10^{-5}$$

where $F_\odot$ is the radiative flux at the photosphere, E is the approximate coronal heating budget, and L is the length of a coronal magnetic loop. The energy budget for the corona is minuscule compared to the radiative flux. A more-telling estimate for corona heating is the kinetic flux density for the photosphere. As described in section 1.2, the corona should be energized by the motions of magnetic foot points in the photosphere. We can estimate this process as

$$\frac{EL}{\bar{m}v^2\nu} = \frac{10^5\ \mathrm{erg\ cm^{-2}\ s^{-1}}}{1\ \mathrm{g\ cm^{-2}} \times (5 \times 10^4\ \mathrm{cm\ s^{-1}})^2 \times 3\ \mathrm{mHz}} = 10^{-2} \tag{A.4}$$

where m is the surface mass density [from Vernazza et al., 1981], v and ν are the characteristic velocity and frequency for granulation. Again,we find that only a small fraction of the photospheric kinetic energy need be converted into thermal energy in the corona.

A great deal of research has gone into the physical definition of the coronal heating term. A detailed description of these processes could fill up a thesis alone, but we will now present some basics of these heating models. The primary consideration in coronal heating models are dissipation mechanisms and transmission mechanisms for magnetic energy. Alfvenic waves carry magnetic perturbations from the photosphere into corona. The main divisions between heating models is if those perturbations are transmitted, stored as magnetic free energy, and dissipated later, or do perturbations dissipate spontaneously. A great deal of micro-physics is necessary to actually dissipate Alfven waves in a near-perfect conductor. Anomalous Ohmic and viscous dissipation can occur in small layers because of resonant or turbulent effects in an anisotropic magnetic field with strong density gradients [Heyvaerts and Priest, 1992, Mandrini et al., 2000]. Magnetic reconnection has also been considered as a dissipation mechanism. Reconnection would tap into the magnetic energy transferred into the non-potential field. The question with reconnection-based heating is what determines how much magnetic energy is built up before it is released.

The observational diagnostics on coronal heating ask question: do loops appear to be heated from the bottom (foot points), top (loop apex), or uniformly. Priest et al. [2000] attempted the

most comprehensive experiment to date to see how the hydrostatic temperature predicted by those heating methods compared to x-ray derived loop temperatures. They found that foot point heating was the most likely. Physically, foot point heating is reasonable given that the theoretically driver of heating must come from the lower solar atmosphere. There is also a strong theoretical precedent [Serio et al., 1981, Aschwanden et al., 2000] for foot point heating as most likely global solution to coronal heating problem. A classic paper illustrating the contrary is Masuda et al. [1994] in which x-ray observations of a flaring loop show isolated 30-50 keV emission from the apex of a loop. This has been attributed to a reconnection event, which produced a M2-flare. M-class flares occur at a rate of about 0.5 per day so this is not a viable heating mechanism for the quiescent corona.

A second aspect of heating models is the timescales for the heating input. Multiple studies have shown that a higher-energy, impulsive heat source more closely reproduces the observed coronal dynamics than a constant, lower-energy source [López Fuentes et al., 2007, Klimchuk, 2006]. The corona, past a frequency limit, does not respond differently. If we consider the equation

$$nk\frac{dT}{dt} = n^2\Lambda(T) \tag{A.5}$$

we can assess the radiative cooling time throughout a coronal loop. We find the cooling rate varies

$$\begin{aligned}\frac{1}{T}\frac{dT}{dt} &= 10^{-3}\text{ Hz (transition region, } < 4\times10^5\text{ K)}\\ &= 10^{-4}\text{ Hz (corona)}\end{aligned}$$

Because of the rapid redistribution by conduction and the relatively slow damping by radiation, impulsive heating with a frequency higher than mHz appears steady.

Appendix B

Line Ratios Diagnostics

Emission lines are produced by the quantum transitions between atomic energy levels. The populations of the energy levels are determined by the thermodynamic properties of the corona. Thus, by comparing the observed fluxes between different emission lines we are able to infer information on the state of the emitting plasma. For the purpose this dissertation, the primary diagnostic ratio discussed is the ratio of FeXII 186.8Å /195.1Å, which is density sensitive. I will illustrate the physical background for ratio diagnostics with a comprehensive discussion of this specific ratio.

The Fe XII 186.8Å/195.1Å ratio was first theoretical identified by Flower [1977] and first applied to the solar corona by Dere et al. [1979]. The easiest way to explain the source of the ratio's density sensitivity is through an examination of the atomic states. The 195.1Å line is one of the more typical lines for coronal emission. The 195.1Å line is produced by the transition between $3s^2 3p^2(^3P)3d\ ^4P_{5/2} - 3s^2 3p^3\ ^4S^o_{3/2}$ (Level 4 and Level 1 in Table B.1). This is an electric-dipole

Table B.1 Notable Electron Levels in the Fe XII atom. This energy distribution of levels is displayed in Figure B.1.

Level	Configuration	Decays to	$A_{ji}(s^{-1})$
7	$3s^2 3p^2(^3P)3d\ ^2F_{5/2}$	3	1.6×10^{11}
6	$3s^2 3p^2(^3P)3d\ ^2F_{3/2}$	2	9.9×10^{10}
5	$3s^2 3p^2(^1D)3d\ ^2D_{5/2}$	2	2.2×10^{9}
4	$3s^2 3p^2(^3P)3d\ ^4P_{5/2}$	1	8.5×10^{10}
3	$3s^2 3p^3\ ^2D^o_{5/2}$	-	-
2	$3s^2 3p^3\ ^2D^o_{3/2}$	-	-
1	$3s^2 3p^3\ ^4S^o_{3/2}$	-	-

Figure B.1 Grotrian diagram for the electron levels of the Fe XII ion. The red transition represent the line blend which forms the Hinode/EIS observed 195.1Å emission line. The blue lines are blended lines at 186.8Å. This line ratio is density sensitive.

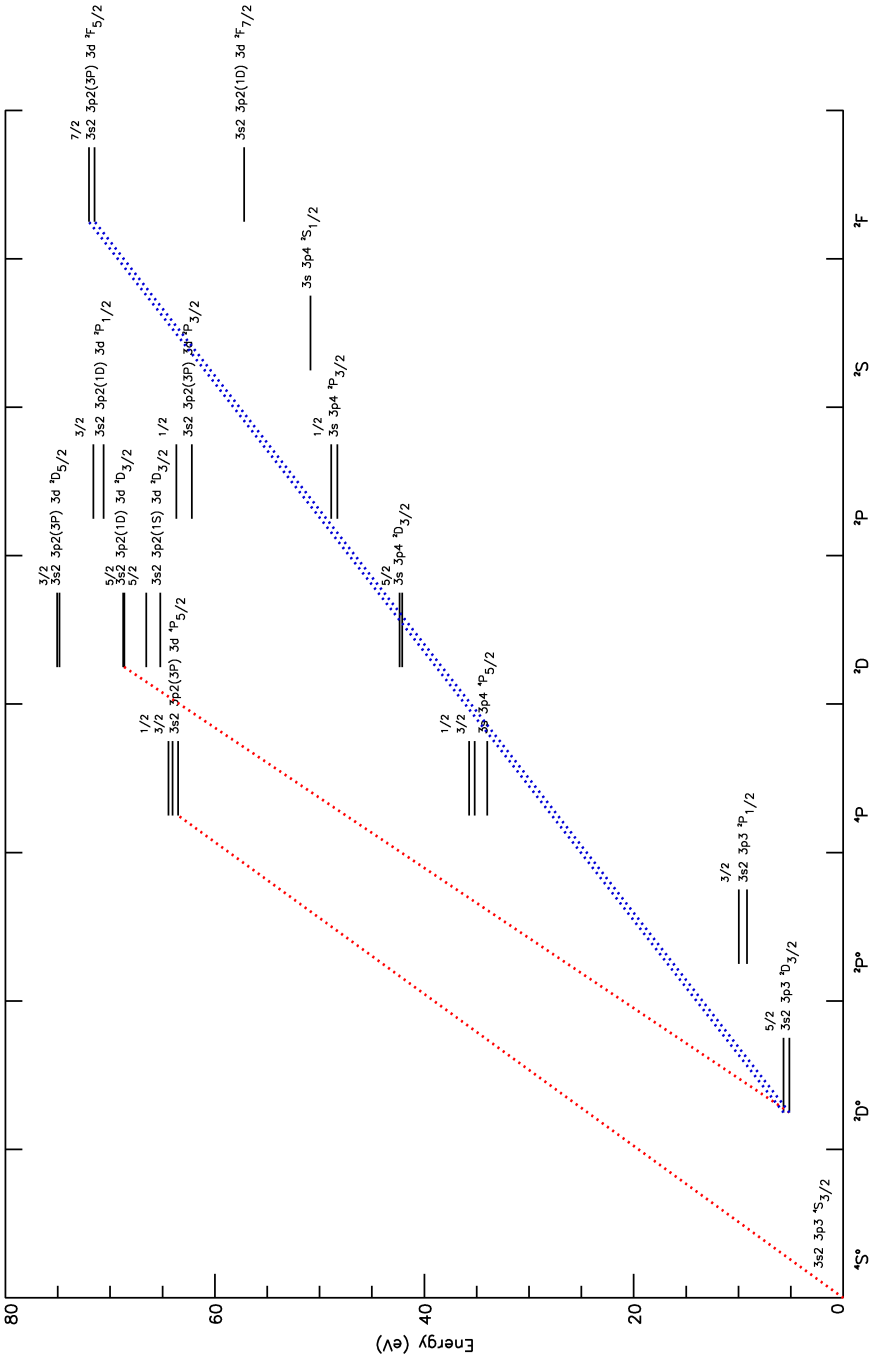

transition ($\Delta S = 0, \Delta L = 1, \Delta J = 1, \pi_u = -\pi_l$) with correspondingly high rate, A_{ji}. Similarly, Level 4 has a strong collision rate from Level 1. The time-dependent population equation for Level 4 can be written:

$$\frac{dn_4}{dt} = n_1 C_{14} - n_4 A_4 1 - n_4 C_{41} \tag{B.1}$$

where n_i is the population in Level i, C_{ij} is the collisional excitation/deexcitation rate between Level i and j, and A_{ji} is the radiative decay Einstein coefficient. This detailed balance is typical of the corona.

The ground level of FeXII is the $3s^2 3p^3\ {}^4S^o_{3/2}$. The first excited level of Fe XII is the $3s^2 3p^3\ {}^2D^o_{3/2}$ (Level 2). Although the principle quantum numbers in Level 1 and 2 are the same, the spin total has decreased ($\Delta S = 1$). Spin-flip collisional excitation does not have a large collision cross section. If we consider the radiative decay between Level 2 and Level 1, we also find that is *forbidden* by parity-change. These two properties result in a disconnect between the Level 1 and Level 2, and this disconnect propagates throughout the populations of the higher levels.

The 186.8Å line is a blend of the transition between $3s^2 3p^2(^3P)3d\ {}^2F_{5/2} - 3s^2 3p^3\ {}^2D^o_{3/2}$ (Level 7-Level 3) and $3s^2 3p^2(^3P)3d\ {}^2F_{7/2} - 3s^2 3p^3\ {}^2D^o_{5/2}$ (Level 6-Level 2). Although, it is possible to populate the fine-structure split Level 6/7 from Level 1, the collision rate is over ten times as strong from the fine structure split Level 2/3. Thus the strength of the 186.8Å line is primarily determined by the populations of Level 2 and Level 3.

Although, the typical coronal balance states that the ground level is the most populous, the unique nature of the FeXII atom makes this a less accurate statement. The split between the Level 2/3 and Level 0 allows a substantial fraction of FeXII to populate Level 2/3. Figure B.2 shows the relative contributions to Level 3 from various processes as a function of density. At low densities, the population is balanced between forbidden radiative transitions to Level 2 and Level 1 and allowed radiative transitions from $3s^2 3p^2(^1D)3d\ {}^4D_{3/2}$ and $3s^2 3p^2(^1S)3d\ {}^4D_{5/2}$. At higher densities, the balance is set by allowed radiative transitions from Level 7 and Level 6 and collisional excitation to $3s^2 3p^3\ {}^2P^o_{3/2}$ and deexcitation to Level 2. The end result of these density dependent

Figure B.2 Important quantities for the Fe XII atom as a function of density. Equilibrium rates into and out of the $^2D_{5/2}$ metastable level (a). Populations in the *L-split* ground configuration of Fe XII (b). The predicted value of the 186.8Å/195.1Å line ratio (c).

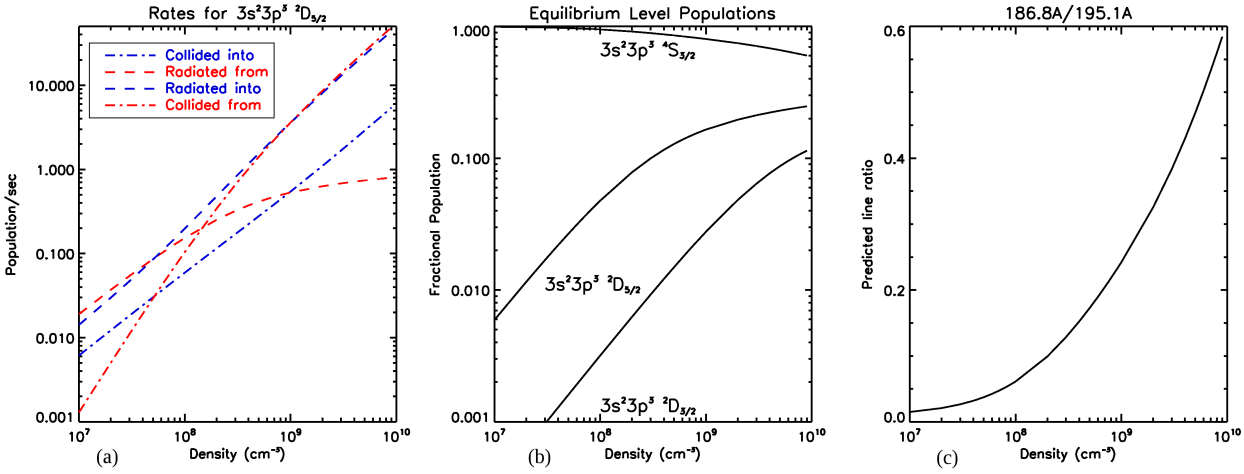

interactions is a strong variation of population with density. The relative populations of Level 1, Level 2, and Level 3 are shown in Figure B.2. The higher energy Level 3 is always more populous than Level 2, below 10^{10} cm^{-3} due to the radiative effects discussed above.

This physics determines the density-sensitivity of the 186.8Å and 195.1Å line ratio. Based on these levels, the observed 186.8Å/195.1Å line ratio (including blends) can be written

$$R = \frac{n_7 A_{73} + n_6 A_{62}}{n_4 A_{41} + n_5 A_{52}}.$$

Appendix C

Spectral Line Fitting

In this dissertation, a few instances of spectrograph data are referenced. The analysis of this data requires fitting the profile of spectral lines. This appendix will describe how this process is undertaken.

Hinode/EIS data

The raw Hinode/EIS data is provided in a three-dimensional "fts" file: two spatial dimensions and a spectral dimension. The value at each point in this 3D array refers to an intensity (in data number) at a particular spatial point at a particular wavelength. Figure C.1 shows an observation of the Fe XIII 202.04Å line using the 2" slit and a 30s exposure. The line profile is fit with a gaussian,

$$I(\lambda) = I_{max} \exp \frac{-(\lambda - \lambda_0)^2}{\sigma^2} + C \tag{C.1}$$

where I_{max} is the peak intensity (in photons), λ_0 is the centroid (in Å), σ is the line width, and C is the background intensity. The errors at each pixel are largely determined by photometric Poisson noise. A χ^2 minimization is done using the MPFIT algorithm [Markwardt, 2009] which uses a gradient-descent technique to find the best fit model. Errors on the model parameters are based on the variation of the χ^2 statistic in the parameter-space surrounding the minimum χ^2 model. The reduced χ^2 for this fit is 1.36.

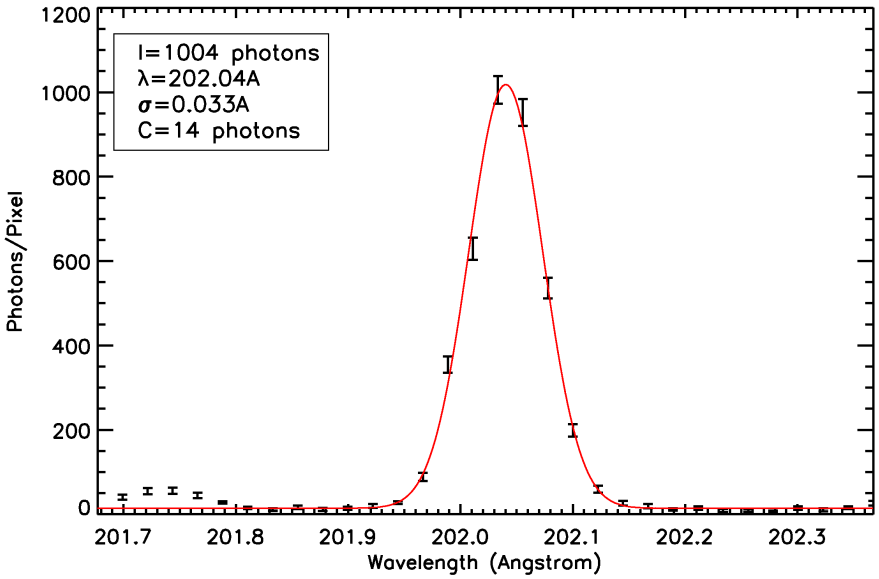

Figure C.1 Observation of the Fe XIII 202.04Å emission line with EIS. The best fit gaussian is plotted in red, and the parameters are shown in the upper left hand side.

Line Width

The observed width of coronal spectral lines have three sources: thermal broadening, instrumental broadening, and nonthermal broadening. These widths are related by

$$\sigma^2 = \sigma_T^2 + \sigma_I^2 + \sigma_D^2 \tag{C.2}$$

where σ is the observed width, σ_T is the thermal width, σ_I is the instrumental width, and σ_D is the nonthermal width.

The thermal width is formed by the random Maxwellian motions of the emitting plasma. It scales with the temperature of the plasma

$$\sigma_T = \frac{\lambda_0}{c}\sqrt{\frac{2kT}{m}} \tag{C.3}$$

where m is the mass of the ion, c is the speed of light, k is the Boltzmann constant, and T is the temperature. For Fe XIII 202Å, this equates to 16mÅ.

The instrumental width stems from the optical design of the system: the number of rulings on the grating and the width of the slit. Using the 2" slit, EIS has an instrumental width of 26mÅ.

Nonthermal broadening occurs because of unresolved mass motions of the plasma. This Fe XIII profile exhibits a nonthermal broadening of 12mÅ. Based on the χ^2 distribution, we find an error on the observed line width of 2mÅ

Doppler Velocity

If the emitting plasma is moving with a net velocity relative to the observer the spectral line will be shifted according to the equation

$$\frac{\lambda_0 - \lambda_L}{\lambda_L} = \frac{v}{c} \tag{C.4}$$

where λ_L is the wavelength of the line at rest. The doppler shift for this spectral profile is 3.5mÅ which corresponds to a velocity of 5 km s^{-1}. Based on instrumental broadening, the CCD pixel size, and the χ^2 distribution, we find a velocity error of 9.6 km s^{-1}. This error can be reduced

by using the 1” slit (less instrumental broadening) and binning pixels (to decrease the photometric errors).

Appendix D

Spectral Contributions to the SDO/AIA EUV Bandpasses

304Å

The 304Å bandpass is centered on the 303.7Å He II resonance-doublet ($2p\ ^2P^o_{3/2} - 1s\ ^2S_{1/2}$, $2p\ ^2P^o_{1/2} - 1s\ ^2S_{1/2}$). Of the emission lines featured by AIA, 304Å is certainly the most complex. The VAL-C atmosphere [Vernazza et al., 1981, Fontenla et al., 1993] predicts that the He II is the dominant helium species in a 15 km thick layer where the temperature rise from 2×10^4 K to 10^5 K with the majority of 304Å generated between 55-75$\times 10^4$K [Batalha and de La Reza, 1989]. The dominant excitation method is believed to electron collisions (in the quiet sun), although recombination maybe also play a role populating the $2p\ ^2P^o_{1/2}$ state [Zirin, 1975]. The 304Å line is optically thick on the solar disk and self-reverses near the solar limb [Cushman and Rense, 1978]. Prominence 304Å profiles have not been observed, but radiative transfer models show that 304Å is optically thick given a prominence slab > 200 km thick and pressure > 0.02 dyne cm^{-2} [Labrosse and Gouttebroze, 2001].

The dominant blends in the 304Å bandpass Si XI 303.3Å and Fe XIII 303.4Å. The SERTS spectrograph provides the most complete measurement of the EUV spectra is this regime. On disk, He II is observed to be 200 times stronger than Si XI, which is the stronger of the two coronal blends (Brosius, 1997). Off limb the ratio is more difficult to define, but the CHIANTI predictions state that 10^{26} cm^{-5} of emission measure at 1.5 MK emits as strongly a megameter thick slab of prominence material (which is on the order of several "prominence threads", while observed prominences appear to contain 10^3-10^4 threads). Prominence emission should dominate coronal

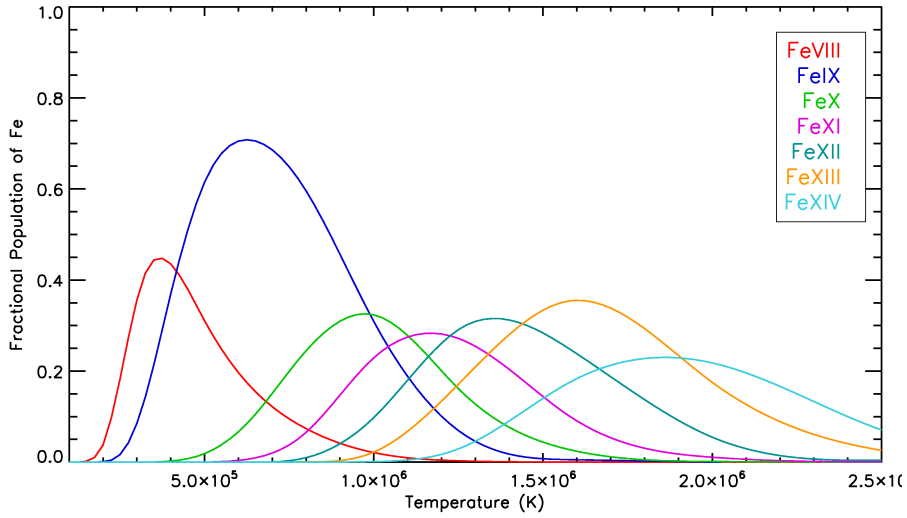

Figure D.1 Populations for iron ion species as a function of temperature. In equilibrium based on Arnaud and Raymond [1992].

emission.

171Å

The 171Å bandpass features multiple blends. The strongest lines in the bandpass are the Fe IX 171.08Å resonance line ($3s^2 3p^5 3d\ ^1P^o_1 - 3s^2 3p^6\ ^1S_0$) and a set of Fe X lines 177.2Å (resonance, $3s^2 3p^4(^3P) 3d\ ^2P_{3/2} - 3s^2 3p^5\ ^2P^o_{3/2}$), 174.5Å ($3s^2 3p^4(^3P) 3d\ ^2P_{3/2} - 3s^2 3p^5\ ^2P^o_{3/2}$), 175.2Å ($3s^2 3p^4(^3P) 3d\ ^2D_{3/2} - 3s^2 3p^5\ ^2P^o_{1/2}$), and 175.5Å ($3s^2 3p^4(^3P) 3d\ ^2P_{1/2} - 3s^2 3p^5\ ^2P^o_{3/2}$). The Hinode/EIS instrument is capable of observing spectral lines to a minimum wavelength of 170Å although the effective area of the telescope is less than 1% of peak at that extreme. Brown et al. [2008] presented a comprehensive EIS spectral list including a number of different observing regions. These spectral observations have been calibrated using pre-launch measurements to convert observed intensities to spectral irradiance measurements. We multiply these measurements by the effective area of the AIA telescopes to produce a predicted observational intensity for AIA and present the data in Tables D.1, D.2, and D.3. Table D.1 shows the relative contributions for the strongest contributing lines at the solar limb for the 171Å bandpass. At the limb, Fe IX is dominant representing over 70% of the AIA

Ion	Line	EIS Intensity[a]	AIA E.A.[b]	AIA Response[c]
Fe IX	171.354	0.54×10^5	3.143	2071
Fe X	174.532	1.20×10^5	0.168	251
Fe X	175.262	0.43×10^5	0.165	89
O VI	173.063	0.06×10^5	1.074	81
Ni XV	176.701	0.29×10^5	0.065	23
O V	172.2	$<0.06\times10^5$ [d]	2.40	<200[d]

Table D.1 Emission line data for the 171Å AIA bandpass.[a]Calibrated EIS data in ergs cm^{-2} s^{-1} sr^{-1} from Brown et al (2009). [b]AIA effective area in cm^2 reported in Boerner et al. [2012], [c]AIA predicted response in DN s^{-1}to the EIS observed intensity. [d] Line not observed in quiet sun EIS data, estimates based on CHIANTI data. Total predicted AIA signal: 2800 DN.

signal. Because of the temperature gradients in the lower corona, the Fe IX/Fe X emission ratio decreases with radial distance from the limb. The contributions are even near 1.1 $R_\odot$. Figure D.1 shows the ionization equilibrium populations for iron as predicted by Arnaud and Raymond (1992). Fe IX has a wider FWHM as well a higher maximum population than the other Fe VIII-XIV ions. This stems from the full shell ground configuration, $1s^2 2s^2 2p^6 3s^2 3p^6$.

Although, the 171Å bandpass includes multiple blends these blends are predominantly centered on the same temperature range. There are lines within the 171Å which can contribute to the AIA signal at other temperatures: O VI 173.0Å, Ni XV 176.7Å, and O V 172.2Å. Ni XV has a peak ion population at 2.5 MK, and its contribution increases as a function of height off limb. Although it is a relatively strong line, it sits at the long-wavelength extreme of the bandpass. O VI has a peak ion population at 3×10^5 K. The O VI 173.0Å line does not emit strongly because the excitation level sits at a high energy relative to temperature of peak ionization. This significantly reduces its collision strength. O V 172.2Å is similar to O VI is that there is a large energy difference between the ionization peak and the excitation level. This line is not observed by EIS, but we have included it in the contributing line list for several reasons. It has a strong transition rate (3×10^{10}s^{-1}). It sits at wavelength of maximum effective area for the 171Å bandpass. O V is a complicated ion with numerous resonances which might affect non-equilibrium emission.

Ion	Line	EIS Intensity[a]	AIA E.A.[b]	AIA Response[c]
Fe XII	193.509	1.99×10^5	1.782	4883
Fe XII	195.118	2.31×10^5	1.118	3592
Fe XII	192.395	1.10×10^5	1.722	2591
Fe XII	186.873	2.58×10^5	0.388	1330
Fe XI	192.812	0.46×10^5	1.774	1125
Fe XI	188.216	1.21×10^5	0.689	1112
Fe XI	188.302	0.87×10^5	0.710	825
Fe XII	195.170	0.53×10^5	1.081	802
Fe X	190.040	0.35×10^5	1.171	547
Fe XIII	196.522	0.92×10^5	0.380	490
Fe VIII	194.659	1.45×10^5	1.417	284
Ca XIV	193.879	0.94×10^5	1.725	224

Table D.2 Emission line data for the 193Å AIA bandpass. Headers same as Table D.1. Total predicted AIA signal: 25851 DN

193Å

The 193Å bandpass has the strongest signal at the solar limb of any of the AIA bandpasses. This bandpass is centered on the Fe XII $3s^2 3p^2 3d\ ^4P_{3/2} - 3s^2 3p^3\ ^4S^o_{3/2}$ transition. At the peak ion temperature, this is the second most common collisional transition (first is the $3s^2 3p^2 3d\ ^4P_{5/2} - 3s^2 3p^3\ ^4S^o_{3/2}$ 195.1line). The Fe XII ion was explained in some detail in Appendix B. The term-split ground configuration creates multiple ground-level transitions around 195Å, which are shown in Table D.2. Fe XII transitions represent 56% of the AIA signal. Fe XI blends represent another 20%. The a majority of the other contributions come from other warm coronal lines emitted in the 1-2$\times10^6$K range (Fe X: 5%; Fe XIII: 5%; FeXIV: 2%; Ar XI: 1%).

Outside of that temperature range, the two strongest contributors are Fe VIII 194.6Å and Ca XIV 193.8Å. Both of these lines sit near the maximum efficiency of the AIA telescope. Fe VIII will contribute emission from plasma near 5×10^5K. Ca XIV will contribute emission from plasma near 3 MK, but this hot emission should only be present near active regions.

Ion	Line	EIS Intensity[a]	AIA E.A.[b]	AIA Response[c]
Fe XIII	203.827	5.43×10^5	0.284	2238
Fe XIV	211.314	1.22×10^5	1.057	1935
Fe XIII	209.619	0.68×10^5	1.062	1072
Fe XIII	209.917	0.32×10^5	1.089	525
Fe XIII	203.737	1.19×10^5	0.275	475
Fe XIII	201.123	2.67×10^5	0.101	384
Fe XIII	202.046	1.75×10^5	0.146	369
Fe XIII	204.260	0.69×10^5	0.328	329
Fe X	202.447	1.57×10^5	0.754	175

Table D.3 Emission line data for the 211bandpass. Headers same as Table D.1. Total predicted AIA signal: 10962 DN

211Å

The 211Å bandpass is centered on the Fe XIV $3s^2 3d\ ^2D_{3/2} - 3s^2 3p\ ^2P^o_{1/2}$ 211.1Å transition (resonance line, if core excitations are ignored). At the solar limb, Fe XIII emission dominates over Fe XIV, but the ratio Fe XIII/Fe XVI decreases with height. Fe XIII exhibits a strong set of lines near 205Å similar to Fe XII at 195Å. The spectrum at 210Å is less crowded than 193Å. The Fe XIV line contributes 21% of the AIA signal. Fe XIII lines contribute 56%, and Fe XII lines contribute 7%. There is significant overlap in the 211Å bandpass with ions emitting in the 193Å bandpass, but there is a net shift such that the 211Å bandpass is observing hotter plasma, especially at higher altitude. At a height of 1.02 R$\odot$ the ratio Fe XIII 203.8Å/Fe XIV 211.3Å decreases 0.52 due the coronal temperature gradient. The 211Å bandpass has significantly less signal than 193Å (over a factor of 2 at the limb).

94Å, 131Å, and 335Å

There are three bandpasses in AIA that have not been used on the previous imager missions. They are centered on the Fe XVIII 93.9Å, Fe XX 132.8Å, and Fe XVI 335.4Å. These are resonance lines intended for diagnostic use on flaring regions with temperatures great than 5 MK. It is possible that a component of the steady corona exists at that temperature but it is not likely to comprise more than a few percent of the total emission measure [Reale et al., 2009]. Only the

131Å bandpass contains a emission which can aid cool coronal analysis, which features weak Fe VIII lines at 131.24Å and 130.94Å. The diagnostic viability of the 131Å data is discussed in section 3.3. The other two bandpasses are ignored in this thesis, as their signal-to-noise is too low to be of diagnostic value.